Mechanical and Failure Properties of Human Cerebral Blood Vessels

by

Kenneth LaVaun Monson

B.S. (Brigham Young University) 1995

M.S. (Brigham Young University) 1997

A dissertation submitted in partial satisfaction of the
requirements for the degree of

Doctor of Philosophy
in

Engineering-Mechanical Engineering

in the

GRADUATE DIVISION

of

THE UNIVERSITY OF CALIFORNIA, BERKELEY

Committee in charge:

Professor Werner Goldsmith, Chair
Professor Marian C. Diamond
Professor Tony M. Keaveny
Professor Jeffrey C. Lotz

Fall 2001

The dissertation of Kenneth LaVaun Monson approved:

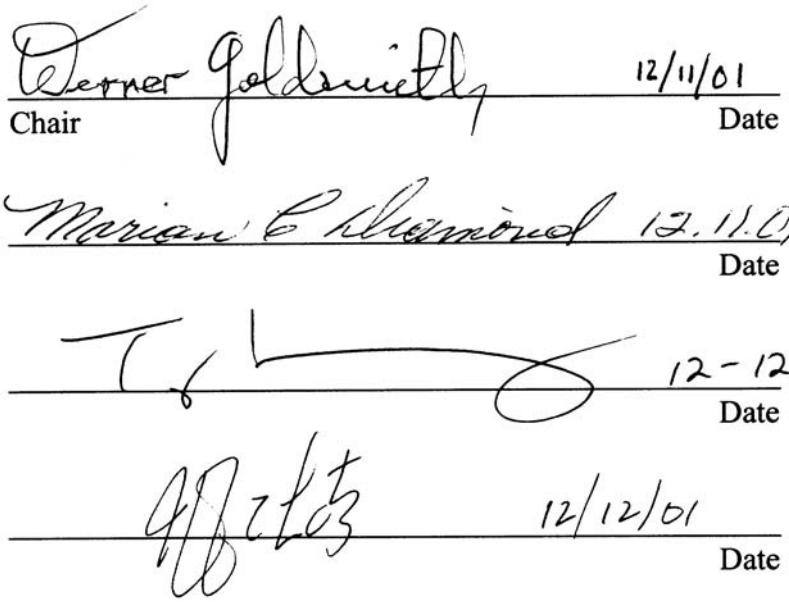

Chair — Date

Date

Date

Date

University of California, Berkeley

Fall 2001

Abstract

Mechanical and Failure Properties of Human Cerebral Blood Vessels

by

Kenneth LaVaun Monson

Doctor of Philosophy in Mechanical Engineering

University of California at Berkeley

Professor Werner Goldsmith, Chair

Human cerebral blood vessels are frequently damaged in head impact, such as occurs in falls, contact sports, or vehicular collisions, resulting in intracranial bleeding. As an integral part of the support structure for the brain, these vessels also play a key role in the load response of the cranial contents. An understanding of the mechanical behavior of these arteries and veins, as well as their limiting loads, is thus required for a proper understanding and modeling of traumatic brain injury--as well as providing substantial assistance in preventive measures and even diagnosis and treatment. It is believed that axial stretching is the dominant loading mode for the blood vessels, regardless of the nature of the insult.

A total of 43 arteries and 24 veins from the cortical surface of the temporal lobe of the cerebrum were harvested from healthy patients in surgery and from cadavers in autopsy and successfully tested for mechanical properties. Most of the vessels were stretched to failure in the longitudinal direction, some quasi-statically and some dynamically, while a few arteries were inflated to failure. The significance of specimen and experiment parameters was determined through multivariate analysis of variance (MANOVA) testing. Longitudinal test results demonstrate that the arteries were considerably stiffer than the veins, carrying approximately twice as much stress as the

veins at failure but withstanding only half as much stretch. Autopsy specimens were found to carry substantially less stress at failure than surgical samples, and no significant rate dependence was measured over a strain rate range of three orders of magnitude. Differences between tests resulting in failure at the grip and those rupturing in midsection were not found to be significant, and the extent of preconditioning was shown to be influential in measurements on arteries. Inflation tests on arteries demonstrated, as expected, that at a chosen circumferential stretch, circumferential stresses increase with more extensive axial stretches. Cortical arteries appear to be stiffer and stronger in the longitudinal direction than they are circumferentially. With regard to modeling, uniaxial vessel behavior over a limited span can be accurately represented by an exponential function, but a popular, two-dimensional constitutive model is shown to have major shortcomings in simulating combined inflation and stretch of the cortical arteries.

_____

Werner Goldsmith

Dissertation Committee Chair

Table of Contents

List of Tables

List of Figures

Nomenclature

Roman Symbols

Symbol	Units	Definition
A	-	Constant
$\widetilde{A}$	m^2	Cross-sectional area in the reference configuration
B	Pa	Constant
b_i	-	Constant
$\mathbf{C}$	-	Right Cauchy-Green, or Lagrangian, stretch tensor
C_{zz}, $C_{\theta\theta}$	-	Axial, circumferential components of $\mathbf{C}$
c	J/kg	Constant
$\mathbf{E_A}$, $\mathbf{e_i}$	-	Unit vectors (reference, current configurations)
$\mathbf{F}$	-	Deformation gradient tensor
F	N	Measured axial load
f	cycles/sec	Frequency
H, h	m	Wall thickness (reference, current configurations)
J	-	det $\mathbf{F}$
k	N/m	Stiffness
m	kg	Mass
Mod_Y	Pa	Maximum slope or elastic modulus at yield
n_i	-	Constants equal to either 0 or 1
$\mathbf{P}$	Pa	First Piola-Kirchhoff Stress tensor
P_{zz}, $P_{\theta\theta}$	Pa	Axial, circumferential components of $\mathbf{P}$
p	Pa	Internal pressure
R, r	m	Vessel radius (reference, current configurations)
$\mathbf{T}$	Pa	Cauchy Stress tensor
$T_{\theta\theta}$	Pa	Circumferential component of $\mathbf{T}$
W	J/kg	Strain energy per unit mass
$x, \dot{x}, \ddot{x}$	m	Displacement, velocity, acceleration
Z, z	m	Vessel length (reference, current configurations)

Greek Symbols

Symbol	Units	Definition
λ_{iv}	-	*In vivo* stretch
λ_T	-	Length of toe region (measure of stretch)
λ_r, λ_θ, λ_z	-	Stretch (radial, circumferential, axial components)
λ_Y	-	Yield stretch
λ_U	-	Ultimate stretch
σ_Y	Pa	Yield stress
σ_U	Pa	Ultimate stress
ω	rad/sec	Circular frequency

Acknowledgements

Having consulted with and relied on a large number of faculty, students, and others in the accomplishment of this work, I wish to thank all of them. I would like to express particular gratitude to the following individuals for their key roles:

Professor Werner Goldsmith for his supervision of this project and his insurance of its financial support, for his expertise in and commitment to head injury research into his retirement years, and for his friendship and concern for me and my family.

Doctor Geoff Manley for his commitment to the problem of head injury, for practical insights that guided the direction of this project and made it possible, and for his friendship.

Professors Marian Diamond, Tony Keaveny, and Jeff Lotz for project insights and review of the manuscript.

Doctor Nick Barbaro and many neurosurgical residents for harvesting specimens.

Doctor Peter Bacchetti and Alan Bostrom for statistical expertise and analysis.

Sherene Ban, Ruhi Kumar, Sung Ho Kim, and Eugene DelValle for their assistance with a variety of research tasks, including tissue acquisition, testing, and data analysis.

Doctor Chuck Monson, my brother, for consultation regarding experimental setup and data analysis.

My parents for their love, support, and confidence in me.

My wife, Jill, for her love, companionship, and support and for her willingness to sacrifice many of the comforts of life.

My children – Lauren, Caleb, and James – who are continual reminders of what matters most in life.

1 Introduction

1.1 TRAUMATIC BRAIN INJURY (TBI)

Head injury is a critical health problem worldwide, with approximately 1.5 million people suffering a traumatic brain injury each year in the United States alone. Fifty thousand of these die, while 230,000 are hospitalized and survive (Thurman, 1999). Motor vehicle accidents and falls are the leading causes of head injury among those of age ranges 5-64 and 65 and older, respectively, but firearms are also a significant factor, particularly when injuries resulting in death are considered (CDC).

Head injuries are commonly classified as penetrating or non-penetrating. Penetrating injuries arise almost invariably from impact of projectiles or pointed objects, with damage occurring through direct deformation of cranial tissue by the foreign object and by massive pressure increases due to the added volume of the object. The resulting injuries are almost always extremely severe, and besides avoiding contact with the penetrating object or wearing a helmet, there is little one can do to minimize initial damage. Non-penetrating head injuries result from either direct impact to the head or impulsive loading, where motion is imposed on the cranium by forces acting through the neck. In these cases, the mechanisms producing damage are sometimes unclear. In contrast to penetrating injuries, severity ranges from trivial to fatal, and there is great potential for preventing or reducing the degree of these injuries through the use of protective equipment. In addition to penetrating and non-penetrating descriptions, injuries may also be classified as primary, referring to damage that occurs at the moment of insult, or secondary, denoting conditions that develop subsequent to the injury.

1.2 BIOMECHANICS AND TBI

In the effort to understand and mitigate the scope of traumatic brain injury, biomechanics, or the application of mechanics to biological systems, has emerged as an invaluable tool for delineating events associated with primary trauma. Increased knowledge of an injury event and its consequences further clarifies the mechanism of injury, providing for better prevention, diagnosis, and treatment. In engineering mechanics, models are utilized to investigate the relationship between the input to and response of a given system. Analytical, numerical and physical (including biological – animal, cadaver, and living human, at non-injurious loading levels) models of varying scope are all employed in the study of head injury. Computational models are frequently used since they allow relatively simple exploration of a complex system's response through input and parameter variation. Physical models, however, are the only way to appreciate a tissue's local and global response to loading, to quantify its properties, and to validate a numerical representation. The interaction between model types contributes to an ultimate objective – the development of a model, or collection of models, that can predict the response of the head and its various components, including the occurrence and extent of injury, to a myriad of loading scenarios, at least within the bounds allowed by natural variation of biological tissue properties. In pursuit of this goal, investigators have explored the mechanical behavior of various cranial structures and their interactions with surrounding tissues. Results have been incorporated into numerical models that have subsequently become increasingly more complex and accurate but still lack the level of detail required.

While many of the significant tissues of the head have been included in the most advanced models, the cranial vasculature has yet to be incorporated. With few

exceptions, the mechanical properties of these arteries and veins, including failure values, have not been measured. Study of the behavior of brain vessels under loading is critical not only because they are commonly damaged during impact and impulsive loading but also because they are a vital piece of the composite structure of the brain and thus play an important role in its overall response to mechanical loading.

1.3 OBJECTIVES AND SCOPE

The main goal of the current investigation is the characterization of the mechanical and failure properties of cerebral blood vessels from living humans. This is considered to be a step toward more accurate traumatic brain injury models that can better predict the response of the head to mechanical loading and provide critical levels for the onset of various types of trauma. The goal will be accomplished by meeting the following objectives:

1) Axial stress-stretch behavior, up to the point of structural failure, of human cerebral arteries and veins will be measured through *in vitro* tensile tests. Specimens will be obtained both through surgery and autopsy. The significance of state of preservation and rate of loading on the vessels' behavior will be determined. The influence of repeated sub-failure stretching will also be clarified.
2) The interaction between axial and circumferential stretch will be investigated through inflation tests. Vessel behavior will be measured at various combinations of axial load and internal pressure. Similar to uniaxial longitudinal tests, the vessels will be pressurized to the point of failure to delineate maximum allowable circumferential stresses.

3) Collected data will be utilized to analyze how well existing constitutive models for blood vessels describe the behavior of cerebral arteries and veins. Because current computational models of the head are only capable of treating these vessels as string-like structures, i.e. able to sustain axial tension only, modeling efforts will focus on uniaxial forms of constitutive relations. With data available from both inflation and axial stretch tests, however, biaxial relations will also be considered.

This study is considered to be a major step toward the full mechanical characterization of healthy cerebral vessels. While a two-dimensional model of the vessels will be proposed, the lack of available data will surely limit its applicability. Data from future experiments can be combined with the data reported here to produce a more representative relation. Further, while this investigation is limited to dilatational loading, the behavior of these vessels in shear, particularly as induced by torsion, is surely also important. Finally, efforts in this study are limited to the primary response of these vessels while they are in a passive state, i.e. the influence of smooth muscle activation along with other chemical and physiological factors associated with reaction to loading are not considered.

1.4 CONTRIBUTIONS

The delineation of cerebral blood vessel behavior will improve head injury modeling capabilities, which will forward the design of protective structures and equipment, give additional insight into mandated protective standards through improved knowledge of human tolerances, and provide a stronger physical basis for diagnosis and resulting treatment. Although secondary to the intent of this dissertation, the information may also

be beneficial in the study of cerebral vessel pathology, such as aneurysms, arteriovenous malformations, arteriosclerosis, and hypertension.

2 Background

This chapter provides a review of the basic anatomy relevant to TBI, with a focus on the cerebral vasculature and its structure, as well as a brief description of typical lesions. An examination of related investigations is also presented. More complete descriptions of head and brain anatomy may be found in general anatomy texts and in books by Diamond *et al* (1985) and Netter (1997). Much of the material presented in this chapter is also discussed to one degree or another in excellent survey papers on head injury biomechanics, such those by Goldsmith (1970, 2002) and Melvin *et al* (1993).

2.1 ANATOMY OF THE HEAD

The head is divided into the face and the cranium and its contents, with the skull composed of eight separate bones. These bones fuse together to form a composite shell of spongy (trabecular) bone, known as diploë, sandwiched by compact (cortical) bone. For the most part, both the inner and outer surfaces of the brain case are topographically smooth. As illustrated in Fig. 2.1, however, the floor of the inner surface is made up of three abrupt steps, the anterior, middle, and posterior fossae, that roughly coincide with the inferior aspect of the brain. Various openings, the largest of which is the foramen magnum where the spinal cord connects to the brain, traverse the base of the skull, allowing the entrance and exit of blood vessels and nerve fibers.

Between the inner surface of the cranium and the brain (and extending to encase the spinal cord) are three layers of membranes known as the meninges. The outermost layer, the dura mater, is a relatively tough membrane made up of two layers. The outer layer is rigidly attached to the skull, while the inner layer generally follows the contour of the brain, forming four septa that compartmentalize it. Depicted in Figs. 2.1 and 2.2, the two

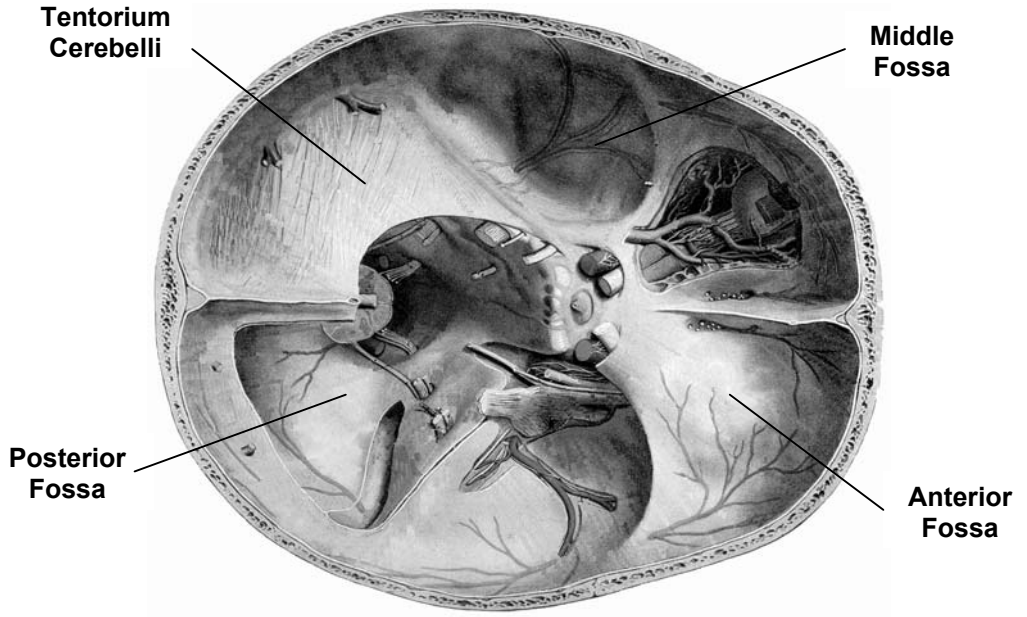

Figure 2.1 Base of human skull with right portion of tentorium cerebelli removed (modified from Fig. 671 in Sobotta, 1928)

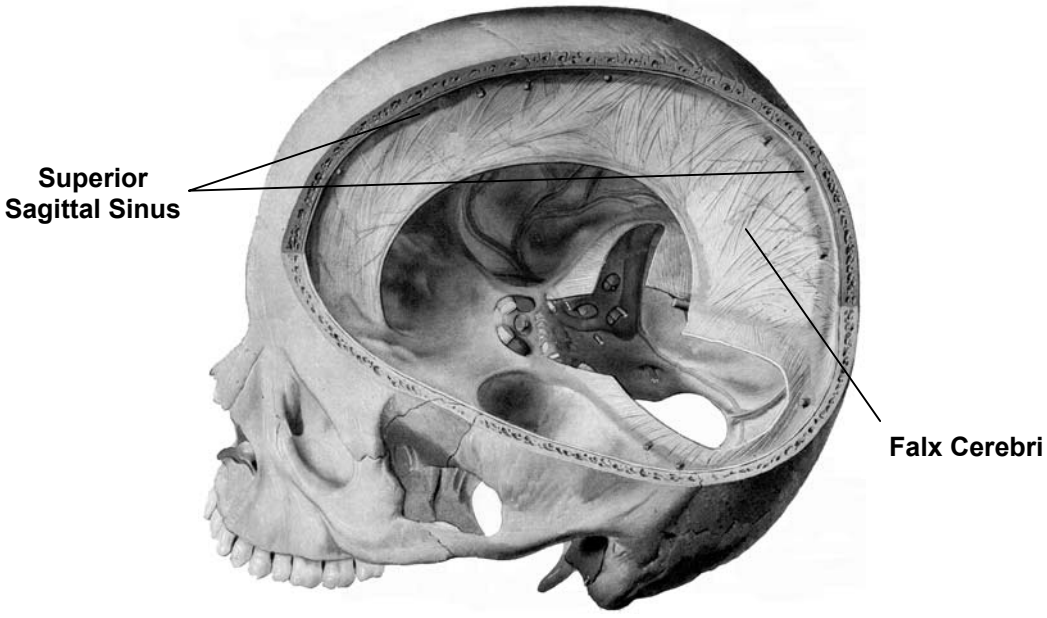

Figure 2.2 Human skull with portion of skull cut away and brain removed to show intact falx cerebri (modified from Fig. 672 in Sobotta, 1928)

largest of these, the falx cerebri and the tentorium cerebelli, extend between the cerebral hemispheres and the cerebrum and cerebellum, respectively. At the base of the septa, the two dural layers separate to form sinuses that serve as channels for venous blood.

The delicate inner meningeal layers lie just inside the dura, although they share no connection with it except through cerebral veins that traverse the meninges to the sinuses. The middle layer, named the arachnoid, lies in direct contact with the dura and is connected to the innermost layer, the pia mater, by web-like strands. The pia closely follows the complex contours of the brain surface. The space between these two membranes, known as the subarachnoid space, is filled with cerebrospinal fluid (CSF) and provides space for cortical arteries and veins. Figure 2.3 portrays a coronal cross-section of the superior skull, the meninges, and the brain in the region of the falx cerebri.

The brain itself, described by Ommaya (1968) as a "soft, yielding structure, not as stiff as a gel nor as plastic as a paste," is made up of two cerebral hemispheres, the

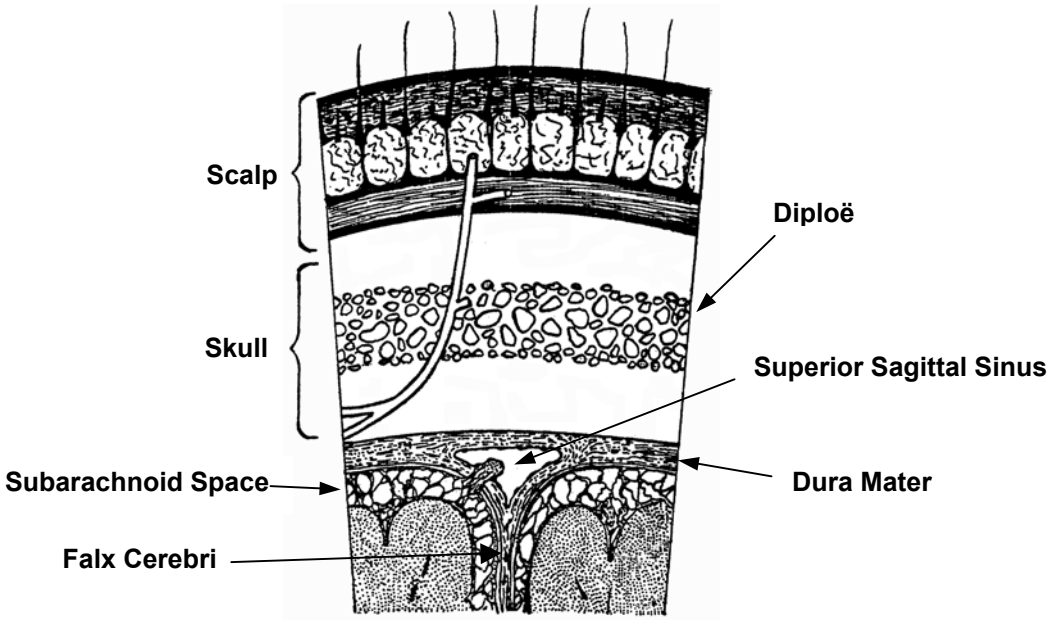

Figure 2.3 Sketch of superior frontal section showing scalp, skull, and meninges

cerebellum, and the brainstem. The cerebral hemispheres are divided into lobes made up of gray and white matter and encompass the lateral ventricles where the CSF is formed. The gray matter is a collection of nerve cell bodies found in the outer layers, or cortex, of the brain and in the basal ganglia deep within the brain. The white matter consists of neural tracts, or cell processes, allowing communication within the hemispheres and with other parts of the central nervous system. The brainstem refers to the diencephalon, including the thalami and related structures, the midbrain, containing the colliculi among other structures, the pons, and the medulla oblongata. The third and fourth ventricles, along with the cerebral aqueduct, are formed by the midbrain.

2.1.1 Cerebral Blood Vessels

2.1.1.1 Cerebrovascular Structure

2.1.1.1.1 Blood Supply to the Brain – The Cerebral Arteries

Although the human brain accounts for just three percent of body weight, its activity requires one-fourth of the total cardiac output (Diamond, 2001). Arterial blood is supplied to the brain through four main arteries, the left and right internal carotid arteries and the left and right vertebral arteries. Branches of these four arteries eventually join together at the base of the brain to form the Circle of Willis around the pituitary gland.

The internal carotid arteries, which deliver eighty percent of the brain's arterial blood, branch off from the common carotid arteries in the neck, traverse the base of the skull through the carotid canals of the temporal bone, and pass though the cavernous sinus before arriving at the base of the brain. Each vessel then branches into the opthalmic artery, supplying the eye on its respective side, and the anterior and middle cerebral arteries. These cerebral arteries together provide for the needs of the frontal, parietal, and

insula lobes, along with portions of the temporal and occipital lobes. The two anterior cerebral arteries are connected by the anterior communicating artery, forming the anterior portion of the Circle of Willis.

Carrying the other twenty percent of needed blood, the vertebral arteries originate from the subclavian arteries at the base of the neck, ascend through the transverse foramina of the cervical vertebrae, and enter the cranium through the foramen magnum, where the two vessels combine to form the basilar artery on the inferior surface of the brainstem. Before combining, the arteries give off branches that supply the medulla, the spinal cord, and part of the cerebellum. The basilar artery continues to ascend, providing blood to the cerebellum and the pons, until it branches into the posterior cerebral arteries and the posterior communicating arteries at the base of the brain. The posterior cerebral arteries feed the occipital lobe and the inferior and medial portions of the temporal lobes. The posterior communicating arteries extend anteriorly to connect with the middle cerebral arteries, connecting the arterial circuit started with the vertebral arteries to that associated with the internal carotids.

As the cerebral arteries extend into the hemispheres, they give off small branches to feed the inner structures of the brain, including the thalami and the basal ganglia. When they reach the cortex, however, they are still of significant size and spread over the cortical surface, with small branches diving into the gray matter, which is at least twice as vascular as the white matter (Stehbens, 1972). The resulting structure contrasts with that of other organs where vessels branch off like the structure of a tree and only the smallest vessels are found at the most distal locations. Figure 2.4 displays the cerebral artery structure on the convex surface of the right hemisphere, while Fig. 2.5, a photo of a

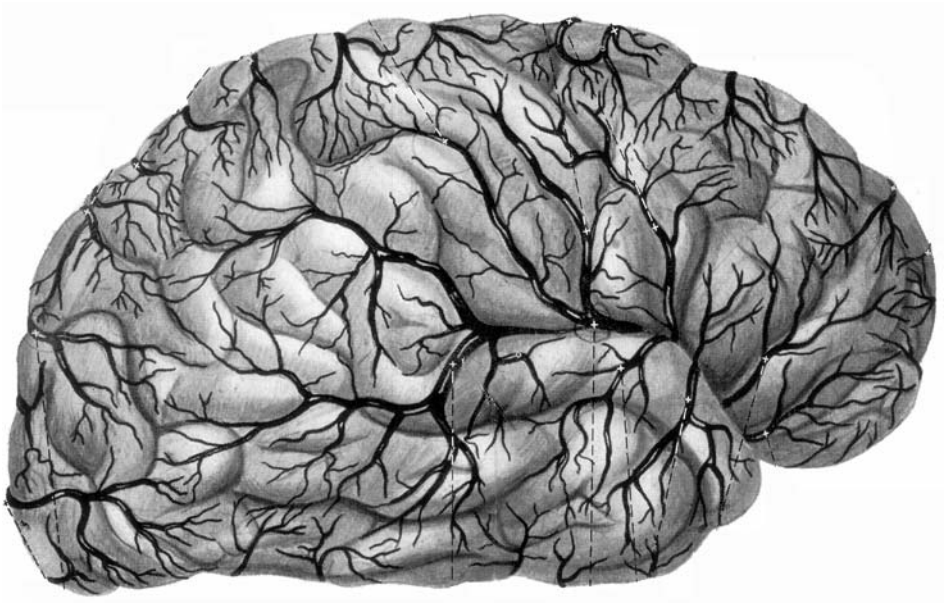

Figure 2.4 Convex surface of right hemisphere showing cortical arteries (modified from Fig. 321a in Woerdeman, 1950)

Figure 2.5 Photograph of a cerebral artery cast (Fig. E, p. 61 in McMinn, 1977; used with permission – Mosby 0723408823)

cerebral artery cast with the surrounding brain removed, illustrates the dense, complex nature of the arterial arrangement both on and below the convex surface of the hemisphere.

2.1.1.1.2 Venous Drainage of the Cerebral Hemispheres

The brain capillaries drain into the cerebral veins, which are classified as either superficial or deep. The superficial veins include the inferior, superior, and middle cerebral veins, which drain the inferior, superior, and lateral surfaces of the brain, respectively. Much like the cortical arteries, these collecting veins form a network over the surface of the cortex. The deep veins, including the internal cerebral vein and the basal vein, drain the thalami and basal ganglia and unite on the posterior aspect of the brain stem to form the Great Vein of Galen. Each of these veins empties into one of the many sinuses of the cranium, forming a connection between the brain and dura, and are often thus referred to as “bridging” veins. Figure 2.6 depicts the superior surface of the brain with the dura partially retracted. The upper wall of the superior sagittal sinus has been removed to show the entrance points of the superior cerebral veins. The inferior, superior, and middle cerebral veins drain into the transverse, superior sagittal, and cavernous sinuses, respectively, although the middle cerebral also connects to the other two veins through the anastomotic veins of Trolard and Labbé. Each of the sinuses, connected to each other in various ways, eventually drains into the jugular veins, which serve as the main route for cranial cavity drainage. The cavernous sinus, however, also connects to extracerebral vessels, providing another pathway for drainage besides the jugulars. Similarly, emissary veins through skull also form a mode of collateral venous flow.

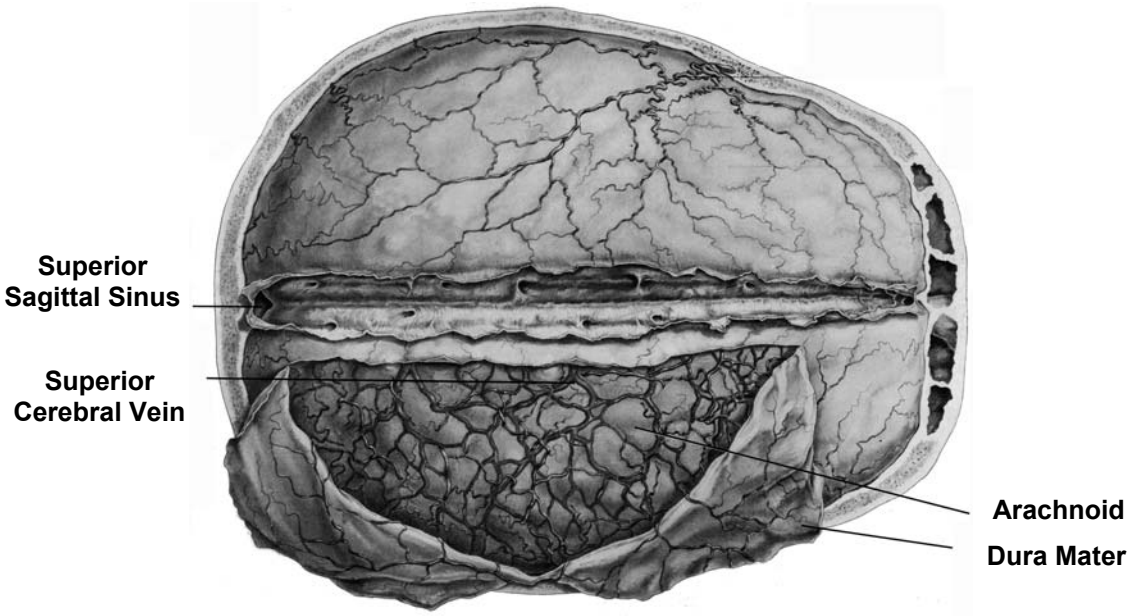

Figure 2.6 Superior surface of brain with skull removed and dura partially retracted (modified from plate CXLVIII, p. 573 of Deaver, 1903-1904)

2.1.1.2 Cerebral Vessel Architecture

Blood vessels are made up of a number of adherent concentric layers, the significant structural components being elastin and collagen fibers and smooth muscle cells. In general, both arteries and veins consist of three main layers, the intima, the media, and the adventitia, from innermost to outermost, with the three layers separated by sheets of elastin called the internal and external elastic laminae. The intima is made up of endothelial cells on a thin layer of elastin. Smooth muscle cells, oriented in a mostly-circumferential helix and embedded in a complex of elastin and collagen, dominate the media. Additional thin elastic laminae separate concentric layers of smooth muscle within the media. Adventitia is mostly made up of collagen and is typically less organized than the other layers. The specific constitution of arteries, in particular, varies considerably with distance traveled in the circulation. As blood moves toward the periphery, the

number of elastic laminae within the media decreases until distinct layers can hardly be identified (Holzapfel *et al*, 2000). As a result, large arteries proximal to the heart are classified as "elastic" (not to be confused with a material's characterization as elastic in mechanics) while those in the periphery are referred to as muscular. Cerebral arteries fall within the muscular group. While arteries and veins share the same general structure, veins typically have relatively thin walls in comparison to their diameters.

When compared to extracranial arteries, the cerebral arteries are distinct in many ways, as described by Stehbens (1972), Hayashi *et al* (1980), Holzapfel *et al* (2000), and Finlay *et al* (1995). These arteries contain a thicker internal elastic lamina than other vessels. The media consists of up to twenty layers of smooth muscle arranged in mostly a helical direction, although there are some longitudinally oriented fibers in the outer media. Media thickness is less than in comparable extracranial arteries and contains much less elastic material, or elastin. The external elastic lamina is nonexistent, and like the media, the adventitia, composed mostly of collagen, is also thinner than in extracerebral arteries, to the point of being difficult to identify at all. It contains less elastin than adventitia in extracerebral vessels. Some investigators have suggested that these compositional differences might be due to the fact that cerebral vessels are, in general, not subject to exterior pressures or tensile loads (Stehbens, 1972). Finlay *et al* point out that the fibers in the cerebral artery wall become better organized, or oriented in common directions, as internal pressure increases.

Compared to arteries, a significantly smaller amount of attention is devoted to cerebral vein architecture in the literature. Stehbens (1972) describes these vessels as extremely thin, composed primarily of collagen, with very little elastic tissue or smooth

muscle. Some describe the vessels as having no media at all. In contrast to the arteries, when internal pressure is removed from the veins, they become limp, no longer retaining their circular cylindrical shape. While cerebral arteries typically see around 100 mmHg of internal pressure, the blood pressure of cerebral veins may be as low as 0 mmHg, with negative pressures in the sinuses (Stehbens, 1972).

2.2 LESIONS IN TRAUMATIC BRAIN INJURY

2.2.1 Structure and Implications for Injury

The preceding review of head anatomy illustrates the intrinsic protection provided to the brain. The scalp and the sandwich shell of the cranium provide excellent energy absorption properties, providing a sort of natural helmet, while the meninges, with their accompanying septa, and the CSF serve to limit the motion of the brain within the skull in a more gentle fashion than the rigid skull could alone. Further, the CSF acts as a cushion that protects the brain from blows and buoys it up to limit contact with its surroundings. The ventricles, filled with CSF, have been shown to reduce stresses within the brain (Ivarsson *et al*, 2000). The preceding discussion has also clearly identified the presence of a complex vascular structure around and within the brain. It is clear that any deformation of the brain must also include consideration of these arteries and veins.

Despite the system's natural defenses against primary injury, even well-protected areas aren't safe for all insults. Further, some features of the anatomy make the brain vulnerable in different ways. Contusions, for example, perhaps best described as bruises on the brain's surface, are the most common lesion in head injury. They typically occur at sites where the brain impacts irregular surfaces of the inner skull (such as the abrupt step

between the middle and anterior fossae) as a result of relative motion (Gean, 1994). The most common locations are the anterior temporal lobes of the brain, the anteroinferior frontal lobes, and the inferior temporal lobes. An example of a typical contusion as viewed by MRI is shown in Fig. 2.7 (arrows locate the contused temporal tips). Such contusions involve the superficial brain tissue including the gray matter, with lesser trauma of the deeper white matter.

Another common injury in which the head structure produces vulnerability is subdural hematoma resulting from the tearing of veins that bridge the distance between the brain and the sinuses. Because the superior bridging veins are the only solid connection between the brain and skull in this region, relative motion between the skull and brain stretches these vessels. If the magnitude of an insult is significant, the bridging veins may be stretched until they rupture, resulting in bleeding in the subdural space.

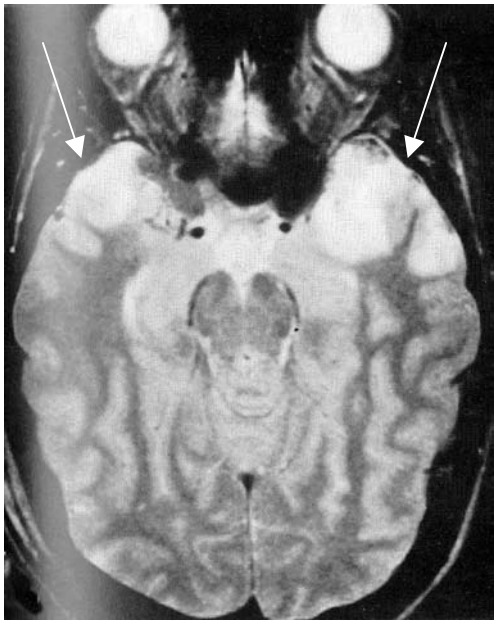

Figure 2.7 Temporal lobe contusions. A T-2 axial MRI image shows typical bilateral temporal lobe contusions in a patient following traumatic head injury (arrows point to injured regions).

These veins, for the most part, drain frontally into the superior sagittal sinus and are thus more vulnerable to occipital impacts than to frontal ones (Lee and Haut, 1989).

2.2.2 Characterization of Lesions

As indicated in Chapter One, head injuries are often described as either penetrating or non-penetrating. Non-penetrating trauma is commonly further categorized as either diffuse or focal. Diffuse injuries are, by definition, widespread and often symmetric and range in magnitude of severity from damage resulting in mild concussion to diffuse axonal injury, i.e. from a temporary interruption of some physiological processes to a permanent mechanical disruption of axons. Other injuries categorized as diffuse include hypoxic brain damage, brain swelling, and diffuse vascular injury.

In contrast to diffuse injuries, focal injuries are more localized and are generally not symmetric. These injuries are commonly associated with blood vessel failure, such as hemorrhage and contusion. Bleeding within the skull often results in a pool of clotting blood called a hematoma and, depending on the location of the mass, may be classified as extradural, subdural, subarachnoid, or intracerebral. If not immediately treated, any expanding lesion in the cranium may result in severe secondary damage due to increasing intracranial pressure and midline shift and distortion of the brain. Additionally, injury-induced chemical imbalances may result in hypoxia, caused by a reduction of oxygen transport to brain cells, as well as edema, or brain swelling due to poorly controlled water transport.

While it is unlikely for a serious insult to cause either diffuse or focal injury only, rather than a combination of the two, research indicates that different loading scenarios are more likely to cause diffuse rather than focal injury, and vice-versa. Using a clinical

database of 434 patients admitted to the hospital for blunt (non-penetrating) head injury, Gennarelli and Thibault (1982) studied the influence of the cause of injury on the resulting lesion. About half of the patients had been injured in motor vehicle accidents, while the other half were hurt in falls or assaults. Of 38 patients that suffered acute subdural hematoma, a focal injury, 74% were injured by fall or assault, while 24% were injured in a motor vehicle accident. In contrast, of 72 patients that suffered diffuse brain injury (characterized by unconsciousness for over 24 hours), 89% were injured in automobile collisions, whereas only 10% were impaired through fall or assault. From these data, it is clear that one type of injury does not necessarily have a lower tolerance than another; this determination depends upon the loading scenario. Similarly, it is interesting to note that skull fracture seems to have little significance in relation to severity of brain damage (Melvin *et al*, 1993) .

2.3 HEAD INJURY BIOMECHANICS

2.3.1 Brief Historical Development

Traumatic head injury has occupied the biomechanical and medical profession for many decades. Among the first bioengineering investigators of traumatic brain injury were researchers at Wayne State University sixty years ago. Through numerous experiments on animals and cadavers, their efforts included clarification of the role of impact-induced linear acceleration, with its accompanying pressure waves, in damage at the level of the brain stem (Gurdjian, 1975). Perhaps the most significant result of their early work was the Wayne State Tolerance Curve (WSTC). By dropping six embalmed cadavers on their foreheads, and assuming that linear skull fracture coincides with the onset of concussion, the researchers showed that allowable linear acceleration is a

decreasing hyperbolic function of impact duration (Lissner *et al*, 1960; Gurdjian *et al*, 1962). Because the data set was small and only included contact durations between 2 and 6 ms, later researchers supplemented the initial points with data from animals and cadavers and extended the curve to much longer contact durations through tests on human volunteers. Through experiments on cadaver skulls and monkeys, scaling to humans using dimensionless parameters, Ono *et al* (1980) showed that while the threshold for human skull fracture is slightly higher than that for concussion, the Wayne State curve was quite similar to their concussion threshold curve. The WSTC has become the foundation for head injury tolerance indexes, finding expression as the Gadd Severity Index (GSI) (Gadd, 1966) and as the government-mandated Head Injury Criterion (HIC) (Versace, 1971). Although frequently challenged, the HIC is still embedded as the main measure of injury severity in current governmental and industry-wide regulations concerning performance of protective devices, dummies, and vehicular components. Acceptable levels of acceleration and their durations are also specified for helmets and other equipment.

Approximately contemporaneous to the early work at Wayne State University, Holbourn (1943, 1945) introduced his theory regarding the mechanism of head injury. Using theoretical arguments backed up by experiments on photoelastic gel, he hypothesized that damage to the cranial tissues only occurs through shear strains. This conclusion was based on the brain's extremely high bulk modulus to shear modulus ratio. Holbourn proposed that rotation is the main mechanism for producing shear, assuming that any shear strains produced by linear acceleration of the skull were generally negligible. Through a series of experimental investigations, Ommaya and co-workers

investigated and, in general, corroborated Holbourn's proposals. In contrast to Holbourn's hypothesis, which did not differentiate between cases with impact and without, they found that concussion was much easier to produce in cases involving impact as opposed to impulsive motion only (Ommaya, Fass and Yarnell, 1968; Ommaya and Corrao, 1969). As a result, Ommaya and Hirsch (1971) suggested that half of the potential for brain injury is associated with rotational acceleration, while the other half is determined by contact phenomena. Ommaya and co-workers (1967) also proposed a relationship for scaling data from animals to humans and set forth a 50% probability tolerance level for rotational acceleration. In agreement with the Holbourn theory, experiments by Gennarelli, Ommaya, and Thibault (1971) on monkeys demonstrated clear differences between injuries produced through rotational and linear acceleration. While focal lesions were produced through translation, the investigators found it impossible to cause diffuse injury with such an impulse. Insults involving rotation, however, easily generated diffuse injury. Gennarelli, Thibault, and co-workers have continued the investigation of rotation, particularly as it influences subdural hematoma and diffuse axonal injury. In recent years, these studies have included experiments on gel models, much like Holbourn, instead of tests on animals.

2.3.2 Head Modeling

In 1966, the National Institutes of Health sponsored a meeting on head injury. Among the many important developments at the conference, Goldsmith (1966) suggested the development of a theoretical model of head injury as a means for further investigating the findings of experiments. This suggestion initiated numerous modeling efforts, at first mostly analytical and later computational. Such simulations require a knowledge of

mechanical properties of the brain and other tissues of the cranium, which were not known then. Since that time, properties, along with some failure limits, have been measured and re-measured for most of the major components of the head, including the scalp, skull, dura and brain. Mechanical properties of human tissues have been compiled in Yamada (1970) and Abe, Hayashi and Sato (1996). With the growth in computing capability has come the development of complex finite element models of the head that are growing more accurate in their ability to predict brain deformation resulting from various impacts or impulses.

In the investigation of tissue properties for these models, however, the determination of the stress-strain relations and their potential rate dependence, along with failure characteristics, of the blood vessels of the cranium have been neglected; such data are critical for the response analysis of the head to dynamic loading performed by computational methods. Head injury experiments on human cadavers demonstrated that the pressurization of cadavers' vascular systems produced stronger coupling between the skull and the brain, providing a more realistic head-brain system response (Stalnaker *et al*, 1977; Ward *et al*, 1977). As developers of finite element models have worked to improve accuracy, they have stressed the importance of the inclusion of blood vessels in the model and the lack of any data on these vessels (Bandak and Eppinger, 1994; Vossoughi and Bandak, 1996).

A recent study by modelers at Wayne State University demonstrates the significance of the presence of blood vessels in a brain model (Omori *et al*, 2000). Their two-dimensional, sagittal plane model (represented as a half circle) includes radially oriented parasagittal bridging veins, connecting the brain with the dura, as well as radially

oriented cerebral arteries, as shown in Fig. 2.8. The model also includes the skull and the CSF but omits the ventricular system. While some data have been reported for the bridging veins (Löwenhielm, 1974; Lee and Haut, 1989), no complete set of properties was available for either type of vessel, so the WSU group assumed linear elasticity and estimated a property set by piecing together a variety of studies on other vessels. Even though the anatomy of the preliminary model is far simpler than that seen *in vivo* (among other issues, see Huang *et al*, 1999, regarding significance of bridging vein orientation) and it was thus not expected to produce an accurate prediction of overall brain deformation, results from simulations reveal a dramatically different strain field in the model containing vasculature compared to a model without vessels. Figures 2.9(a) and (b) demonstrate these substantial differences in principal strain when the model is subjected to a rotational impulse consisting of a half-sine acceleration with a peak of 5000 rad/sec^2 and a duration of 5 ms followed by a deceleration half-sine with a peak of

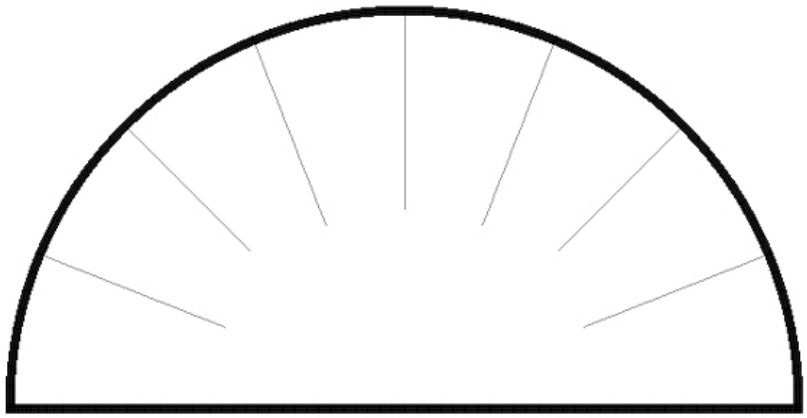

Figure 2.8 Two-dimensional, sagittal plane WSU model includes radially oriented parasagittal bridging veins, connecting the brain with the dura, as well as radially oriented cerebral arteries.

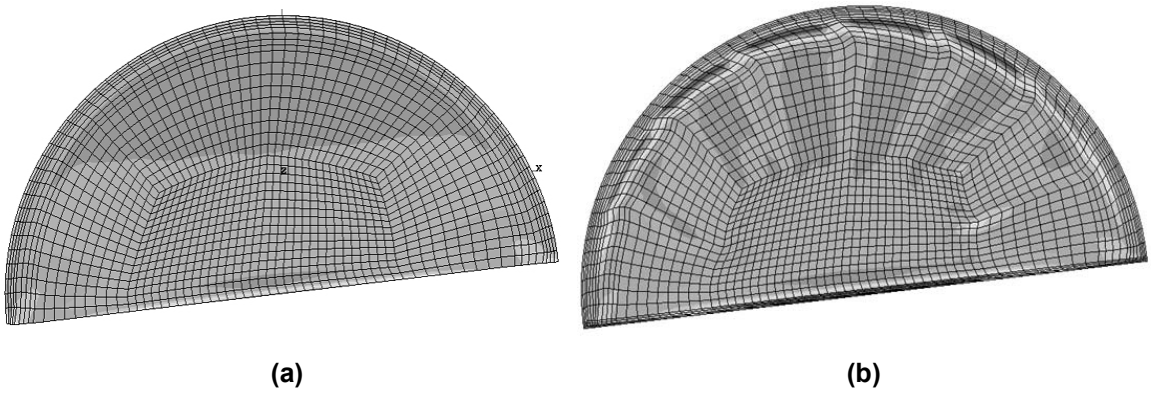

Figure 2.9 Resulting principal strains for models without (a) and with (b) blood vessels

2500 rad/sec^2 and a duration of 10 ms. The concentration of principal strains is shown to occur near the blood vessels and also at the subarachnoid space on the brain surface.

2.4 BLOOD VESSEL MECHANICS

The mechanical properties of blood vessels have been under investigation for many years, as evidenced by the work of Roy (1880). A number of excellent reviews (e.g. Dobrin, 1978) and property tabulations (Yamada, 1970; Abe *et al*, 1996) have been compiled to document research in this field. Of particular note is an extensive survey recently published by Humphrey (1995). This work includes a discussion on general artery structure and behavior, a review of the subject of nonlinear elasticity and constitutive modeling as applied to blood vessels, and a study of various experimental techniques and results.

2.4.1 General Mechanical Behavior of Passive Blood Vessels

Blood vessels have been shown to be basically incompressible under physiological conditions (Carew *et al*, 1968), and, despite the complex arrangement of fibers within the various layers, are considered to be cylindrically orthotropic (Patel *et al*, 1969). In

healthy vessels, the intima is insignificant in contributing to mechanical behavior in comparison to contributions by the media and adventitia. Typical axial load-deformation behavior of a passive blood vessel from the current study is presented in Fig. 2.10. As the plot demonstrates, the tissue is nonlinear with a large degree of distensibility at low stretches and increasing stiffness at higher stretches. Roach and Burton (1957) showed that the behavior in the low stiffness region is attributable mainly to elastin fibers, while the subsequent reduction in compliance is associated with the gradual recruitment, or straightening out, of the much stiffer collagen fibers. *In vivo*, vessels are typically loaded to levels associated with the transition between the low and high stiffness portions of the curve.

When the tissue is stretched to a small extent and then unloaded, the loading and unloading paths are clearly different, demonstrating hysteresis due to internal friction. As

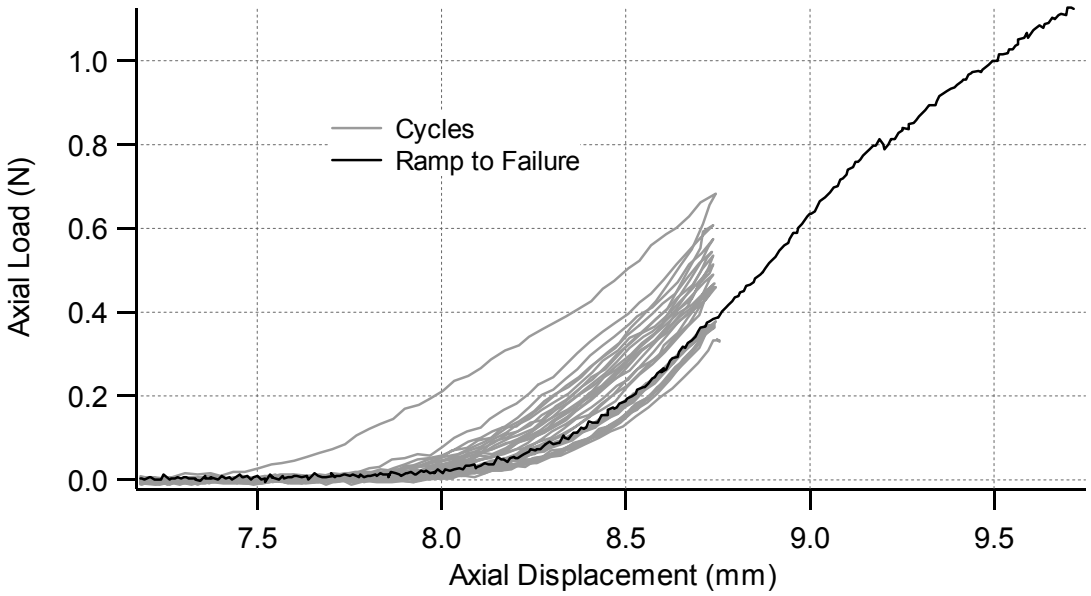

Figure 2.10 Typical axial load-displacement behavior of a blood vessel stretched repeatedly to sub-failure levels, followed by extension to failure

the beginning and end points of the two curves are coincident, this behavior is termed viscoelastic. If the cycling is continued, as in the figure, the amount of hysteresis grows asymptotically smaller until it, and the loading and unloading paths, reach a steady-state condition. With each successive cycle, the maximum load carried by the vessel decreases, demonstrating stress-relaxation phenomena, another sign of the tissue's viscoelastic nature. Fung *et al* (1979) suggested that the loading and unloading portions of the curve each be treated as a separate elastic material, allowing the constitutive equation of each one to be derived from a strain energy function. They termed this approach pseudoelasticity.

Loading a vessel beyond *in vivo* levels eventually results in inelastic behavior, where some residual stretch is present upon unloading. The level of stretch at which this elastic limit is exceeded, however, has not been quantified. Mechanical failure of the vessel begins when wall stresses rise to the level of individual fibers' strengths.

2.4.2 Constitutive Modeling of Blood Vessels

A number of constitutive forms have been suggested for modeling the mechanical behavior of blood vessels. Fung (1967) suggested an exponential formulation for uniaxial tests on biological soft tissue, noting that the derivative of the axial component of the First Piola-Kirchhoff stress with respect to stretch was approximately linear, as shown in Equation 2.1, where P_{zz} is axial load divided by the cross-sectional area of the reference

$$\frac{dP_{zz}}{d\lambda_z} = AP_{zz} + B \tag{2.1}$$

configuration, λ_z is axial stretch (current length divided by reference length), and A and B are constants. Tests on various arteries have demonstrated behavior consistent with this formulation, although with some limitations. Tanaka and Fung (1974) report the

expression to be valid for canine aorta only at stresses greater than 20 kPa. Similarly, Hayashi *et al* (1981), in tests on bovine aorta, found Equation 2.1 to accurately represent low and high stress data separately, but it was inadequate for the complete range. These approaches assumed that the tissue was homogeneous and that stresses were uniform through the cross-section.

Most multi-axial descriptions allow for possible variations within the vessel wall but may also be simplified for cases where stress is assumed uniform through the wall. Relations of this type have been given in polynomial, exponential, and logarithmic forms. The latter two expression types have been shown to provide better fits with fewer coefficients (Hayashi, 1993). The coefficients for these forms also tend to make more physical sense as material parameters than do those of the polynomial type (Fung *et al*, 1979). Recent reports by Humphrey (1995, 1999), Ogden *et al* (2000), and Holzapfel *et al* (2000) discuss the capabilities and shortcomings of some of the most commonly used models. The reports also discuss the importance of accounting for residual stresses in cases where through-wall variations are considered important. These approaches account for deformation from an open sector (assumed to be stress-free) to a deformed cylinder.

As more is learned about the physical structure of vessels, constitutive models may be proposed that include this information. Holzapfel *et al*, for example, suggest a new relation, still based largely on exponential behavior, that models the vessel as two (or more) concentric layers considered to represent the media and adventitia. Each layer is a composite of helically oriented fibers (in both directions to preserve symmetry about the axis) embedded within an isotropic material, thus producing an orthotropic material in

each layer. In general, the material axes of the two layers are not aligned with one another.

2.4.3 Previous Investigations of Human Cerebral Vessel Mechanics

Despite the extensive study of blood vessels, little has been reported with regard to human cerebral arteries and veins. While much of the behavior reported for extracranial and animal vessels may be qualitatively applied to the cerebral vessels, modeling requires that specific properties are available. None of the few studies conducted on human cerebral blood vessels has provided the range and type of data necessary for the development of a constitutive model, including behavior to failure.

2.4.3.1 Axial Stretch Testing

The first known study of the longitudinal stress-strain behavior of human cerebral vessels was carried out by Chalupnik, Daly, and Merchant (1971). Their motivation for the study of these vessels was to identify how they contribute to the dynamic response of the brain to loading, rather than to determine when the vessels themselves fail. As a result, failure properties were not reported. Twenty-eight major cerebral arteries obtained from autopsy, along with two veins, were perfused at physiological pressures, and subjected to two types of loading: sinusoidal displacements with a frequency range of 0.001 to 100 Hz and uniaxial extensions with strain rates ranging from 0.001 to 50 s^{-1}. No failure values are given, but the average largest reported stress resulting from the uniaxial extension tests is 2.0 MPa at 20% stretch. No rate dependence was observed in either type of test. As shown in Fig. 2.11, the stress-strain curve presented in their unpublished report exhibits the usual concave upward shape. Data from other vessels have also been included in the figure to allow for comparison.

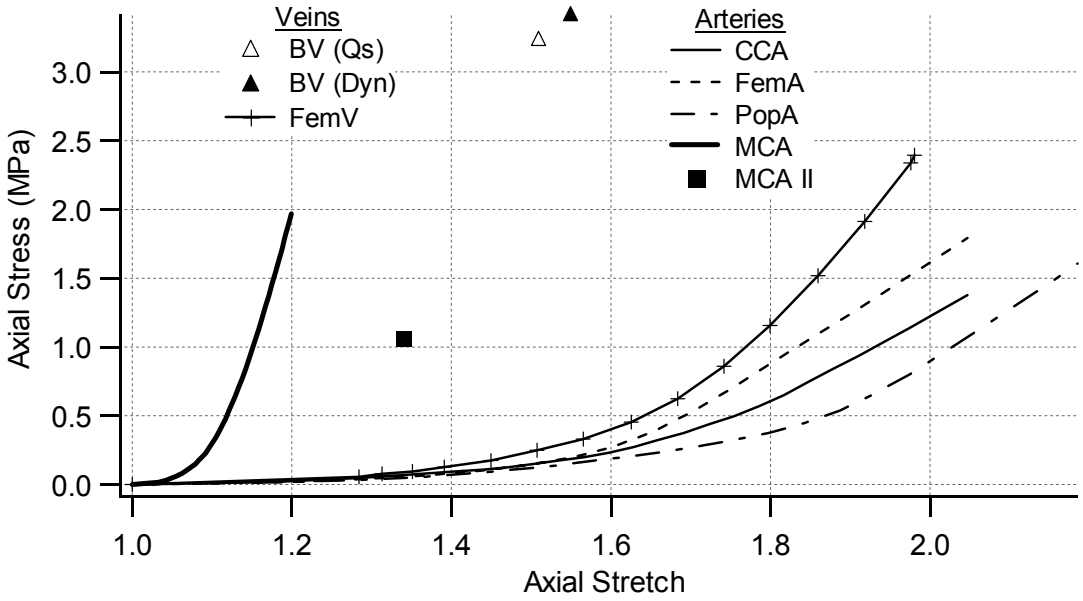

Figure 2.11 Comparison of axial stress-stretch behavior of various arteries and veins. Stress measure is First Piola-Kirchhoff. BV-bridging vein failure points (Lee and Haut) for quasi-static and dynamic tests. MCA-subfailure major cerebral artery data (Chalupnik *et al*). MCA II-failure data for major cerebral arteries (Steiger *et al*). CCA, FemV, FemA, PopA-common carotid artery, femoral vein, femoral artery, popliteal artery (Yamada).

In a study of the mechanical properties of cerebral aneurysms, Steiger *et al* (1989) tested various large Circle of Willis arteries from four patients to provide comparison data of normal vessels. Strips of arteries, obtained from both surgery and autopsy, were stretched in 0.1 mm increments (with 30 seconds between each step) until failure. As plotted in Fig. 2.11, failure stretch and stress were measured to be 1.34 and 1.06 MPa, respectively. Sub-failure data were not reported. Differences between the results reported by Steiger *et al* and Chalupnik *et al* may be due to the fact that the latter vessels were slightly pressurized while the former were not.

Another series of investigations concerned the failure characteristics of the human parasagittal bridging veins at various strain rates. Damage to these veins generally occurs due to relative motion between the skull and the brain induced by suddenly applied

angular acceleration, generally resulting in subdural hematoma. In contrast to the study by Chalupnik *et al*, the main focus of these vein studies was the failure of the veins themselves, rather than how they might influence brain dynamics in trauma. Because of this, no sub-failure data are reported. Löwenhielm (1974), the first to study these veins, reports a strong dependence of maximum elongation on strain rate, decreasing from about 70 to 20% for strain rates varying from 1 to 1000 s^{-1}, with the largest rate dependence occurring below 100 s^{-1}. Similarly, maximum stress is shown to increase significantly for this range of strain rate, although the high-rate tests show a relatively large amount of scatter. On the other hand, Lee and Haut (1989) report an absence of rate dependence for both quantities. Their tests resulted in mean maximum stresses of 3.24 and 3.42 MPa and mean ultimate stretches of 1.51 and 1.55 for quasi-static (0.1-2.5 s^{-1}) and dynamic (100-250 s^{-1}) strain rates, respectively, where differences are statistically insignificant. Stress and stretch are not correlated in Löwenhielm's report, so his data cannot be shown in Fig. 2.11, but the average failure point for Lee and Haut is included. Both Löwenhielm and Lee and Haut studied veins from cadavers.

While no other work concerning the effect of strain rate on failure of the human cerebral vasculature has been reported, there are a few studies that address the issue in human non-cerebral or in animal vessels. Löwenhielm (1978) found the failure values of bovine parasagittal bridging veins to be independent of rate, as did Lee and Haut (1985) for major neck arteries and veins from ferrets. Mohan and Melvin (1982, 1983) demonstrated similar results for ultimate strain in the human aorta, but they report a significant dependence of ultimate stress on rate, with a factor of two increase for strain rates differing by four orders of magnitude. Conversely, Collins and Hu (1972) found a

decrease in ultimate strain with increasing rate in porcine aorta. It is obvious that there exists a difference of opinion concerning rate effects on mechanical properties.

2.4.3.2 Multi-Axial Testing

A number of inflation studies has been conducted on major human cerebral arteries (e.g. Busby and Burton, 1965; Scott *et al*, 1972; Nagasawa *et al*, 1979; Hayashi *et al*, 1980; Hudetz *et al*, 1981). These efforts were concerned with the influence of such things as age, disease, and smooth muscle activation under standard physiological conditions, with the measured property being the incremental modulus or a derived stiffness parameter. These studies are extremely valuable, having revealed important characteristics of these vessels, such as the fact that intracranial arteries are stiffer than extracranial ones (Busby and Burton, 1965; Hayashi *et al*, 1980). Nevertheless, because no stress-stretch data was reported and loads were limited to physiological levels, they do not provide adequate data for modeling large stretch behavior and failure, such as occurs in trauma.

2.4.3.3 Related Studies

Other investigations that warrant brief attention here include those that have studied the behavior of the vessels within their natural environment, or in surroundings meant to simulate the brain.

Smith (1979) conducted direct cortical impact experiments where a small steel sphere was dropped on the cerebral cortex of both living and cadaveric (vessels perfused with saline and India ink for cadaver case) dogs. The sphere was dropped from various heights to determine what energy was required to cause extravasation. He reports no difference between living and cadaveric tests.

Marina (1989) attempted to determine the impact signature required to rupture blood vessels within the brain through the use of a physical model. Major cerebral arteries were obtained from human cadavers (in a fixed condition) and anchored within a plastic, water-filled cylinder. The system was then impacted sufficient to cause internal pressures as high as 20 MPa. While simulated vessels of wax paper could be ruptured, the arteries did not fail at these levels, presumably because the impact duration was too short.

Finally, Shreiber *et al* (1997, 1999) have studied contusions and the breakdown of the blood-brain barrier through vacuum-pressure induced direct cortical deformation of rat brain. The investigators used finite element modeling and experimental results to determine the strain tolerance for blood-brain barrier breakdown. Additionally, they showed that contusions play a minimal role in the generation of secondary injury.

2.5 SUMMARY OF PREVIOUS WORK

Substantial research has been conducted in the investigation of head injury. State-of-the-art computer models are growing more and more accurate in their ability to simulate head injury. Recent research suggests that the inclusion of the cerebral vasculature into these models will considerably increase their verisimilitude, but a complete set of properties for these tissues is not available. While some study of the vessels has been conducted, data from these investigations are not suitable for the development of a constitutive model that extends to failure. In the case of uniaxial tests on arteries, only major cerebral arteries have been investigated, with just a few tests to failure. For bridging veins, sub-failure behavior has not been reported, and the two investigations of this material disagree on significance of strain rate. Inflation tests have similarly been limited to major arteries, without any attention given to smaller ones. Additionally, no

measurements have been made on veins. In these cases, load levels have generally been limited to those encountered under normal physiological conditions, and parameters such as the incremental modulus have been the property of interest, rather than stress-stretch information representing the behavior of the vessels over a range of stretch. In nearly all mechanical property studies of the cerebral vasculature, vessels tested were obtained through autopsy.

3 Experimental Setup and Procedure

3.1 SPECIMENS

3.1.1 Human Vessels

Healthy human arteries and veins were obtained from the lateral surface of the temporal lobes of patients undergoing surgery to treat temporal lobe epilepsy, a disease which is not associated with changes in blood vessel mechanics. During the time of this study, the surgeries were performed at a rate of approximately twenty per year. In this procedure, a portion of the brain, with its accompanying blood vessels, is removed from the patient. Vessel segments from the area to be removed that had the least amount of branching along their lengths were selected for testing. Due to variations in vascular anatomy and brain resection sizes, some cases provided multiple specimens for study while others provided none. Resected segments were generally around 15 mm long. As indicated in Table 3.1, a total of 36 arteries and 34 veins (from 40 donors) were excised in surgery; age and sex of donors are also presented in the table.

Table 3.1 Human Donor Information (Number of Donors, Mean Age, and Percent of Male Donors) and Number of Specimens Obtained for Testing by Source and Type

	Healthy Vessels		Autopsy Vessels	
	Cortical		Cortical	
	Artery	Vein	Artery	Vein
Number of Donors	33	31	3	2
Mean Age (stdev)	33 (9)	34 (10)	51 (12)	49 (15)
Sex (% Male)	53	50	100	100
Number of Specimens	36	34	9	2

In order to investigate behavioral differences between fresh and cadaver tissue, blood vessels were also obtained through autopsy. As in the surgeries, cortical vessels were

resected from the lateral surface of the temporal lobe for direct comparison to fresh vessels. Multiple specimens could typically be taken in each autopsy case. Donor and specimen information for autopsy cases is also given in Table 3.1. Clearly, a significantly larger number of vessels was obtained from many more donors in surgery as compared to autopsy.

For the surgical specimens, signed, informed consent for the use of tissue was obtained from each patient using a protocol approved by the UCSF Committee on Human Research and by the UCB Committee for the Protection of Human Subjects. All specimens were obtained and tested according to the guidelines set forth by the National Institutes of Health on the protection of human subjects.

3.2 EXPERIMENTAL CONSIDERATIONS

3.2.1 Significance of Normal Stresses

While the cerebral blood vessels are undoubtedly under a state of multi-axial stress *in vivo*, stresses in the axial direction are hypothesized by the author to be the most important in the consideration of head injury, both in how the vessels interact with the surrounding brain material and in how the vessels fail. This is well accepted for gross displacements of the brain that result in the stretching of bridging veins. Even for cases where injury to the brain occurs through shear strains, however, it is here supposed that the vessels, in general, bend to carry loads axially. Thus, while some shear and bending loads develop, especially when the vessels are pressurized, the major resistance to loading is accomplished through axial stretch. Absent of internal pressure, the vessels, of course, have very little bending stiffness, but they are pressurized *in vivo* and studies have

shown that axial behavior is coupled with circumferential response (Zhou and Fung, 1997), so it is important to characterize axial properties at various internal pressures.

3.2.2 Accurate Measurement of Properties – Tissue Preparation

3.2.2.1 Tissue Storage and Testing Environment

The general rule regarding deterioration of blood vessels seems to be that mechanical properties are unchanged for a period of approximately 48 hours from the time of death (assuming storage in physiological saline solution upon removal from the body and cold storage for periods longer than a few hours). Chalupnik *et al* (1971) state this to be the case as though it is a result of their study, but it is not clear if this idea originated with them or somewhere else. Löwenhielm (1974) and Sato *et al* (1979) use this same methodology, again without providing justification from the literature. A more recent study by Brossollet and Vito (1997) indicates that mechanical properties of bathed vessels remain constant for a period of eight hours after death and that they are not consistently changed by cold storage over a period of several days.

With regard to testing environment, vessels are generally kept moist by or bathed in physiological saline to prevent shrinkage or swelling of tissue. Variations in the exact components of the solution seem to have no significant effect on properties of passive vessels. The same appears to be true for tests conducted at room as opposed to body temperature (Humphrey, 1995).

3.2.2.2 Vascular Smooth Muscle and TBI

Despite its important role in secondary injuries arising from head trauma (Boock, 1991), the influence of active smooth muscle is not considered in this investigation. In Boock's studies, rat femoral arteries and veins (in which smooth muscle viability had

been carefully preserved) were subjected to a brief, sub-failure stretch insult and then returned to their initial length. In seconds, the vessel diameter began to contract and a non-zero isometric axial force was measured. Since primary injury associated with trauma generally takes place at durations at least an order of magnitude less than that required for smooth muscle response, its influence in primary injury is considered to be insignificant. Tests in which investigators have included metabolic poisons in their physiological saline to inhibit active smooth muscle response give the same results as those using normal physiological saline (Humphrey, 1995).

3.2.2.3 Preconditioning

Blood vessels are under significant axial stretch *in vivo* and thus retract upon resection. It is generally agreed that this retraction is accompanied by a degree of restructuring (Fung *et al*, 1979) and that the process can be reversed, thus restoring the tissue to its *in vivo* structure, through a process called preconditioning. Preconditioning is accomplished by repeatedly cycling the tissue, both through axial stretch and pressurization, between its zero-load configuration and some target one until steady-state is obtained in the loading and unloading curves.

3.2.3 Non-Uniform Stresses

Because of the layered, inhomogeneous structure of blood vessels, the stress distribution through the wall is generally not uniform. This is complicated by the fact that if an arterial ring is cut, even when free of traction, it will open up, thus revealing the presence of residual stresses (Chuong and Fung, 1986; Vaishnav and Vossoughi, 1987). For the purposes of this study, however, mean stress will be reported.

3.3 TESTING APPARATUS AND PROCEDURE

Table 3.2 shows the number of each kind of test conducted by specimen type. The majority of vessels was clearly tested in the axial stretch mode. The few inflation tests are considered to provide a strong foundation for a future in-depth study of the multi-axial behavior of cerebral arteries and veins.

Table 3.2 Number of Tests by Specimen Type and Source

		Surgery Vessels		Autopsy Vessels	
		Cortical		Cortical	
		Artery	Vein	Artery	Vein
Axial Stretch	**Quasi-static**	14	11	8	3
	Dynamic	10	7	6	2
Inflation	**Quasi-static**	4	1		
	Dynamic	1	0		

3.3.1 Specimen Preparation

Prior to the resection of a chosen blood vessel, a piece of suture was placed alongside the portion of the vessel to be removed, as shown in Fig. 3.1, and cut to the length of the segment to provide a means for measuring the *in vivo* length. The samples were stored in physiological saline (0.15 M NaCl) at temperatures just above freezing during their transfer to Berkeley from San Francisco and until approximately 30 minutes before testing; measurements were typically performed within 4-5 hours of excision. In autopsy cases, time between death and tissue acquisition ranged from 20-30 hours.

Upon arrival in Berkeley, the excised length of each specimen was measured by means of a millimeter scale, and *in vivo* stretch was calculated as the ratio of the *in vivo* and excised lengths. It was not uncommon for some surrounding tissue, such as brain tissue or pia mater, to still be attached to the sample, so this was dissected away under a

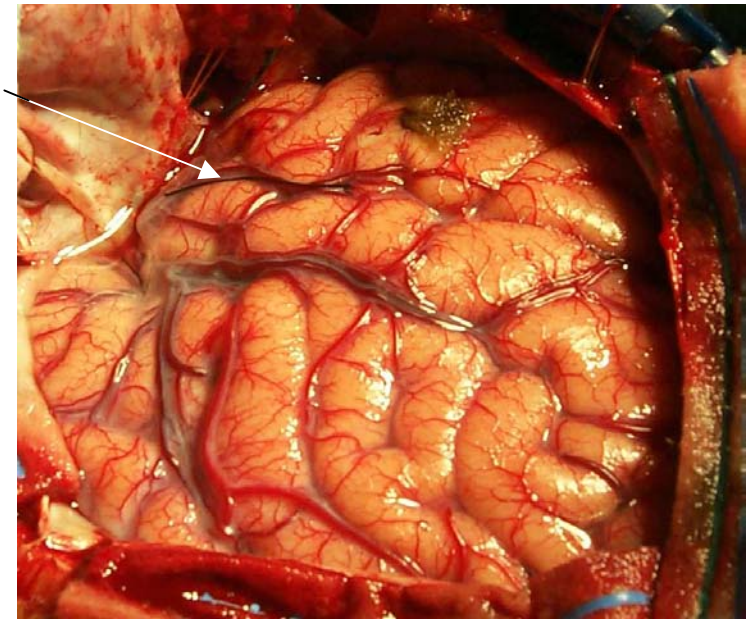

Figure 3.1 Surface of brain during temporal lobectomy surgery. Arrow identifies suture used for *in vivo* length measurement.

stereo microscope using a variety of micro-surgical tools. The vessel was then carefully inspected to identify any significant inhomogeneities like branch points or damaged regions. To permit the determination of stress and comparison of differently-sized vessels, cross sections were cut from the ends of each sample prior to testing to be measured. After testing of the larger segments, these sections were laid flat and their images captured to a computer by means of a CCD camera mounted on a microscope (100X). In a few cases, once an image of the intact cross-section was acquired, the section was cut radially and allowed to spring open to relieve most of the residual wall stresses. Images of these cases were also captured. Measurements of the digitized images, including approximate outer diameter, wall thickness, total area between inner and outer walls, and, where applicable, opening angle, were then conducted using dimension analysis software (Scion Image, Scion Corporation). For sections that were more

elliptical than circular, the major and minor axes were averaged as an approximation for diameter. Cross-sectional area was measured directly (rather than calculated using the approximate diameter) since the measurement software allows any shape to be traced and its area calculated. Thus, the outer and inner wall profiles were traced and their areas subtracted to determine total area. Where multiple cross-sections were available, results were averaged in an attempt to account for changes in geometry along the vessel length. Following the preparation of cross-sections, remaining specimen length was measured. Various stain (Sigma Nigrosin, Sigma-Aldrich Inc.) markings were then applied to each sample using a single strand of a brush to allow determination of stretch through video analysis.

3.3.2 Axial Stretch Testing

3.3.2.1 Apparatus

3.3.2.1.1 Quasi-static Tests

Static tests were conducted by means of a servo-hydraulic load frame (Model 858 Mini-Bionix, MTS). The main components of the system included the test frame, the digital controller, and a computer. The digital controller provided transducer excitation, signal amplification, and data acquisition for external signals along with the necessary instrumentation for actuator control. The controller was programmed using software provided with the system. While a variety of control modes were available for the machine's actuator, only position control was used in this study.

Specimen gripping was accomplished using two polyethylene flat-plate clamps, each with sandpaper on their inner surfaces to increase holding capacity, as shown in Fig.

(a)

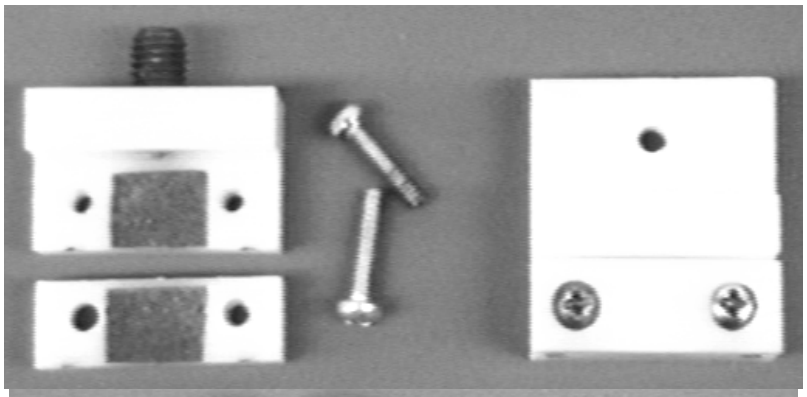

(b)

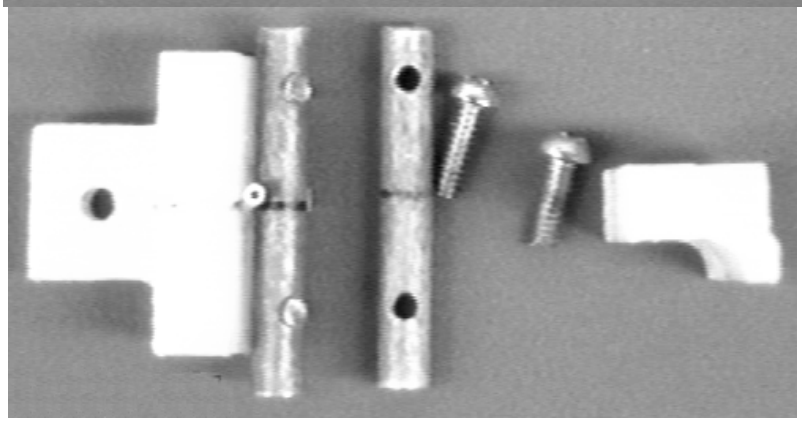

Figure 3.2 (a) Flat and (b) cylindrical clamps for the testing of small blood vessels. Width of clamps is 25 mm. Each image shows one clamp assembled and one disassembled. In (b), the assembled grip holds a piece of silicon rubber tubing

3.2(a). As flat clamps are prone to cause premature material failure at the clamp-specimen interface due to stress concentrations and one of the major objectives of this study was the measurement of failure properties, an alternative to the first clamping solution was tested and shown to promote failure in midsection. As seen in Fig. 3.2(b), these clamps featured two small cylinders, around which the specimen was wrapped before being clamped. Figure 3.3 demonstrates the effectiveness of the alternative design on silicon rubber tubing, with premature failure obviously occurring in the flat clamp cases. This solution, however, required greater vessel lengths than were generally available and thus could not be used.

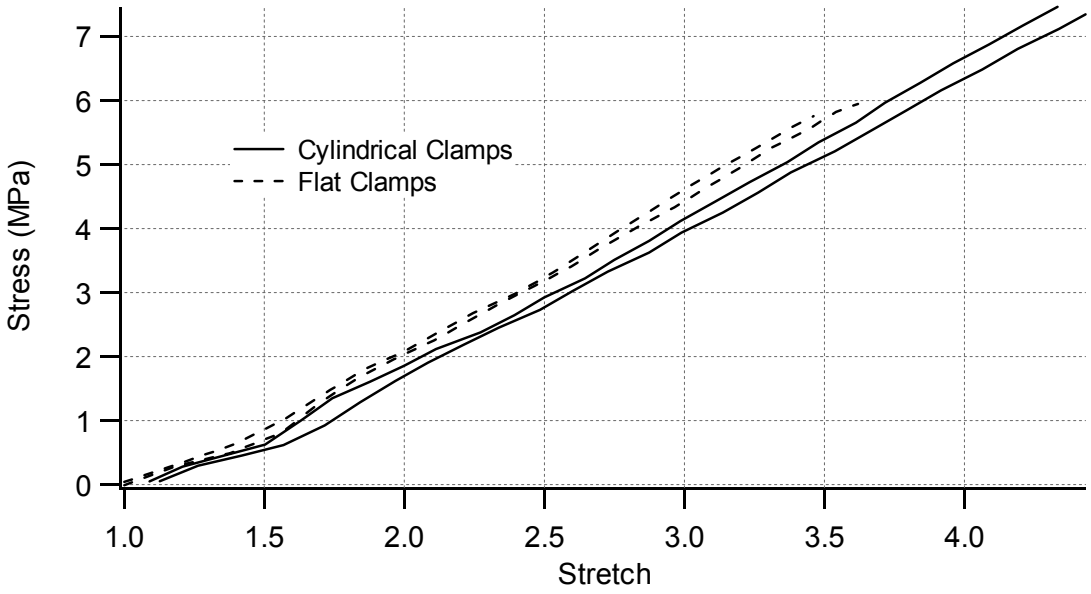

Figure 3.3 Stress-stretch results from extension tests on silicon rubber tubing using flat and cylindrical clamps

Applied loads were measured using either an 11 or a 45 N capacity load cell (MDB 2.5, MDB 10; Transducer Techniques), and deformations were obtained by means of the on-board LVDT and a Hi8 video camera (ES4000, Canon) operating at 30 pps.

3.3.2.1.2 Dynamic Tests

For the dynamic test, strain rates at least three orders of magnitude higher than those utilized during the quasi-static tests (0.01-0.10 s^{-1}) were desired. Two separate testing arrangements were utilized. In the first, a 1.8 kg steel sphere was dropped onto a 0.6 m long rectangular aluminum beam (of cross section 6 x 25 mm) from a height which was selected as a function of the length of the specimen to produce constant strain rates of the order of 100 s^{-1}. A photograph of the dynamic experimental arrangement is shown in Fig. 3.4. The beam was initially in a horizontal position, pinned at the distal end to a heavy stand that was mechanically isolated from the load cell to minimize noise due to

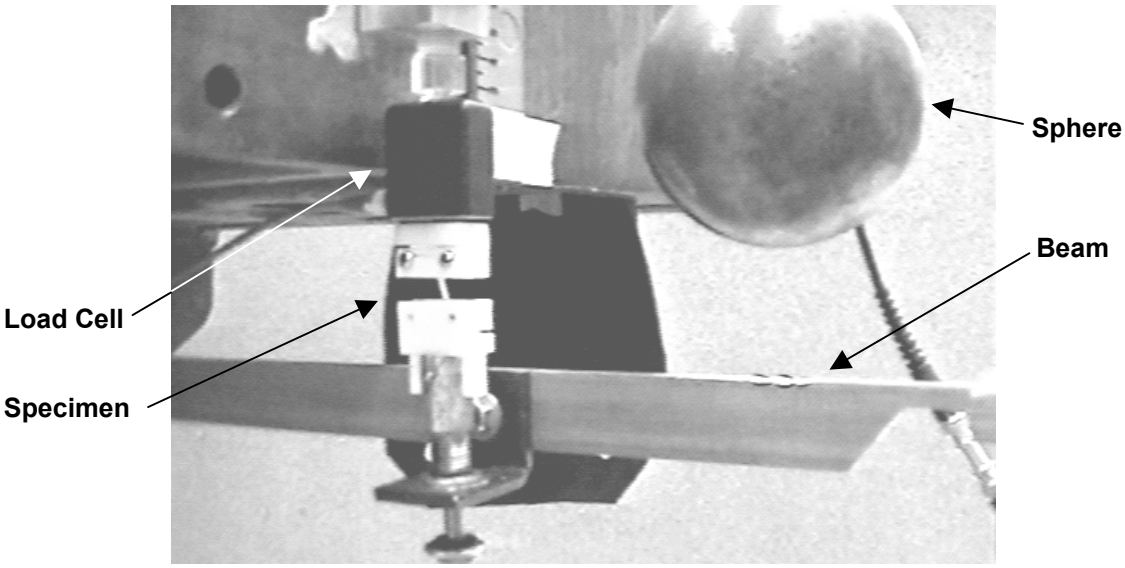

Figure 3.4 Photograph of sphere-beam impact dynamic testing setup

vibrations from the impact. The other end of the beam, 20 mm from the impact point, was connected to the head of a tripod by means of a frangible wooden support which broke upon contact. The top of the specimen was held rigidly to the load cell while the lower end was only loosely connected to the beam by means of a bolt, as shown in the photograph. The lower grip initially rested on the beam and, due to its loose connection to the beam, did not move significantly until the impact-accelerated beam contacted the bolt head. This arrangement ensured that the beam absorbed the initial impact without loading the specimen, thereby producing a constant rate of extension. Although the gross motion of the end of the beam was rotational, the short travel that occurred before specimen failure was essentially linear. The same load cell and grips that were used in the static tests were also employed here. An amplifier / conditioner module (TMO-1, Transducer Techniques) was used in conjunction with the load cell, providing a two-pole Butterworth low-pass filter with a cutoff frequency of 2200 Hz. The motion of the lower grip was recorded using an optical displacement follower (Opt-Follow, Yaman.

Instructions for the operation of this device can be found in Brunette, 1988). Specimen deformation was also monitored using a high speed video camera (Spin Physics 2000, Kodak) operating at 2000 pps. Data collection was triggered when the sphere interrupted the path of a laser just prior to impact.

The second dynamic test arrangement was designed in an attempt to overcome some shortcomings of the first setup. In the first case, preconditioning was accomplished by manually adjusting the height of the tripod supporting the beam, resulting in an inability to precisely specify the extent of preconditioning. Further, despite attempts to minimize load cell vibrations due to the impact, some noise was still present in the recorded data that made analysis difficult. The second apparatus was designed to work in conjunction with the servo-hydraulic load frame and to execute both quasi-static and dynamic tests. As Fig. 3.5 shows, a high-density polyethylene (HDPE) lever was pinned at one end,

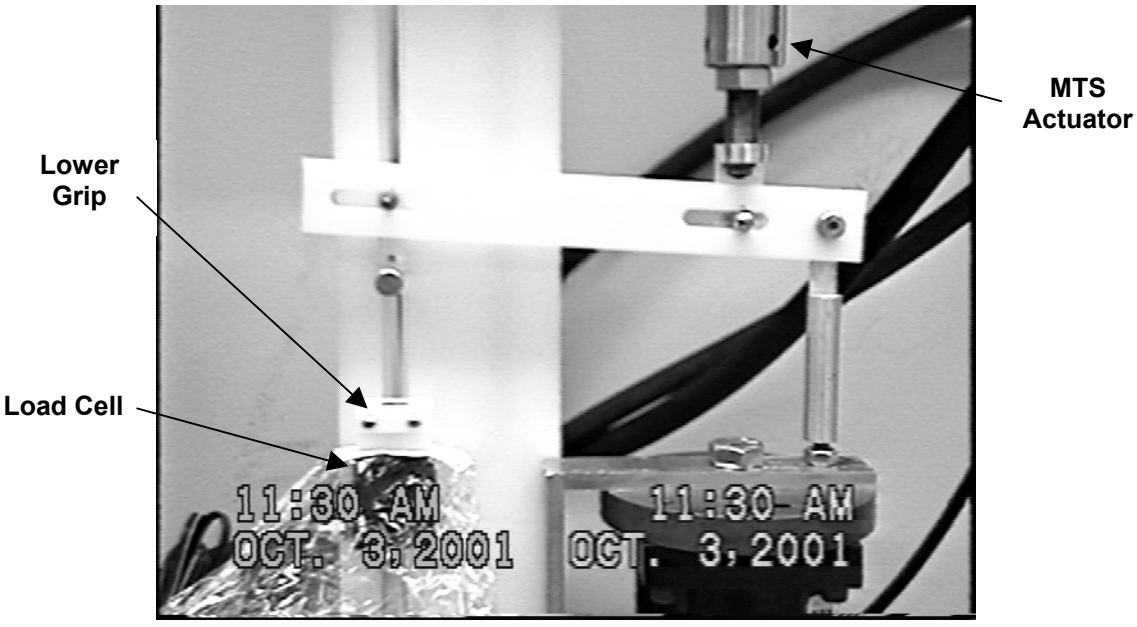

Figure 3.5 Velocity multiplier device for use in conjunction with MTS load frame. Load cell is covered with plastic wrap. Upper grip and specimen are not shown.

attached to the machine actuator via one pin-slot interface, and connected to the grip at the top of the specimen through another pin-slot interface. Lever dimensions were designed such that velocity at the specimen connection was nearly five times greater than that at the actuator. Since the maximum velocity at the actuator was 267 mm/s, the largest speed of the upper grip was limited to 1335 mm/s. The design provided for a constant velocity at the specimen connection when the actuator velocity was constant. The specimen connector sat within a slot in the HDPE backing, constraining its motion to the vertical direction. As seen in Fig. 3.6, the pin-slot interfaces were constructed with fixed dowel pins inside bushings that slid and rolled within the plastic slots, reducing the tendency for the metal to dig into the plastic. Control of the actuator for desired motion and acquisition of load and position data were accomplished using the load frame system. The standard and high-speed video cameras previously described were used to verify motions as appropriate.

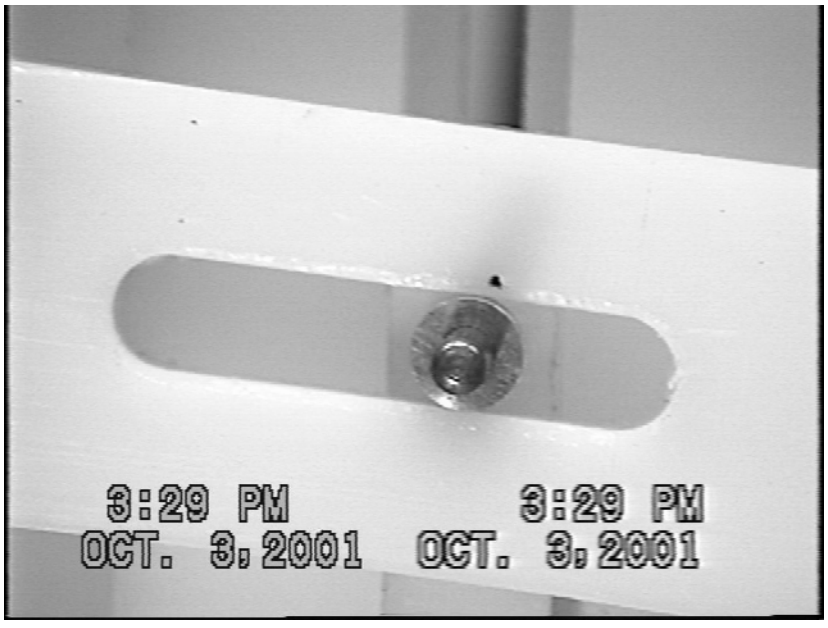

Figure 3.6 Close up of one slot-pin interface on the velocity multiplier used with the MTS load frame for dynamic testing

3.3.2.2 General Procedure

In order to encourage midsection failure with the flat clamp grips, following the lead of Lee and Haut (1989), vessel ends were air dried before gripping since the strength of collagen increases significantly when it is dried. Once the specimen was prepared, one end was fastened into the upper grip, which was then attached to the actuator. The device was then lowered manually until the bottom end of the vessel was between the jaws of the lower clamp, which had previously been fixed to the load cell. The lower grip was then tightened around the lower end of the vessel. This loading technique was utilized instead of first gripping both ends of the vessel and then transferring it to the machine since any relative motion of the grips during the process could damage the fragile specimen. In addition, the chosen process simplified starting the test at the vessel's no-load length, allowing calibration of the zero load level, and improved specimen alignment.

Prior to testing to failure, each specimen was subjected to at least ten cycles of quasi-static extension between the initial no-load condition and the calculated *in vivo* stretch. In some cases, this procedure was combined with a stress-relaxation process where the vessel was stretched to its *in vivo* length and held for five minutes. Following preconditioning, each vessel was stretched longitudinally to structural failure. In quasi-static tests, the stretch rate was constant on the order of 0.1 s^{-1}; in dynamic drop tests, an initial small, variable loading rate (associated with the lower grip beginning to fall after the beam had moved) of approximately 10% of the ultimate stretch was followed by a constant rate (after the beam had contacted the bolt head) to failure, on the order of 200 s^{-1}, so that these experiments can be considered to have been conducted at constant strain rate. The dynamic lever setup produced a quadratic displacement-time trace throughout

most of each test period so that a constant strain rate was really never achieved. Maximum rates for this device were slightly less than in the drop test, producing strain rates around 75 s^{-1}. All vessels were kept moist during the entire test sequence by periodically spraying saline solution on the samples. As standard video cameras record with more pixels in the horizontal than vertical direction, the video camera was rotated ninety degrees to increase image resolution for quasi-static tests.

3.3.3 Inflation Testing

3.3.3.1 Apparatus

Because the clamps applied in the axial stretch tests did not allow inflation of blood vessels, a new loading apparatus was constructed. The device was designed to interface with the servo-hydraulic tester and allow simultaneous inflation and axial stretch. As shown in Fig. 3.7, the inflation apparatus included two blunt tip stainless steel needles extending from acrylic manifolds to cannulate the vessel ends, providing a fluid pathway through the vessel. A variety of luer-hubbed, blunt tip needles, with outside diameters ranging from 0.305 to 1.778 mm, were easily interchanged to accommodate various vessel diameters. One manifold was constructed to connect to the actuator of the testing machine, while the other attached to the load cell. Each one had two holes intersecting the fluid pathway associated with the needles. A 207 kPa pressure sensor (MicroSwitch 26PCDFM6G, Honeywell) and a stopcock were attached to the actuator manifold at these locations, while two stopcocks filled the holes on the load cell manifold. The pressure sensor signal was amplified (TMO-1, Transducer Techniques) prior to being recorded by the test system's data acquisition unit. One of the stopcocks on the load cell manifold was connected to a syringe through stiff polyethylene tubing, allowing fluid to be pushed into

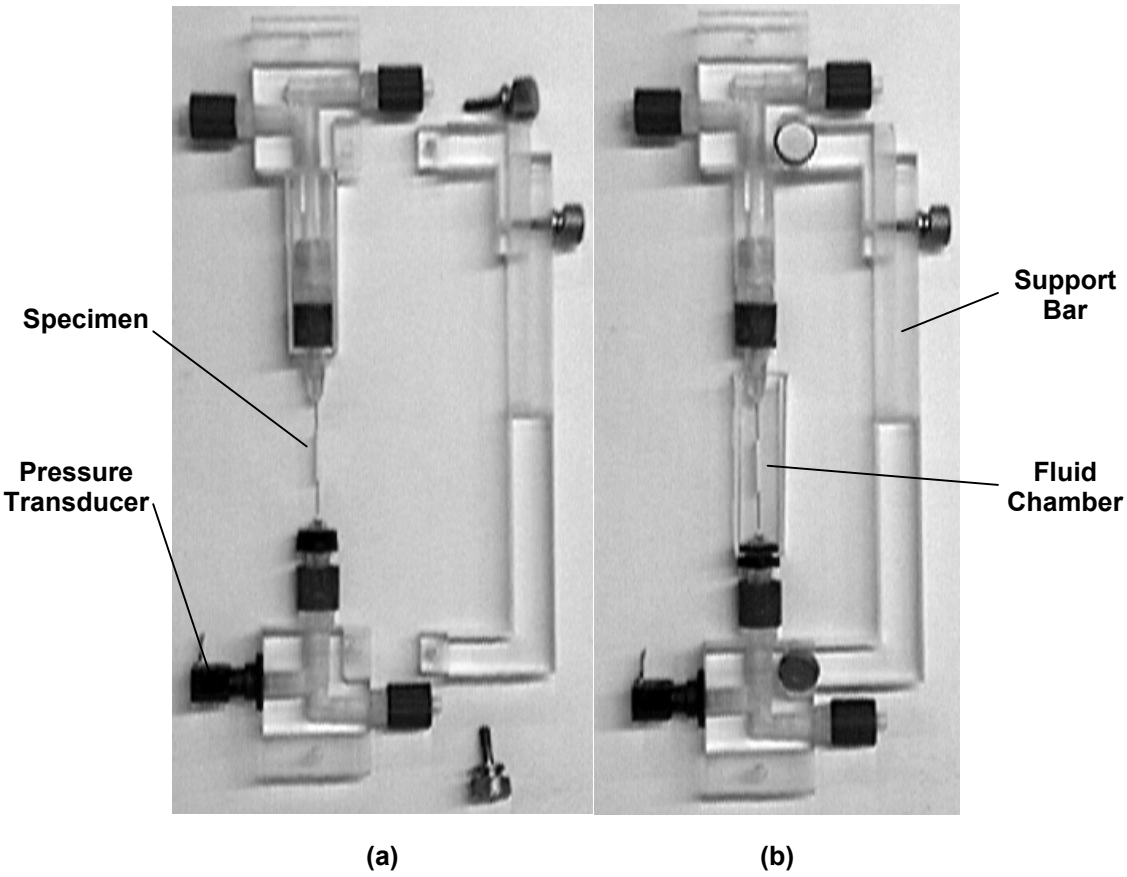

Figure 3.7 Photographs of the inflation apparatus with a piece of silicon rubber tubing attached to the needles. The support bar is unattached and the fluid chamber retracted in (a).

the mounted specimen. As shown in the figure, a cuvet (best described as a square test tube) with a hole milled through its base was used as a bath and containment chamber. The square tube was sealed around the hub of the lower needle with a short, wedge-shaped cylinder constructed from a rubber stopper and could be slid up around an extension tube between the actuator manifold and its needle in order to allow access to the specimen. Finally, to protect the specimen during mounting, the manifolds were designed to be rigidly coupled to one another through an adjustable support bar that was removed after the system was attached to the load frame before testing began.

The pressure sensor amplifier and devices required to produce inflation were mounted to a wooden board, as shown in Fig. 3.8. The body of a plastic syringe was connected to a block that was mounted in a slot on the board, while the syringe piston was attached to the end of a stepper motor-driven linear actuator (Digit, UltraMotion) mounted to the same board. The stepper motor was controlled by a programmable step motor driver (3540i, Applied Motion Products), and the position of the actuator, measured by an on-board potentiometer, was recorded by the test system along with the other data. A range of possible actuator speeds (from quasi-static to over 120 mm/s) and two different sizes of syringe allowed execution of either quasi-static or dynamic inflation.

With the specimen mounted in the test frame and connected to a fluid source, the setup provided multi-axial testing capability. Axial load was measured as in the 1-D stretch tests. Deformation, both axial and circumferential, was monitored using an

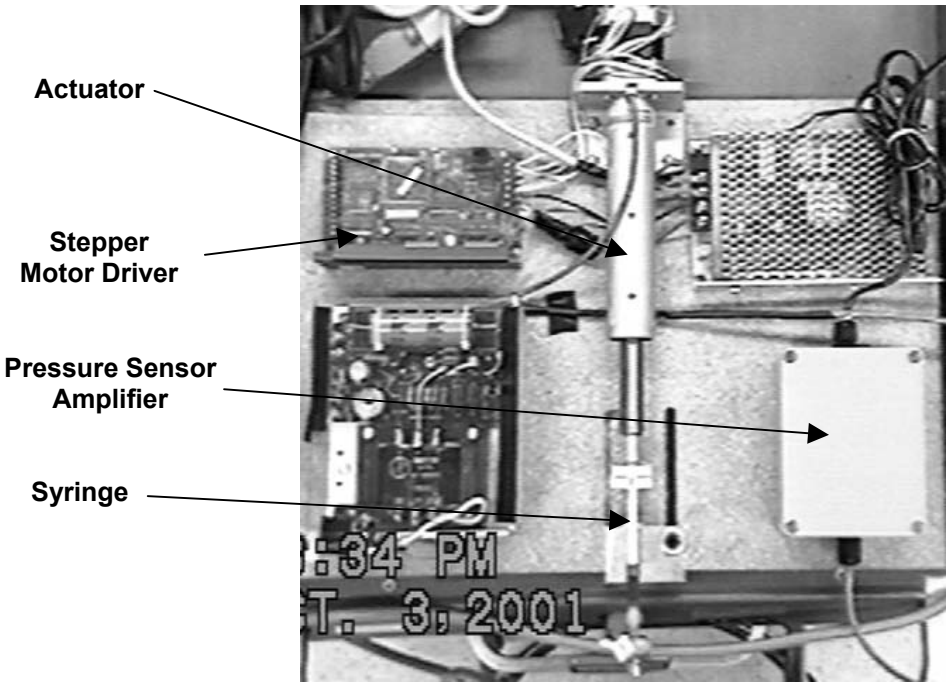

Figure 3.8 Inflation test equipment board including syringe, actuator, stepper motor driver, pressure sensor amplifier, and power supplies

appropriate-speed video camera. A standard camera close-up lens (Promaster) was attached to the lens of the Hi8 video camera to produce an image resolution of 20 μm/pixel. Specimens were pressurized using saline that had been dyed blue using food coloring, while the bath saline was clear. Thus, if the vessel happened to leak within the field of view of the camera, the location of the leak could be identified. Because of the near-transparency of the small vessels, the blue saline also provided needed contrast to identify the vessel's boundaries and enhance their measurement. A yellow background was utilized to contrast with the blue color.

3.3.3.2 Procedure

Once a specimen had been prepared for testing, it was compared to needles of various sizes under a stereomicroscope. A needle size was chosen that appeared to best approximate the inside diameter of the vessel. The selected needles were attached to the manifolds, which were then connected using the support bar. Each manifold and needle was filled with physiological saline, with care taken to remove air bubbles, and the assembly was placed upon a mounting plate under the microscope. The mounting plate was flat except for a raised platform at its center that was approximately the same height as the needles when the assembly was laying flat. During mounting, the blood vessel was placed upon this platform in a small pool of saline and was carefully pulled over the end of one of the needles using microforceps. A length of monofilament suture was then tied around the vessel and needle. High gauge (40 AWG) wire was also sometimes used for this purpose. The same procedure was repeated on the other end of the specimen, and the length of the adjustable support bar was fixed to protect the vessel from inadvertent stretching. When branches were present on the specimen, either the vessel was positioned

to place the branch outside the sutures or the branch was occluded with glue. A small amount of tissue cyanoacrylate (VetBond, 3M) was applied around the specimen ends to better secure them to the needles and to provide a better seal for inflation. Special care was taken to keep the glue from spreading over the body of the specimen. Because the friction between the needle and the blood vessel was minimal and the bond created by the glue was relatively weak, a small epoxy bulb was formed around the outside of a few needles, near their ends. Specimens for which significant axial forces were planned were then pulled over the bulb and a suture tied around them to minimize slippage.

Once the vessel was properly secured to the needles, one stopcock on each manifold was opened and fluid was pushed through the system to verify that the vessel could sustain at least a small amount of pressure. The assembly was then oriented upright, and the containment chamber was lowered and sealed at its base. Petroleum jelly was used to enhance the seal. The chamber was then filled with saline solution.

To connect the structure to the load frame, the upper manifold was first attached to the actuator. The actuator was then carefully lowered until the lower manifold nearly contacted its connection to the load cell. The screw fixing the length of the support bar was then loosened, allowing the lower manifold to slowly drop until it rested on the load cell connector. In order to avoid any significant stretching of the blood vessel, care was taken to position the lower manifold close to the load cell connector before releasing the support bar. Once the lower manifold was attached, the actuator was adjusted downward to relieve tension on the specimen, and the support bar was detached from both manifolds. With the manifolds in place, the pressure transducer cable and pressurizing tube were attached, the load cell and LVDT signals were zeroed, and the video camera

was adjusted. The stopcock on the upper manifold was then opened, and a small amount of fluid was again pushed through the system to verify proper attachment. The stopcock was then closed and the pressure sensor signal was zeroed.

As with the axial stretch testing, the vessels tested in inflation were also preconditioned prior to testing. In this case, however, the apparatus allowed multi-axial preconditioning, more accurately mimicking *in vivo* conditions. Prior to failure testing, each vessel was subjected to an *in vivo* axial stretch accompanied by pressures around 100 mmHg for arteries and 8 mmHg for veins. These deformations were held for a minute or so, accomplishing the conditioning process through stress-relaxation rather than cycling. After the preconditioning process, the specimen was returned to its zero-load state and then subjected to a failure sequence, which consisted of holding the vessel length constant at some chosen value while pressurizing to failure.

3.3.4 Histology

For many of the cases, post-test specimens, along with their pre-test cross-sections, were stored in 10% neutral-buffered formalin (Accustain, Sigma Diagnostics) and later studied using standard histology techniques. The tissue was first processed by immersion in various concentrations of ethyl alcohol to dehydrate it, followed by xylene to remove the alcohol and then melted paraffin to prepare the vessel for embedding, as outlined in Appendix A. After processing, the samples were embedded in paraffin blocks and sliced (8 um thick) using a microtome. Selected slices were put into slides and stained with hematoxylin and eosin, which stain cell nuclei and fibers, respectively. Images of the resulting slides were then captured to a computer using a microscope. Originally, these sections were to be measured and compared to results on non-fixed sections as a means

of validation, but as Hart *et al* (1983) have shown that vessel morphology is not preserved when formalin is used, the sections were only used to compare arterial and venous structures.

3.3.5 Data Processing and Analysis

Load and grip displacement data were used to calculate axial stress and stretch, along with failure values, for the specimens. Video recordings of tests were transferred from the analog video camera used to record tests to a digital video camera (DCR-TRV900, Sony) and captured to a computer using a digital video transfer board (DV300, Pinnacle Systems) and video editing software (Adobe Premiere, Adobe Systems). Images from the recordings were used to check for stretch homogeneity between the grips in order to justify the use of the LVDT data (or optical displacement follower data for some dynamic tests) for axial stretch calculations. In cases where stretch was not uniform, displacements between stain marks or natural landmarks on the vessels were used to calculate local stretches. For inflation tests, the captured video images were further utilized to track the change in the diameter of the vessels. This information, along with the recorded internal pressure measurements, was used to determine the stress-stretch behavior of the vessel in the circumferential direction. In all cases, data obtained through video analysis and that measured directly were time-correlated by identifying the first image in which axial motion of the grip occurred. In tests where no axial motion was required, a small displacement cycle (of around 1 mm) was conducted prior to the test to provide means for synchronization.

3.3.5.1 Kinematics and Equations for Stress and Stretch

In order to calculate stress and stretch from the recorded data, it is necessary to develop the kinematics associated with extension and inflation of a blood vessel segment. The reference configuration is taken as a circular cylinder, with concentric cylinders mapping into concentric cylinders. The deformation is assumed to be uniform through the wall and along the length of the segment. While it is well established that blood vessels usually contain residual stresses as unloaded cylinders (Chuong and Fung, 1986; Vaishnav and Vossoughi, 1987), the thin wall assumption will later be applied, which makes the motion from an unstressed sector into an unloaded cylinder inadmissible (Holzapfel *et al*, 2000). As a result, the derivation here begins in the unloaded state and proceeds into the stretched, inflated one, as shown in Fig. 3.9. Descriptions for the position vectors in each of these configurations are included in the figure, with unit

$$\mathbf{F} = \frac{\partial r}{\partial R}\mathbf{E}_R \otimes \mathbf{e}_r + \frac{r}{R}\mathbf{E}_\Theta \otimes \mathbf{e}_\theta + \lambda_z \mathbf{E}_Z \otimes \mathbf{e}_z \tag{3.1}$$

vectors applying to the radial, circumferential, and axial directions. R and Z are radius and length in the reference configuration, while matching lower case letters represent the same parameters in the loaded state. Given these position vectors and applying the methods of finite elasticity, the deformation gradient **F** is defined by Equation 3.1, where $\lambda_z = z/Z$ and $\mathbf{E}_\mathrm{A}$ and $\mathbf{e}_\mathrm{i}$ are unit vectors in the reference and current configurations, respectively. The vessel is assumed to be orthotropic with unit vectors aligned with the principal directions. Due to assumed material symmetry, the unit vectors in the two configurations are equivalent, and the elements of the deformation gradient tensor are the principal stretches, λ_r, λ_θ, and λ_z, in their respective directions.

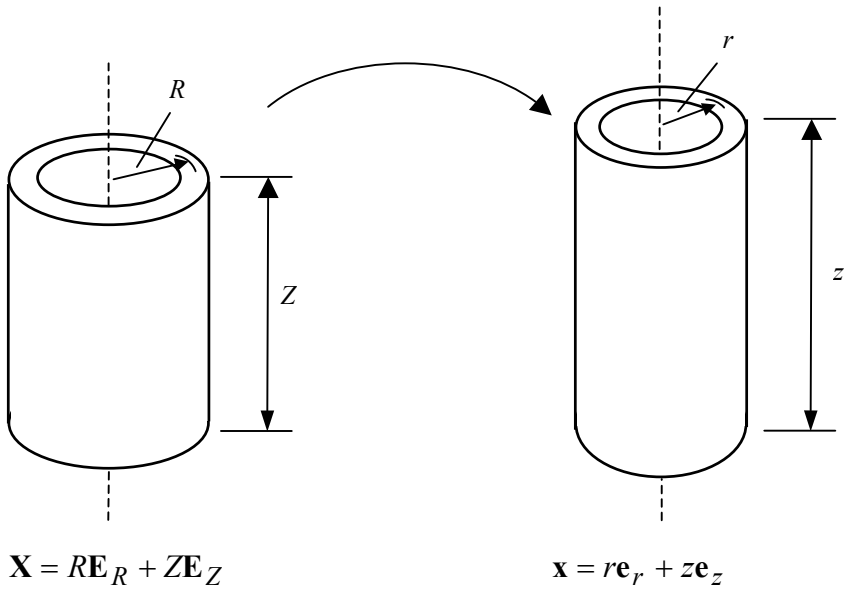

Figure 3.9 Kinematics of combined extension and inflation. Vectors identify the position of any given material point in the reference and after deformation.

All stresses were calculated in the form of the First Piola-Kirchhoff stress **P**, defined as current load divided by reference cross-sectional area. Thus, for uniaxial tests, the longitudinal stress P_{zz} was determined as the ratio of axial load to the unloaded cross-sectional area. In inflation tests, however, the measured axial load is affected by the vessel internal pressure as well as by stresses in the vessel wall. Equilibrium in the axial direction reveals that $F = P_{zz}\widetilde{A} - \pi r_i^2 p$, where F is the measured axial load, $\widetilde{A}$ is the reference area, r_i is the vessel internal radius, and p is the vessel internal pressure. Axial stress for inflation tests, then, was determined using this relationship and assuming that the vessel internal radius could be adequately represented by the vessel external radius which was measured from video. For the calculation of axial stretch λ_z, reference length was defined at the point where an increase of load was first noted during the test to failure (like Mohan and Melvin, 1982, 1983). While this approach seemed sufficient for

quasi-static tests, the measured load during some dynamic ramps did not rise from zero until displacements greater than those where load increased during the final cycles of preconditioning. In these cases, noise was considered to have partially corrupted the signal, and the displacement associated with load rise during the last cycle of preconditioning was taken to be the reference length.

The circumferential stress $P_{\theta\theta}$ was calculated assuming that the vessel wall was thin enough that stresses did not vary significantly through the thickness of the wall and that the measured diameter data adequately represented the mean diameter. With these assumptions, global equilibrium in a transverse section gives the Cauchy stress $T_{\theta\theta} = pr/h$, where p is the internal pressure and r and h are the vessel mean radius and thickness of the wall, respectively, in the current configuration. Using the relation between the Cauchy and First-Piola Kirchhoff stresses ($\mathbf{T} = (1/J)\mathbf{P}\mathbf{F}^T$) and the assumption of incompressibility (since h was not measurable), the circumferential stress may be written as $P_{\theta\theta} = (r\lambda_z / H)p$, where H is the wall thickness in the reference configuration. The reference diameter for calculation of circumferential stretch λ_θ ($= r / R$) is identified in similar fashion as the reference length. Stresses in the radial direction were assumed to be negligible.

3.3.5.2 Characterization of Longitudinal Stress-Stretch Data

Once the stress-stretch behavior of each specimen was determined, the data were described using a series of parameters. The low stress portion of the curve, referred to as the toe region, was fit by the exponential form given by Equation 3.2,

$$P_{zz} = \frac{B}{A}(e^{A(\lambda_z - 1)} - 1) \tag{3.2}$$

which follows from Equation 2.1 by requiring $P_{zz}(\lambda_z=1) = 0$. As indicated in Chapter 2, A and B are constants. B is the slope of the curve at $\lambda_z = 1$ while A determines the degree of curvature. Curves were fit using the Levenberg–Marquardt algorithm, a form of non-linear, least-squares fitting, to minimize chi-square (Igor Pro, Wavemetrics). As is indicated by Equation 2.1, the toe region can be identified by the portion of the curve for which $dP_{zz}/d\lambda_z$ v. P_{zz} is linear. Using this as a guide, the length of the toe region, λ_T, was thus defined as the largest domain over which Equation 2.1 accurately represented the data. The equation requires the stress to be zero for a unit stretch.

Figure 3.10 illustrates the parameterization of an example curve. While the yield point is not as clearly defined for soft tissue as for some other materials, it was defined here as the point where the stress-stretch curve attains its maximum slope, as shown in the figure. Maximum slope, or the elastic modulus at yield, Mod_Y, and yield stress σ_Y and

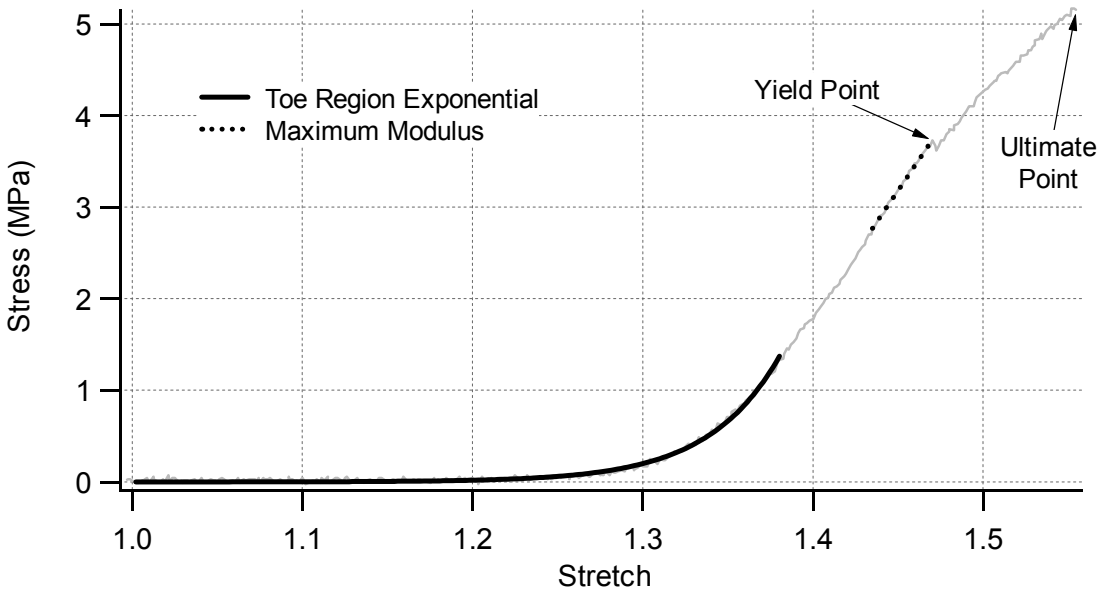

Figure 3.10 Parameterization of example case

stretch λ_Y were recorded for this location. Finally, since in most cases the maximum slope occurred at some point below the maximum load, ultimate stress σ_U and stretch λ_U were identified by the largest stress obtained during the test.

3.3.5.2.1 Statistical Analysis

For a statistical analysis of data from the described tests, the eight curve-characterizing parameters (λ_T, A, B, λ_Y, σ_Y, Mod_Y, λ_U, σ_U) were considered to be dependent variables, with all other variables defined as independent. The list of considered independent parameters included vessel type (artery or vein), vessel source (surgery or autopsy), testing rate (quasi-static or dynamic), age and sex of donor, specimen dimension measurements (cross-sectional area, approximate outer diameter, wall thickness), *in vivo* stretch, time from resection to testing, gauge length, extent of preconditioning prior to testing, location of failure (near end of specimen or in midsection), and type of grip (flat clamps or needles). Multivariate analysis of variance (MANOVA) was utilized to measure the significance of differences between the curve parameters for changes in the independent variables.

Among the many independent variables, vessel type, vessel source and testing rate were of particular interest. The experiments were designed to address their significance, and analysis of overall stress-stretch results seemed to confirm their importance. In order to determine what variables besides these should also be included in the final model, exploratory MANOVA tests of the final data set were conducted using models that considered these three main independent variables along with one of each of the remaining independents. Different models were produced in which the effect of the selected variable was considered on the three main independents, interactions between

the main independents and the variable of interest, and interactions between the main independents. In general, effects were considered to be significant when they were associated with p-values less than 0.05. Upon generation of results from the final model, joint confidence intervals for the various dependents were plotted for variations in the independents, thereby checking the validity of the model design. As a matter of interest, potential dependence among the dependent variables was also analyzed.

3.3.5.2.2 Dynamic Test Vibrations and Modeling

Dynamic tests generally resulted in relatively noisy load data in comparison to quasi-static tests. The noise was considered to be partly associated with impact wave propagation for the first dynamic testing apparatus and with machine vibrations for the load-frame dynamic setup. Where vibrations were considerably higher than the time scale of the measured data, noise was reduced using a binomial smoothing (Gaussian filtering) algorithm (Igor Pro, Wavemetrics), and the resulting data were then parameterized. In the few cases where vibrations from these sources of noise were on the same time-scale as the measured data, it was impossible to remove the noise and the data were not included in analysis.

Another source of noise determined in the data, however, was the dynamic response of the load cell itself. The two load cells utilized in testing are specified to have ringing frequencies at 575 and 1400 Hz for the 11 and 45 N capacities, respectively. Despite the fact that the elements within the load cells are orders of magnitude more stiff than the tested vessels, any loading that excites these frequencies produces oscillations of a portion of the sensor's mass. As a result, the measured load is not necessarily equivalent to the force developed in the blood vessel at a given time, possibly leading to erroneous

conclusions regarding a specimen's behavior at high rates. In order to determine the significance of these oscillations in the present tests, a simple spring-mass model was proposed to represent the vessel-grip-load cell system. The load cell was modeled as a spring that was rigidly fixed at one end and connected to a mass at the other end, as shown in Fig. 3.11. While the exact construction of the load cell is proprietary, it is known that the sensing element is made of one piece that has been machined down and mounted with strain gauges at a chosen location. This reduced area effectively separates the sensing element into two mostly non-deforming pieces, one that remains fixed and one that moves in response to generated loads. The moving piece was represented by the mass in the model. As shown, the modeled mass was also attached to a spring representing the blood vessel, through which loads are applied to the system. The resulting differential equation is given in Equation 3.3,

$$m\ddot{x}_1 + kx_1 = F(x_2 - x_1) \tag{3.3}$$

where m is the sum of the masses of the moving portion of the load cell and the attached grip, k is the stiffness of the sensing element in the load cell, and $F(x_2\text{-}x_1)$ is the force

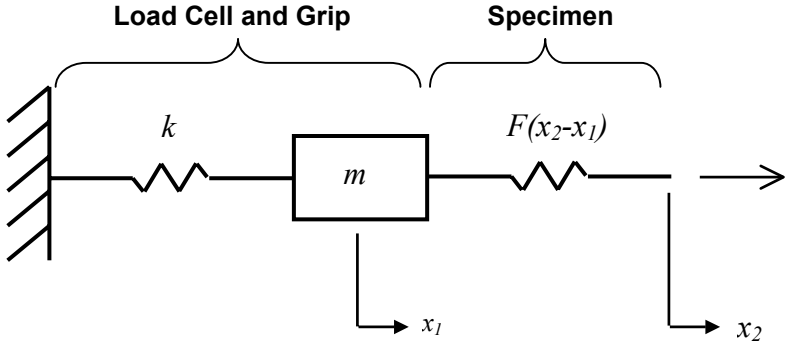

Figure 3.11 Proposed dynamic model for load cell - grip - vessel system

response of the spring representing the vessel. As the symbol suggests, the load cell spring was linear, with the value of k calculated as the ratio of load capacity to specified full scale deflection. While the portion of mass m due to the grip is easily determined by weighing the grip, the fraction attributable to the load cell must be calculated. If only the load cell portion of the spring-mass model shown in Fig 3.11 is considered, oscillations are described as simple harmonic motion and are governed by Equation 3.3, except with the right side equal to zero (and with a reduced mass m' since the influence of the grip has been momentarily omitted). For simple harmonic motion, the expression $\sqrt{k/m'}$ is equal to the circular frequency ω ($\omega = 2\pi f$), where f is the frequency. Thus, the load cell's oscillating mass may be calculated as $m' = k/(2\pi f)^2$, with k as calculated above and f the specified ringing, or natural, frequency. As demonstrated in Fig 3.12, which shows the measured load cell response to an impulse, the real system clearly contains

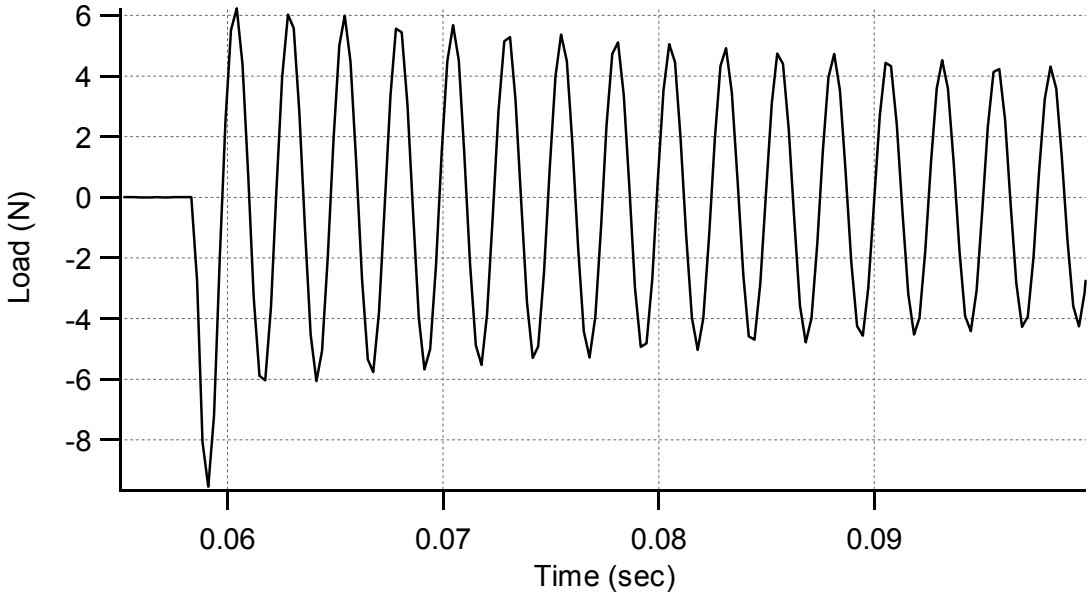

Figure 3.12 Impulse response of 10 N load cell

some damping, but it was considered to be insignificant for the very short time under consideration in the dynamic vessel tests. This assumption was confirmed when the load cell oscillating mass was calculated both with and without the grip attached, and the difference between the two calculations was equivalent to the measured grip mass. The oscillating load cell mass was thus calculated as shown and added to the value of the grip mass for use in Equation 3.3. Specified values for capacity, full-scale deflection, and ringing frequency for the two load cells are summarized in Table 3.3, along with calculated stiffness and oscillating mass. The grip that was attached to the load cell during tests had a mass of 10 grams.

Table 3.3. Specified capacity, full scale deflection, and ringing frequency for the 11 and 45 N load cells, along with calculated values for stiffness and oscillating mass

	11 N Load Cell	45 N Load Cell
Capacity (N)	11.12	44.48
Full scale deflection (mm)	0.0103	0.0103
Ringing frequency (Hz)	575	1400
Stiffness (N/mm)	109.45	437.80
Oscillating mass (grams)	8.4	5.7

With the above values calculated, the load response of the spring representing the blood vessel still needed to be specified in order to allow solution of Equation 3.3. As finding the vessel response was the objective of this exercise, and the measured load cell response for any given dynamic test was known, it was hypothesized that when an accurate representation of the blood vessel was made, the response of the load cell, as calculated using the model, would match the measured load during the actual test. Because such an approach is iterative, a program was written using Matlab (The Mathworks, Inc.) and its differential equation solving capabilities. Following the

approach by which the stress-stretch curves were parameterized for analysis, the candidate response function was chosen to be a combination of an exponential function in the low-stress region, a linear function at higher stresses, and a quadratic function above the yield point. The values of the functions, as well as their derivatives, were required to be equal at each transition point. Because of the transition constraints, only the coefficients in the exponential function and one parameter in the quadratic expression could be freely specified. Times at which the transitions occurred were also defined by the programmer. For a chosen experiment, the program was written to read in the measured displacement-time curve of the actuator (x_2 in Equation 3.3) so that the exact loading applied in the test could be applied to the model. Force-time data from the experiment were also read in and used to compare to the calculated load from the model. Once a suitable match was achieved, the calculated vessel response was considered to accurately portray the behavior of the vessel in the experiment. The program additionally allowed for specification of a failure time, after which the calculated response was based upon the free oscillation of the load cell. The series of equations utilized to represent the blood vessel, along with the constraints required at the transitions, are outlined in Appendix B. The m-files used in Matlab are also included there.

3.3.5.3 Multi-Variate Curve-Fitting

Even though only a small number of inflation tests were conducted, data from these tests were used to evaluate the ability of a selected existing constitutive model to fit the measured behavior. A two-dimensional model proposed by Fung *et al* (1979), shown in Equation 3.4 was considered,

$$W = \frac{c}{2}(e^{Q} - 1) \tag{3.4}$$

$$Q = b_1(C_{\theta\theta} - 1)^2 + b_2(C_{zz} - 1)^2 + 2b_4(C_{\theta\theta} - 1)(C_{zz} - 1)$$

where W is strain-energy, $C_{\theta\theta}$ and C_{zz} are components of the Lagrangian stretch tensor $\mathbf{C}$ $(= \mathbf{F}^T\mathbf{F})$, and c and b_i are constants.

This model is expressed as a strain-energy function, from which stresses may be derived. Cauchy stress is defined in terms of strain energy as $\mathbf{T} = \frac{2}{J}\mathbf{F}\frac{\partial W}{\partial \mathbf{C}}\mathbf{F}^T$, where $J = \det \mathbf{F}$. As the measure of stress utilized in this study is the First Piola-Kirchhoff stress, it is given as $\mathbf{P} = 2\mathbf{F}\frac{\partial W}{\partial \mathbf{C}}$ with $\frac{\partial W}{\partial \mathbf{C}} = \left[\frac{1}{2}\frac{\partial W}{\partial \mathbf{C}} + (\frac{\partial W}{\partial \mathbf{C}})^T\right]$ to ensure symmetry in that term. Applying the above relations to the given deformation produces the following expressions for stresses in the longitudinal and circumferential directions.

$$\hat{P}_{zz} = 2\lambda_z c(b_2(\lambda_z^2 - 1) + b_4(\lambda_\theta^2 - 1))e^{Q} \tag{3.5}$$

$$\hat{P}_{\theta\theta} = 2\lambda_\theta c(b_1(\lambda_\theta^2 - 1) + b_4(\lambda_z^2 - 1))e^{Q} \tag{3.6}$$

where $Q = b_1(\lambda_\theta^2 - 1)^2 + b_2(\lambda_z^2 - 1)^2 + 2b_4(\lambda_\theta^2 - 1)(\lambda_z^2 - 1)$.

Note that no Lagrange multiplier was used to enforce incompressibility in the model directly. Instead, neglecting the stress in the radial direction indirectly requires incompressibility for this case. While the validity of the incompressibility assumption is questionable for blood vessels at large deformations, the model is consistent with the technique used to determine the measured stresses.

In order to find the best-fitting parameters for a chosen model, the composite stress function approach described by Klisch and Lotz (1999) was utilized. For the present case, the composite function is given by Equation 3.7,

$$n_1 P_{zz} + n_2 P_{\theta\theta} = n_1 \hat{P}_{zz}(\lambda_\theta, \lambda_z, c, b_i) + n_2 \hat{P}_{\theta\theta}(\lambda_\theta, \lambda_z, c, b_i) \tag{3.7}$$

where P_{zz} and $P_{\theta\theta}$ are the stresses determined from measured load and pressure and $\hat{P}_{zz}$ and $\hat{P}_{\theta\theta}$ are the calculated results of Equations 3.5 and 3.6. The constants n_1 and n_2 were set to either one or zero and were never equal to each other so that each calculated stress was compared to its corresponding measured value. The best fit of the coefficients c and b_i was achieved using the Levenberg–Marquardt algorithm (Igor Pro, Wavemetrics). Only data that satisfied the requirements of pseudoelasticity were considered. Thus, data from portions of tests where any unloading in either direction occurred were not applied to the process. Once values for coefficients were determined, data generated using the models were compared against the measured results to evaluate the quality of fit. It is important to note that this process is not intended to produce a model that can predict a wide range of data, which would best be done using an independent set of data, but rather to merely evaluate the ability of the model to fit the current data.

4 Results and Discussion

This chapter presents and discusses the results of longitudinal stretch and inflation tests on human cortical arteries and veins. Some general material observations are given first, followed by a discussion of the axial stretch results. Stretch-stretch curves and statistical analysis findings for these tests are given, and the influence of certain variables is discussed and compared to the work of other investigators. Inflation data is subsequently discussed, followed by a report of attempts to fit the measured vessel behavior with mathematical forms.

4.1 MATERIAL OBSERVATIONS

Cortical blood vessel preparation and testing revealed some interesting characteristics of these tissues. The vessels have very thin walls, leading to their relative transparence. While it is usually not difficult to find segments of vessels without major branches, numerous smaller offshoots leave each specimen at multiple points along its length, usually with not more than 2-3 mm between them. These smaller vessels dive into the brain parenchyma and are difficult to see without a microscope. For the specimens considered, veins were more likely to have a relatively long section without minor branches than were arteries. Since the cortical blood vessels lie within the subarachnoid space, each resected specimen is usually accompanied by residual arachnoid and/or pia mater, in addition to brain. With the arachnoid fibers wrapped around the specimen and its branches, in addition to the smaller branches piercing the pia, removal of this extra tissue from the specimen can be very difficult but was done.

Cortical arteries and veins are somewhat easily differentiated from each other under a microscope by their general resilience. The arteries tend to retain their cylindrical form,

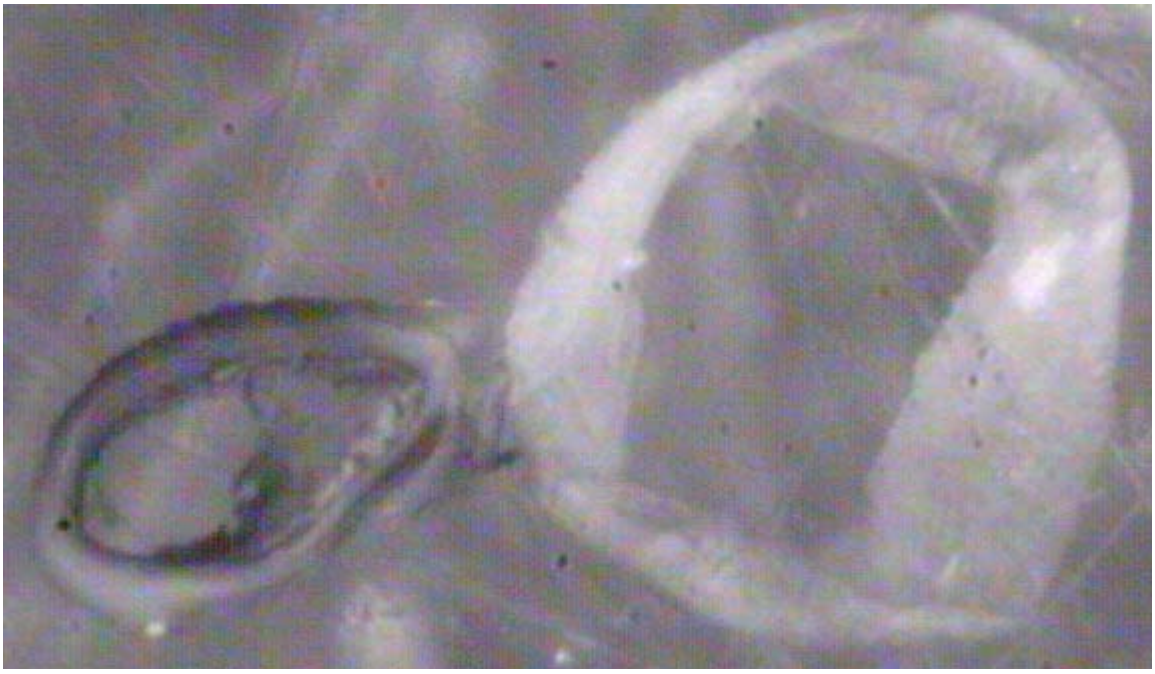

Figure 4.1 Cross-sections of an artery (smaller vessel) and a vein

whereas the veins typically collapse and wrinkle. These characteristics are also apparent when a cross-section is cut and laid flat, with differences shown in Fig. 4.1, where the small vessel is an artery and the larger one is a vein. As illustrated, the arterial section retains its shape, while it is difficult to get the flaccid vein walls to remain perpendicular to the surface. Because of the arteries' relative resilience, extra tissue is more easily dissected away from them than the veins, where it is difficult to discriminate between vein wall and surrounding membranous tissue. This behavior is believed to be a result of the lack of smooth muscle in the walls of the veins. Except for cases where plaque was visible in some large artery walls, no particular visual differences were observed between vessels obtained through surgery and those harvested in autopsy.

A summary of the dimensional measurements made on resected cortical vessels is given in Table 4.1. Means for *in vivo* stretch, cross-sectional area, approximate outer

diameter (only approximate due to non-circular sections), and wall thickness are reported, along with two calculated ratios, those of cross-sectional area to wall thickness and outer diameter to wall thickness. Cortical specimens obtained from both surgery and autopsy are included. As the table indicates, *in vivo* stretch values for arteries and veins were virtually identical. On average, arteries had smaller cross-sectional areas and outer diameters than veins, while the two vessel types displayed similar wall thickness values. No significant dimensional differences were visible between vessels obtained from surgery and the few harvested through autopsy. A detailed spreadsheet listing the properties of each individual specimen is included in Appendix C.

Table 4.1 Number, Mean, and Standard Deviation for Pre-Test Geometrical Measurements on Cortical Arteries and Veins Harvested in Surgery and Autopsy (λ_{iv} – *in vivo* stretch; CsA – cross-sectional area; ~OD – approx. outer diameter; t – wall thickness)

	Arteries				Veins			
	λ_{iv}	CsA (mm^2)	~OD (mm)	t (mm)	λ_{iv}	CsA (mm^2)	~OD (mm)	t (mm)
Num	27	42	41	42	21	23	24	22
Mean	1.31	0.20	0.60	0.10	1.31	0.36	0.82	0.11
Stdev	0.25	0.10	0.21	0.03	0.15	0.26	0.36	0.04

The quality of the collected histology sections was questionable, so those results are not discussed here. It is considered sufficient to say that sections from arteries and veins differed significantly, as expected. Two sample images from this study, one of an artery and one of a vein, are included in Appendix A.

While residual stresses were not considered in the calculation of stress and stretch due to the application of the thin wall assumption, the small amount of data collected on opening angles of the studied specimens is included in Appendix D as a matter of general interest.

4.2 MECHANICAL TESTING — LONGITUDINAL STRETCH

4.2.1 General Observations

A sequence of video images for a typical quasi-static test of an artery with an outer diameter of 0.6 mm and a reference length of 7.8 mm is shown in Fig. 4.2(a). Frames are presented at intervals of 0.4 s. It is evident from the video that the specimen stretched

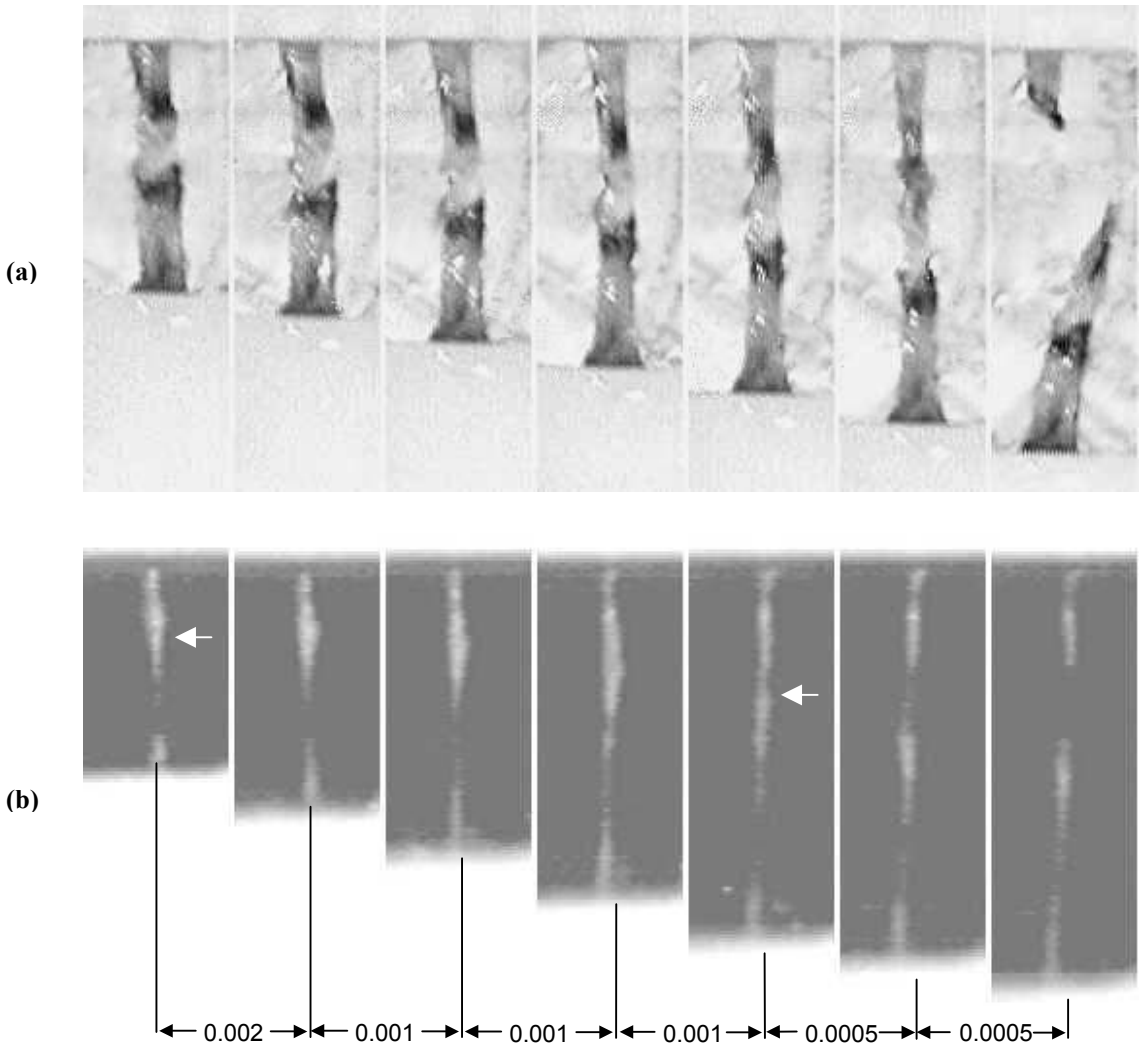

Figure 4.2 Quasi-static (a) and dynamic image sequences for an artery and a vein, respectively. Frame spacing is 0.4 seconds for (a) and is given in seconds for (b). Arrows in two frames of (b) identify a segment of the vein where some excess tissue was not dissected away and where failure ultimately occurred.

uniformly (by comparing displacements of stained regions) and exhibited minimal necking until just prior to failure, which in this case occurred in midsection.

Similarly, a collection of high speed video pictures for a dynamic test of a typical vein with a diameter of 0.35 mm and a unstretched length of 9.4 mm is shown in Fig. 4.2(b). The time interval between images is indicated in the figure, consisting of multiples of 0.5 ms. In two frames, a superimposed white arrow identifies a segment of the vein where some superficial tissue was not dissected away prior to testing, thus giving the impression of a larger diameter relative to the rest of the vessel. While the dark, lower portion of the vessel appears smaller in diameter (due to applied stain), the sequence of images reveals that failure occurred at the same point identified by the arrows, with the vessel remaining intact in the dark region. As was true with the quasi-static test shown in part (a) of the figure, deformation is quite uniform and failure occurred in midsection.

The load-displacement behavior of each of these specimens is shown in Fig. 4.3, demonstrating the presence of an exponential toe region. The arterial data then transitions into linear behavior up to the point of failure. As a result, the yield and ultimate points are considered to be the same for this specimen. Different from the artery case, the extent of the toe region for the vein is not particularly obvious, but after a short rise in load, the slope of the curve begins to decrease, indicating the location of the yield point. The load then continues to rise until ultimate failure is achieved. Of particular note with the vein trace is that the load does not seem to rise until well after 11 mm, yet the chosen reference length for this case, as indicated above, was 9.4 mm. This is believed to be due to noise generated through both impact wave propagation and dynamic characteristics of the load cell.

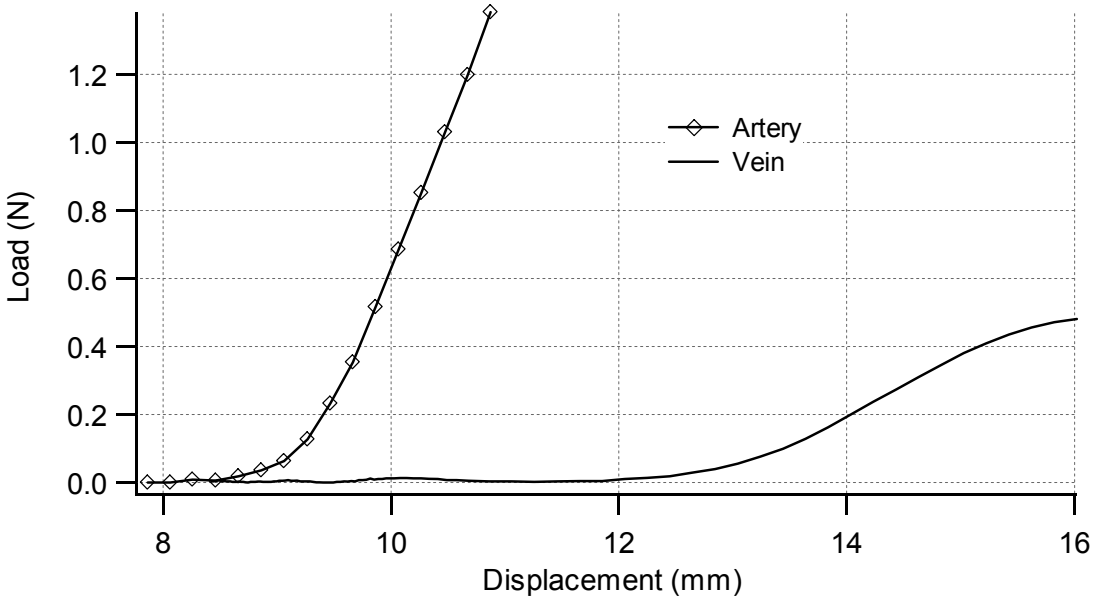

Figure 4.3 Load-displacement data for artery and vein depicted in Fig. 4.2

Like the artery and vein shown in this case, results from tests on all arteries and veins displayed the classic concave-upward behavior expected of soft tissue stress-strain relations. Different from the artery considered above, most also demonstrated separate yield and ultimate points. In nearly all cases, stretch was uniform along the length of the vessel up to the point of yield, after which most additional deformation was limited to the region of failure. While in the two presented examples failure occurred in midsection, just under two-thirds of the specimens failed at the clamp. In general, specimens appeared to be reasonably homogeneous and did not exhibit any large branch points. Both of these factors would be expected to influence the behavior of the vessels under load in an unknown manner. Large variation in the data are observed, as is expected for presumably similar biological materials.

4.2.2 Stress-Stretch Curves

4.2.2.1 Vessels from Surgery

Figures 4.4 and 4.5 present quasi-static and dynamic stress-stretch results, respectively, of longitudinal tests for cortical veins and arteries obtained through surgery. As is the case throughout this dissertation, the stress is given as the First Piola-Kirchhoff stress. The quasi-static data reveal the previously unknown fact that the cortical arteries fail at approximately twice the stress level of the cortical veins and at about half the stretch. The dynamic test results appear to agree with the quasi-static ones on this matter. This suggests that if longitudinal stretching of the vessels is assumed to be the mechanism of failure in head impact, bleeding associated with contusions in the temporal lobes is more likely due to rupture of arteries rather than veins. Before making such a statement, however, it is important to compare the behavior of the vessels relative to the *in vivo* stretch. For example, if the veins were found to shrink more than the arteries upon excision, they would experience considerably more stretch under *in vivo* conditions and may have less stretch remaining before failure than the arteries. As Table 4.1 shows, however, both types of vessel shrink, on average, to 75% ($1 / \lambda_{iv}$) of their original length upon resection. Thus, the comparisons of Figs. 4.4 and 4.5 are considered sufficient for this argument.

While the quasi-static data for arteries and veins are, for the most part, well grouped, one artery, in particular, withstood a unusually high amount of stretch in comparison to the other arteries. A review of the data revealed that this specimen was preconditioned well beyond *in vivo* stretch levels, so it is likely that the pre-stretch influenced its behavior. Beyond high stretch values, however, independent consideration of the vessel's

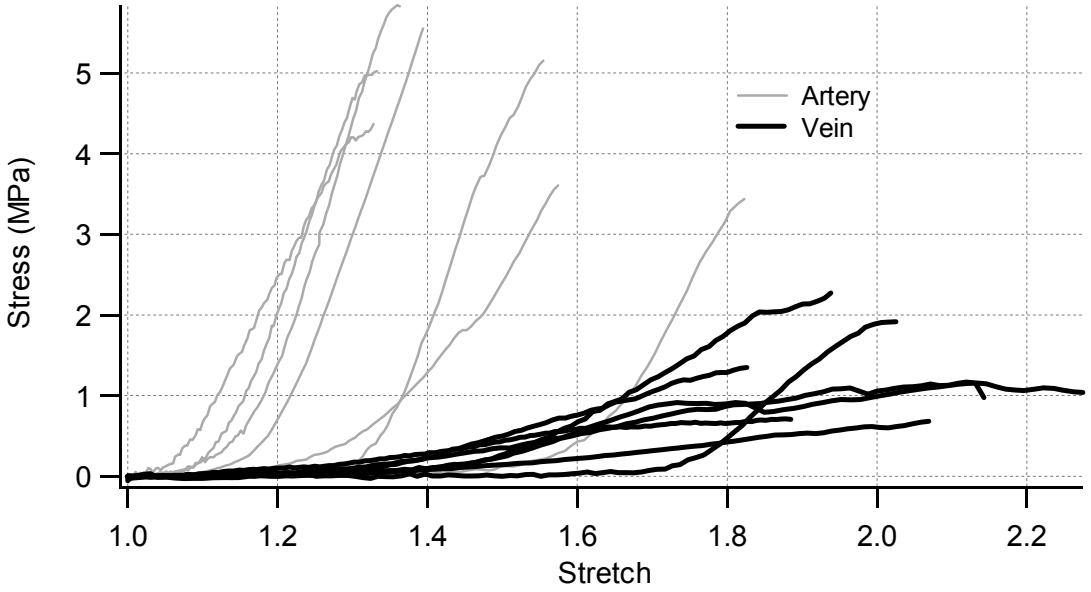

Figure 4.4 Quasi-static stress-stretch results for cortical arteries and veins resected in surgery

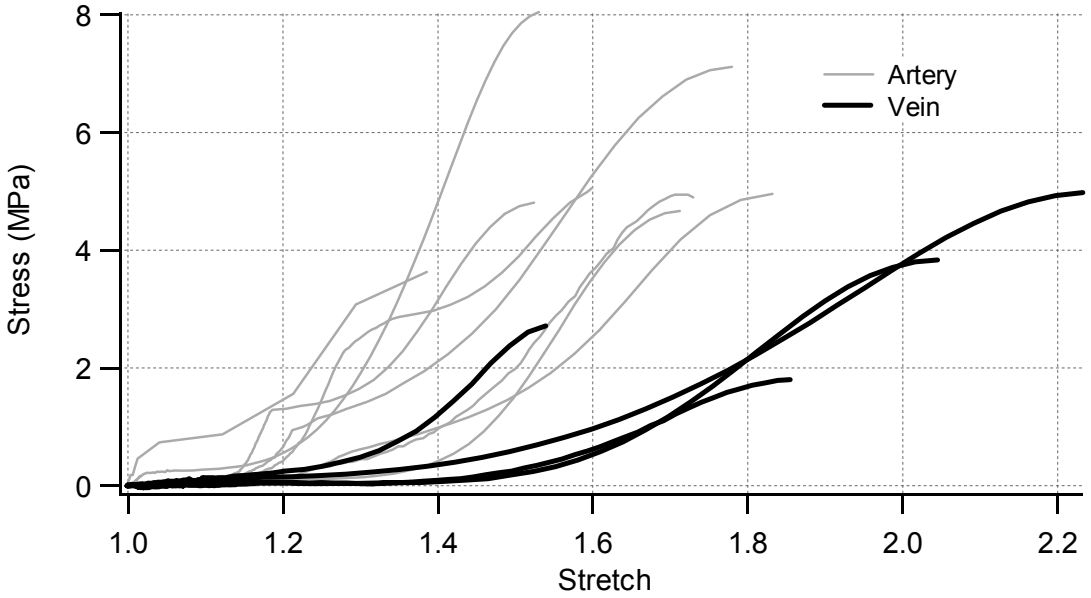

Figure 4.5 Dynamic stress-stretch results for cortical arteries and veins resected in surgery

behavior reveals nothing to indicate that it was damaged and should thus be eliminated from consideration. Similar to this artery, one vein specimen stands out from the others with a remarkably steep stress-stretch curve; it was also preconditioned beyond *in vivo* levels. Extent of pre-stretch thus appears to have a significant impact on vessel mechanical properties and will be further discussed.

Figures 4.6 and 4.7 present a rearrangement of the data to allow direct comparison of quasi-static and dynamic results for arteries and veins, respectively. These figures suggest that increasing the rate of stretch is influential in both arteries and veins, tending to increase the maximum stress obtained. It also appears, for arteries, that ultimate stretch may have increased in dynamic testing, an opposite result than what would be expected. It is unknown why one dynamic vein trace in Fig. 4.7 displays such a small ultimate stretch. The significance of testing rate is difficult to determine from the plots alone, but variation between the different rate tests seems to be on the same order as the biological

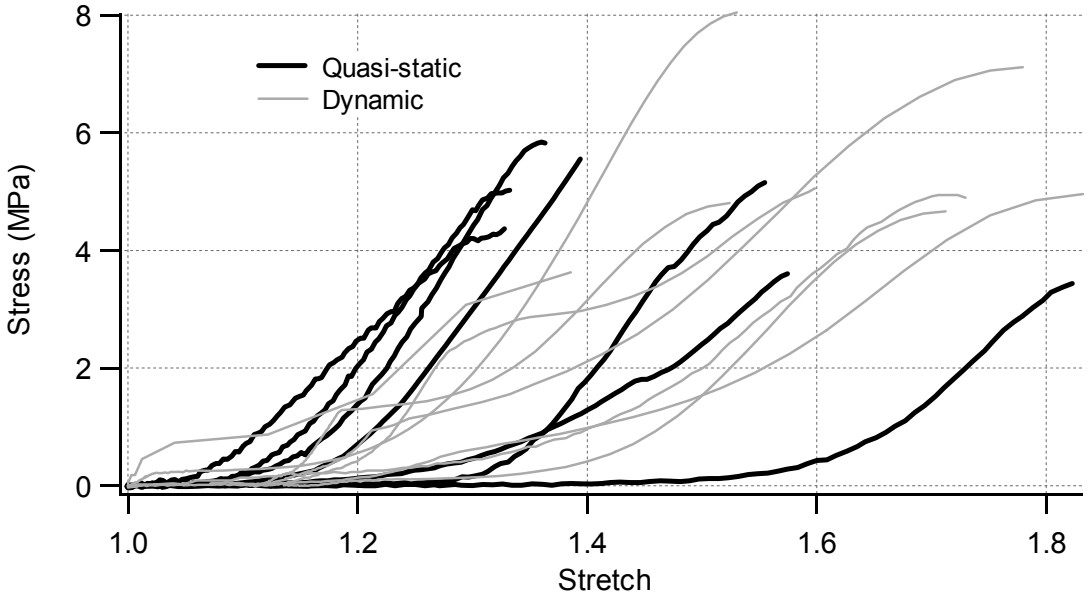

Figure 4.6 Quasi-static and dynamic stress-stretch results for cortical arteries from surgery

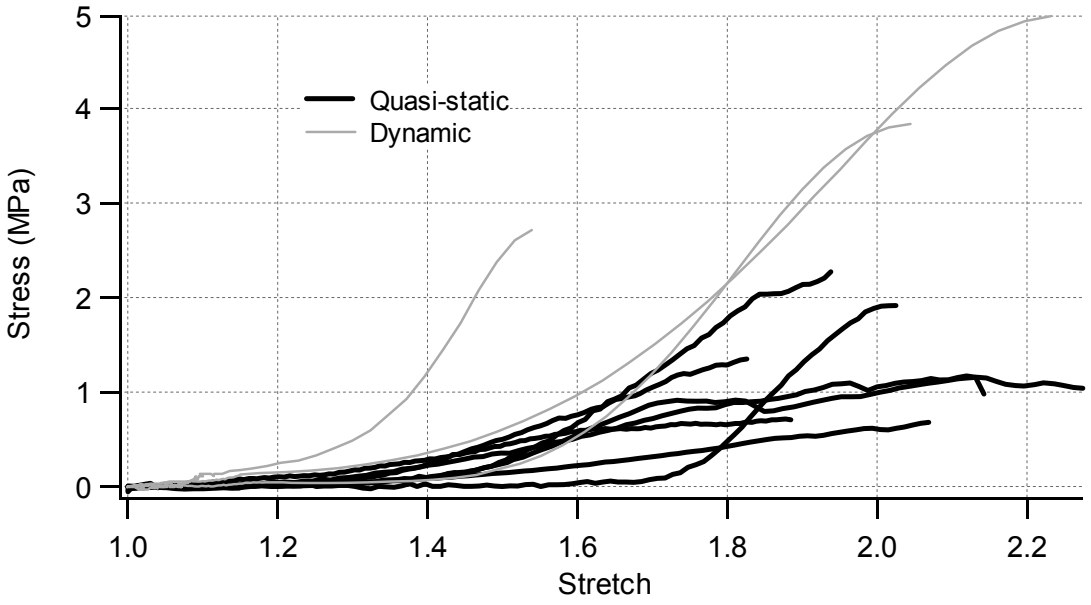

Figure 4.7 Quasi-static and dynamic stress-stretch results for cortical veins from surgery

scatter. Strain rates ranged from 211-476 s^{-1} and from 196-524 s^{-1} for dynamic tests on arteries and veins, respectively, while quasi-static test rates, in the same order, ranged from 0.01-0.26 s^{-1} and from 0.04-0.20 s^{-1}, a difference of three orders of magnitude between the two types of test.

4.2.2.2 Vessels from Autopsy

As was shown for surgical specimens, Figs. 4.8 and 4.9 provide comparisons of cortical arteries and veins tested quasi-statically and dynamically, respectively, while Figs. 4.10 and 4.11 compare results from tests at different rates on arteries and veins, respectively. Similar to specimens obtained through surgery, cortical vessels resected in autopsy also exhibit clear differences between behavior of arteries and veins, again with the arteries failing at around half the stretch and twice the stress of the veins. As was the

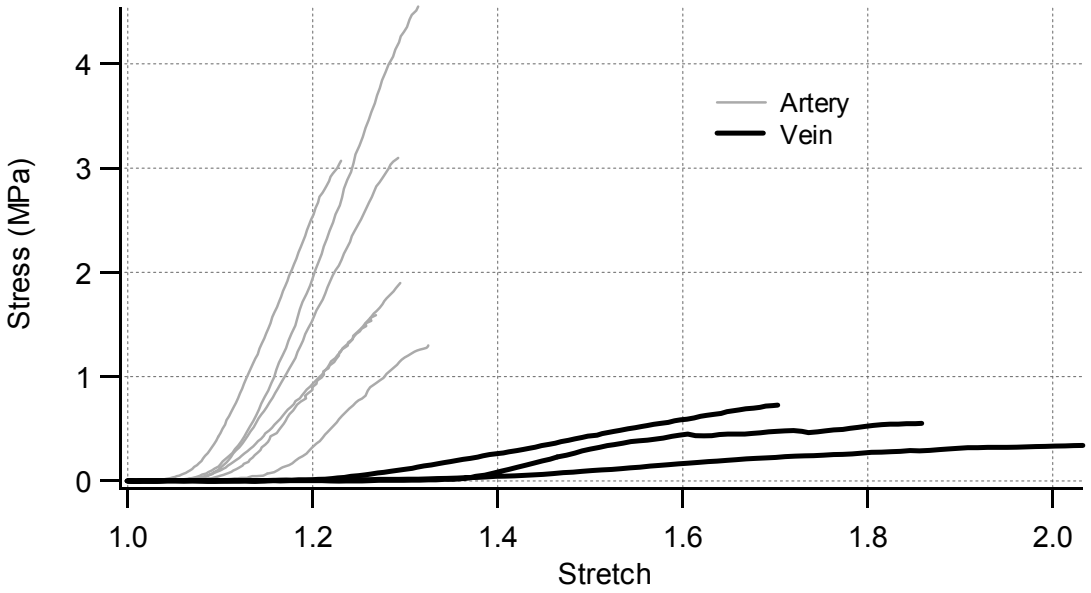

Figure 4.8 Quasi-static stress-stress results for cortical arteries and veins from autopsy

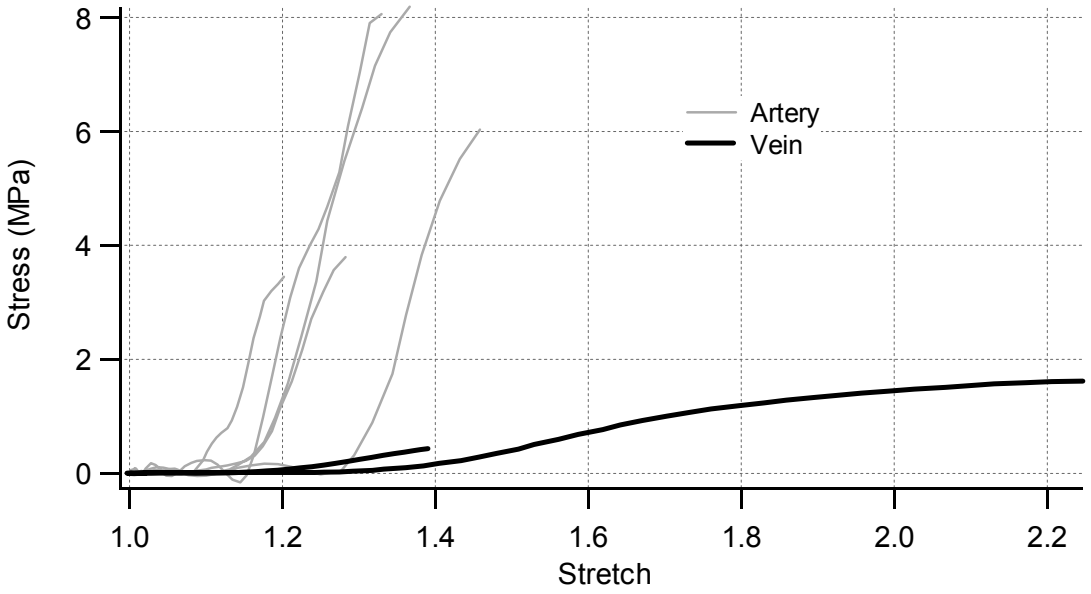

Figure 4.9 Dynamic stress-stretch results for cortical arteries and veins from autopsy

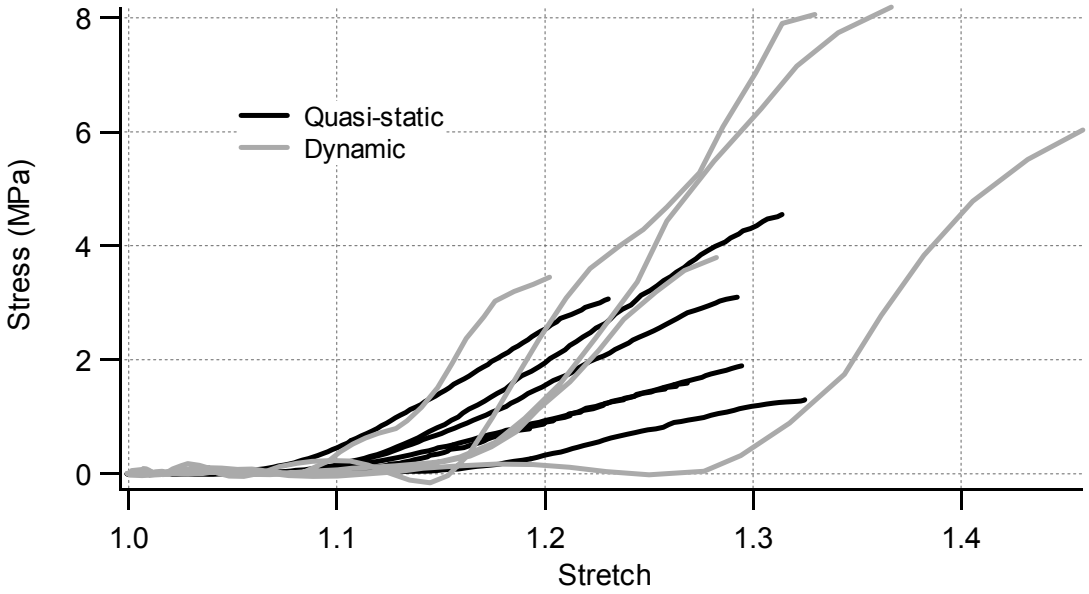

Figure 4.10 Quasi-static and dynamic stress-stretch results for arteries from autopsy

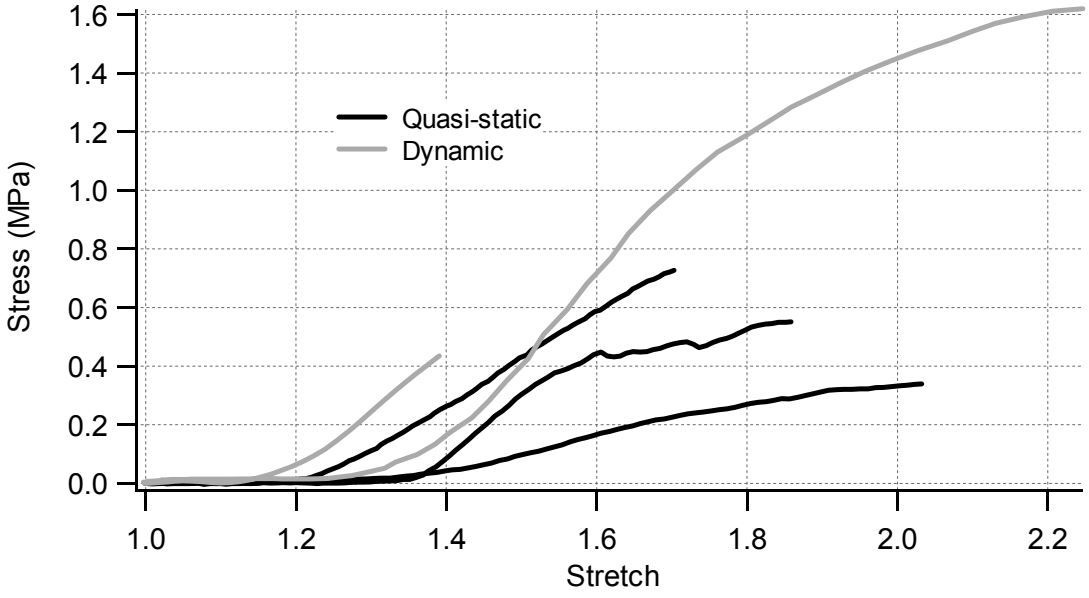

Figure 4.11 Quasi-static and dynamic stress-stretch results for veins from autopsy

case in dynamic tests on surgical vessels, failure stress appears to increase for high-rate-tested autopsy specimens in comparison to quasi-statically-tested ones. Additionally, ultimate stretch again appears to increase with rate for arteries. Dynamic and quasi-static tests on autopsy vessels were conducted at strain rates ranging from 28-138 s^{-1} and from 0.03-0.10 s^{-1}, respectively.

4.2.2.3 Comparison of Autopsy Vessels to Fresh

In order to compare the stress-stretch behavior of vessels taken in surgery to those resected during autopsy, a variety of traces from the preceding figures are combined into Figs. 4.12 and 4.13. For arteries, these comparisons seem to indicate a relative reduction in ultimate stretch for autopsy specimens, with little change in ultimate stress. The comparisons for veins, however, suggest little change in ultimate stretch but a reduction of ultimate stress in samples from autopsy.

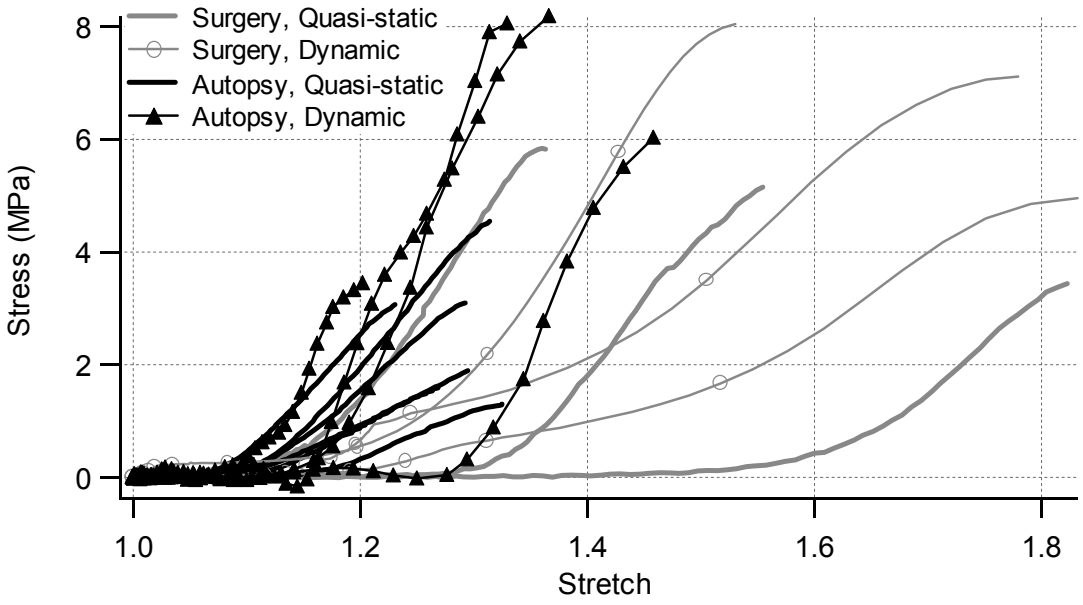

Figure 4.12 Stress-stretch behavior for cortical arteries from surgery compared to those from autopsy. Results include both quasi-static and dynamic data.

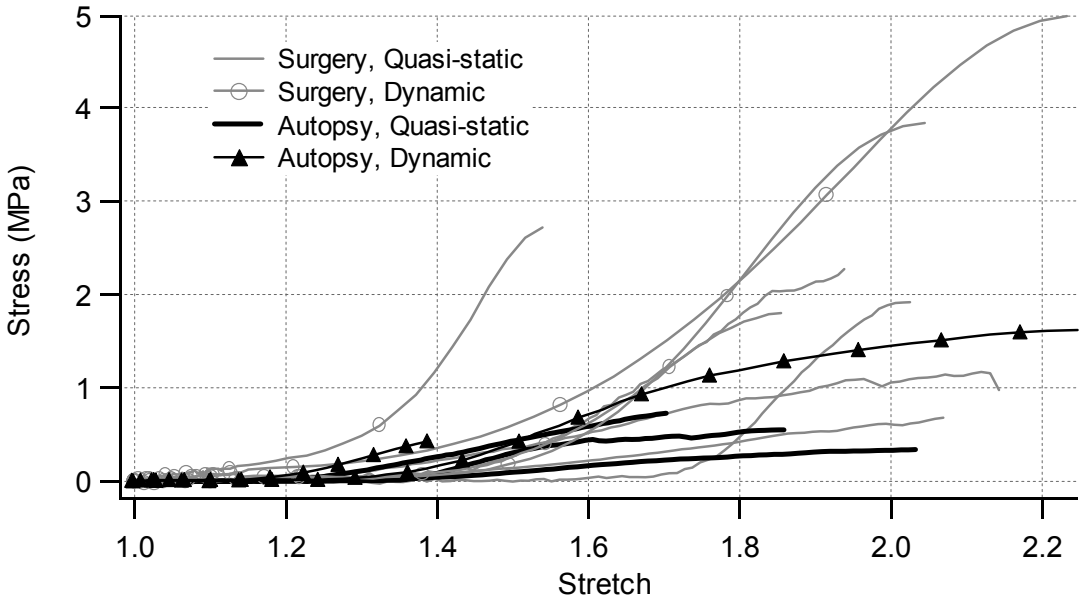

Figure 4.13 Stress-stretch behavior for cortical veins from surgery compared to those from autopsy. Results include both quasi-static and dynamic data.

4.2.3 Statistical Analysis

4.2.3.1 Mean Properties

While the presented curves allow qualitative stress-stretch comparisons for different cases, a statistical analysis of variation in the defined curve parameters provides a more thorough view of the significance of the different variables. Figure 4.14 graphically summarizes the mean values of the specified curve parameters for tests on arteries and veins, illustrating differences associated with autopsy and surgery as well as quasi-static and dynamic. A complete listing of the properties associated with each individual specimen and test is given in Appendix C. The toe-region exponential curves in Fig. 4.14(a) were generated using the mean values for the constants A and B and extend as far as λ_T, marking the average end of the toe region. Figure 4.14(b) summarizes the maximum slope Mod_Y, represented by the line segment (of arbitrary length) below the

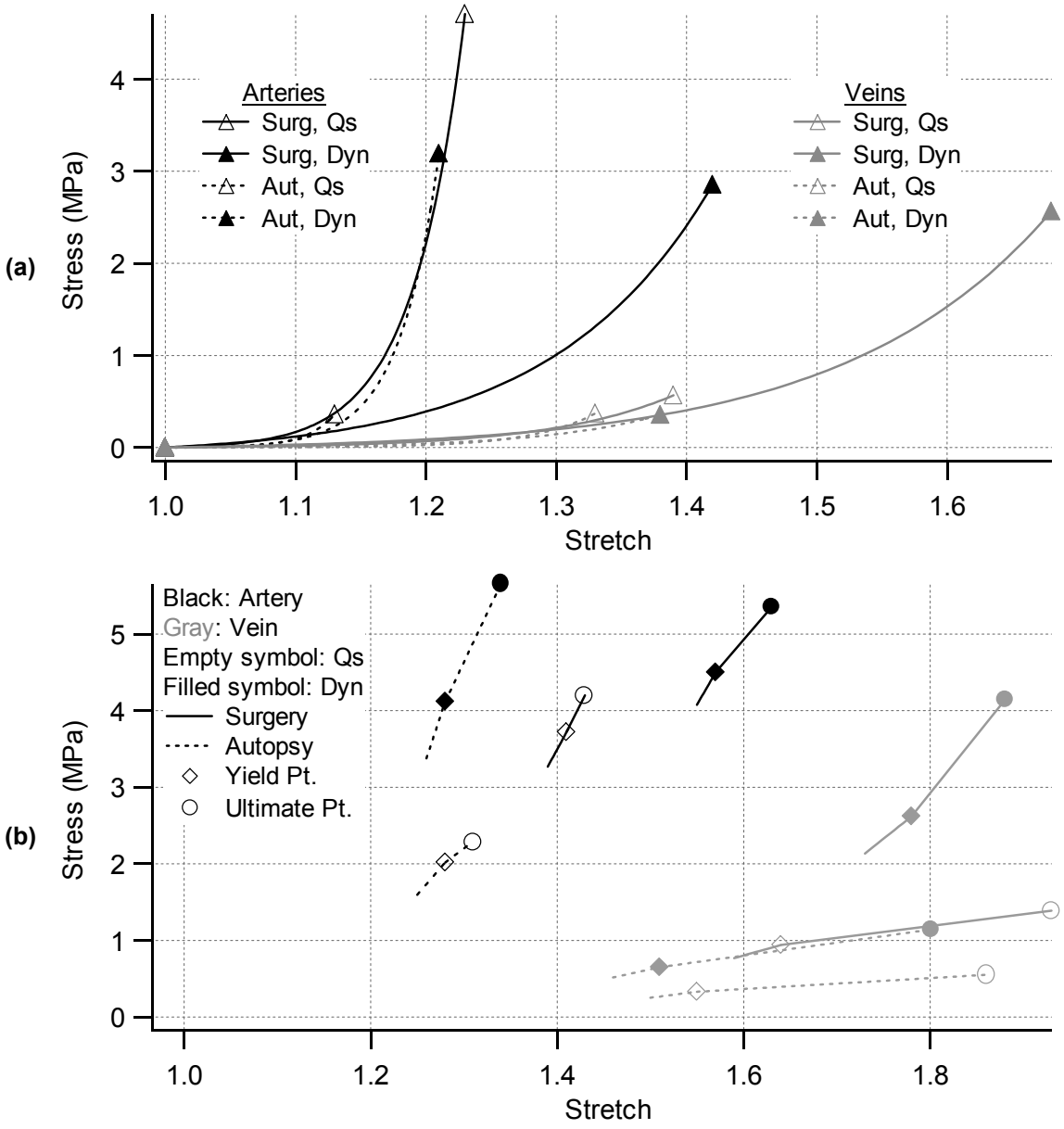

Figure 4.14 Summary of mean (a) subfailure and (b) failure values for stress-stretch tests, by vessel type and source and testing rate. In (a), curves were generated using *A* and *B* and were extended as far as the mean λ_T for the group. Note that the lines connecting the yield and ultimate points in (b) are meaningless except to clarify which points are from the same group.

diamond symbol, and the yield and ultimate points, identified by the diamond and circle, respectively. It is important to note here that the line connecting the ultimate and yield points is present only to indicate which points are related; it has no physical meaning in

terms of the curve shape. All arterial tests are represented with black color, while the vein data are gray. Solid lines indicate surgical specimens; dashed lines identify those from autopsy. Quasi-static and dynamic tests are distinguished by whether the symbol is filled or not, and the diamond and circle symbols identify the yield and ultimate points, respectively.

In Fig. 4.14(a), dynamically-tested arteries and veins from surgery both display a substantially longer average toe region than the other groups. While the vein case maintains the same basic shape as the other vein groups, the arterial one departs significantly from the typical behavior of the arteries. Although it is a bit difficult to see in this plot, the mean initial moduli of the autopsy traces are smaller than those for surgery cases, but their curves increase more quickly than the others as stretch increases. In part (b) of the figure, it is surprising to see that, in two cases, the maximum modulus is not as steep as the line connecting the yield and ultimate points. Since all parameters were not measurable for all tests, this is believed to be a result of slightly different sample populations.

Upon comparison of the two plots, it is clear that the toe-region curves in Fig. 4.14(a), if extended as far as their average toe-region stretch (as in the plot), don't match well with the failure values shown in Fig. 4.14(b). Why this is the case is not fully understood, but if the curves are cut off before they reach the mean toe-region stretch value, they produce much more reasonable estimates of average curve shapes. The plots provide a nice summary of the differences between the various groups, but it is impossible to know, without a more in-depth statistical analysis, which of the apparent differences are significant and which are not.

4.2.3.2 Multivariate Analysis

Based on initial MANOVA tests, donor age was determined to be the only independent variable, besides vessel type, vessel source, and testing rate, that seemed to warrant inclusion in further models, at least within the ranges of variation in this data set. Age was determined to have a significant interaction with testing rate, but no other interactions between the four variables were identified. This means that, for example, the differences between arteries and veins seem to be the same regardless of whether the vessels were obtained through surgery or autopsy and whether they were tested quasi-statically or dynamically. Data from these tests are included in Appendix E.1.

As a result of these initial studies, the final statistical model included vessel type, specimen source, and test method as independent variables. Since the previous tests indicated that the effect of age varied differently in quasi-static tests than in dynamic experiments, two new independent combination variables, age_dynamic and age_quasi-static, were created and used in the model with the others. Predicted percent changes in the curve parameters for alterations in the independent variables are summarized in Table 4.2. The percent changes were calculated relative to the reference values, which were predicted for an artery that was tested quasi-statically after being obtained from a thirty-year-old patient in surgery. For the case of the reference, the numbers represent parameter values and not percentages. The chart, then, is read as the following example illustrates. For a case equivalent to the reference, except that a vein was tested instead of a artery, a 12.7 % increase in the reference value of 1.26 for λ_T is predicted, giving a value of 1.42. Since initial MANOVA tests demonstrated no interactions between the independent variables except for that accounted for between age and testing rate, multiple

variable changes from the reference may simply be summed. Changes that were shown to be statistically significant are given in bold. A complete listing of predicted absolute changes in the curve parameters, along with 95% confidence intervals and p-values, is included in Appendix E.2.

Table 4.2 Predicted percent changes, relative to the reference, in curve parameters for changes in each independent variable from the reference. Reference values (italicized) correspond to an artery obtained from a 30-year-old patient in surgery and tested quasi-statically. Changes that were shown to be statistically significant are given in bold.

	λ_T	A	B (MPa)	Mod_Y (MPa)	λ_Y	σ_Y (MPa)	λ_U	σ_U (MPa)
Reference Values (Art, Surg, QS, 30)	*1.26*	*22.41*	*0.36*	*21.74*	*1.44*	*3.67*	*1.49*	*4.41*
Vein	**12.7**	**-68.5**	**-55.6**	**-85.8**	**18.1**	**-67.8**	**32.2**	**-64.6**
Autopsy	**-9.5**	**59.8**	**-91.7**	**-41.5**	-9.7	**-61.9**	-5.4	**-52.8**
Dynamic	**34.1**	-25.9	22.2	-21.5	**27.1**	**64.6**	**26.8**	61.5
10 Year Age Increase (Dynamic Tests)	**-5.6**	7.3	8.3	**24.8**	**-6.3**	4.9	**-7.4**	3.2
10 Year Age Increase (Quasi-static Tests)	0.0	10.8	2.8	7.8	-0.0	**10.1**	-2.0	5.2

Table 4.2 can be used to determine the predicted values for any combination and variation of the independent variables. It is important to note, however, that because the data set does not correspond well to all possible combinations, some cases result in unreasonable predictions. For example, if one wishes to predict the yield modulus, Mod_Y, of a quasi-statically tested vein that was obtained from a thirty-year-old in autopsy, Table 4.2 recommends a 127% total reduction in the modulus of the reference. This obviously yields a negative, physically unrealistic value for this property. A review of the data set reveals that this combination of variables is not well represented, since only three veins with an average donor age of 52 were obtained from autopsy and tested quasi-statically.

Despite the poor performance of the model at this location, predictions from better supported areas produce believable results.

An extensive listing of predicted parameter values for various combinations and changes in the independent variables is provided in Appendix E.3. Use of the predicted values to construct an expected curve, however, reveals the same problem discussed in the previous section on mean values, namely, if the toe-region curve is extended as far as the average toe length, it does not match the failure predictions. As with the mean values, a reasonable prediction may be obtained by restricting the length of the toe exponential.

The predictions of Table 4.2 generally agree with the graphical mean value summaries of Fig. 4.14, but the table clarifies which of the changes are significant. The following sections discuss the changes predicted for alterations in the various independent variables.

4.2.4 Discussion of Independent Variable Significance

4.2.4.1 Vessel Type

The numbers in Table 4.2 reveal that the independent variables are listed in order of general decreasing influence, at least in terms of how broadly significant they are. With greater influence than any other variable, variation of vessel type (artery or vein) changes all eight parameters significantly. According to the table, an arterial specimen is expected, in comparison to a vein, to have a shorter toe region, with higher values for both A and B, indicating more non-linearity in the toe region and a higher slope at $\lambda = 1.0$. It is also expected to have a steeper yield modulus. Additionally, it will most likely also demonstrate lower yield and ultimate stretches but higher stress values at these

locations. These differences are no surprise since they are readily visible in the stress-stretch plots.

While there are no other comparisons of cerebral arteries and veins in the literature, Fig. 4.15 shows selected traces from the current study in the context of reported quasi-static tests on a variety of other vessels (including data from Yamada, 1970; Chalupnik *et al*, 1971; Lee and Haut, 1989; Steiger *et al*, 1989). The plot demonstrates similarity between the cortical and large cerebral arterial data (MCA, MCA II). When compared to other blood vessels, the cerebral arteries are significantly stiffer and withstand much less stretch before failure. Busby and Burton (1965) have similarly reported a higher longitudinal stiffness for cranial arteries than for extracranial ones. The cortical veins

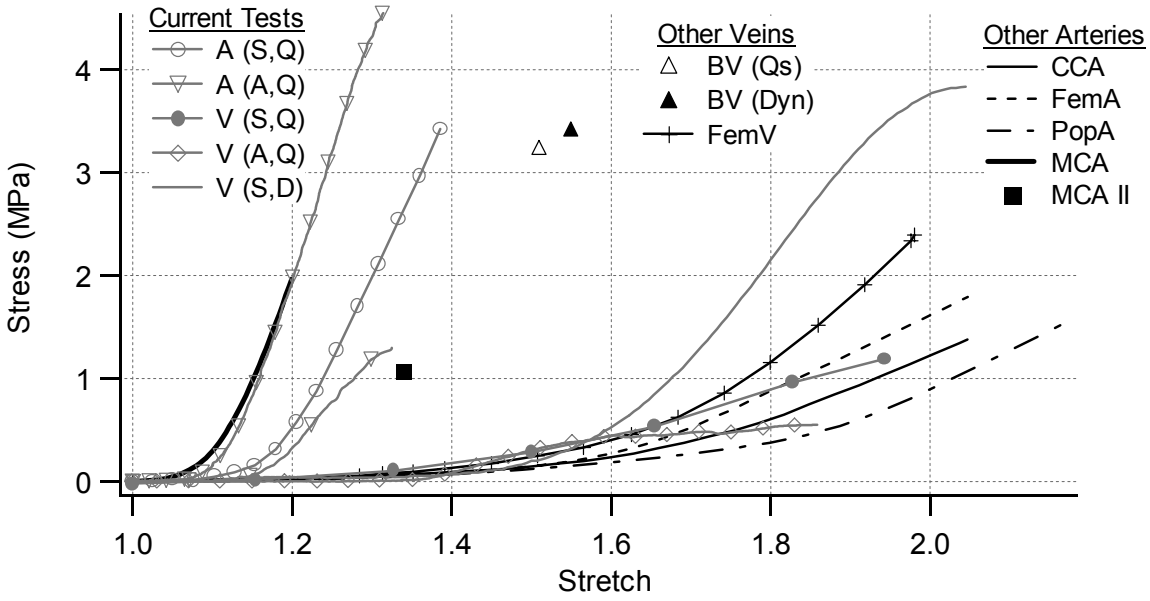

Figure 4.15 Comparison of stress-stretch behaviors from the current experiments with those reported in the literature for a variety of blood vessels. Current tests are identified as arteries or veins with an A or V (S-surgery, A-autopsy; Q-quasi-static, D-dynamic). BV-bridging vein failure points (Lee and Haut) for quasi-static and dynamic tests. MCA-subfailure major cerebral artery data (Chalupnik *et al*). MCA II-failure data for major cerebral arteries (Steiger *et al*). CCA, FemV, FemA, PopA-common carotid artery, femoral vein, femoral artery, popliteal artery (Yamada).

display behavior similar to most other non-cerebral arteries and veins, which, in general, don't appear to indicate any particular differences between the two types of vessel.

4.2.4.2 Specimen Source

While not as widely significant as vessel type, specimen source also has a significant influence on a number of the curve parameters, according to Table 4.2. Surgical vessels are expected to produce longer toe regions than those from autopsy, with lower values for *A* but higher ones for *B*. They are also anticipated to demonstrate higher yield moduli and yield and ultimate stresses. While the variable is near significant levels for the yield stretch, neither the yield nor the ultimate stretch is predictably affected.

No other published study compares the properties of blood vessels from surgery and autopsy. The effect of specimen source is not visible in the traces of Fig. 4.15, where each of the non-cortical vessels was obtained from autopsy, but its influence is likely hidden there by variation associated with size and structure.

It is particularly interesting to consider the stretch disparity between the bridging vein failure data and that associated with the presented dynamic cortical vein trace. The bridging veins were obtained from cadavers while the vein from the current study was taken in surgery, but based on the above results, the specimen source variable did not significantly influence yield or ultimate stretch values. Since the bridging veins are really just cortical veins that bridge the gap between the brain and skull, they might be expected to have the same general structure and behavior. It is possible, however, that their dissimilar configurations and resulting *in vivo* physiological loading conditions produce structural differences. It is also important to note, however, that the specimens tested by Lee and Haut were obtained by excision from frozen cadaver heads and, further, were

stored overnight in saline solution after thawing. A recent study by Brossollet and Vito (1997) shows a significant increase in stiffness resulting from this type of tissue storage, which may contribute to the discrepancies in the results noted above.

4.2.4.3 Testing Rate

The influence of testing rate, with dynamic cases compared to quasi-static ones, is also illustrated in the table. As shown, the toe region is anticipated to be longer for dynamic tests, and the yield and ultimate stretches and yield stress are all expected to increase for dynamic tests. Ultimate stress is also likely to increase but its p-value was slightly over the level required for the change to be considered significant.

It should be noted here that, in most cases, the dynamic strain rates associated with autopsy vessels were significantly lower than those for vessels from surgery (28-138 s^{-1} compared to 196-524s^{-1}). As a result, there was some concern that this difference might affect observations regarding the influence of rate. Statistical tests were thus conducted to check for interactions between effects associated with the vessel source and testing rate variables, as it might be expected, for example, that dynamic tests on specimens from autopsy would produce different results than dynamic tests on surgical vessels, due to the differences in rate. Results of the tests demonstrated no significant interaction and may be seen in the form of confidence ellipse plots included in Appendix E.4. While it is possible that measured values would be different in autopsy vessels if they were tested at higher rates and that the shift in test rates was just right to produce results similar to the surgical vessels, this seems unlikely. Nevertheless, it remains a possibility, and this inconsistency is considered to be a weakness of the study that must be cleared up by further testing.

4.2.4.3.1 Dynamic Test Modeling

While statistical analysis of the data provides expected differences for vessels tested at different rates, a graphical illustration of an artery's stress-stretch response during preconditioning (a quasi-static process) and during a dynamic ramp, as shown in Fig. 4.16, provides some insight into why the differences may exist and how they might be related. First is the fact that the responses for the preconditioning cycles and the dynamic ramp do not correspond as expected. Rather, the dynamic trace doesn't begin to rise significantly until a much higher stretch is reached. Since this inconsistency was present in a number of dynamic tests but in no quasi-static ones, it was concluded that something was corrupting the data from the dynamic tests. Additionally, with high-rate tests also demonstrating more rounded features, in general, it seemed likely that some effect was operative at other regions of the curve as well.

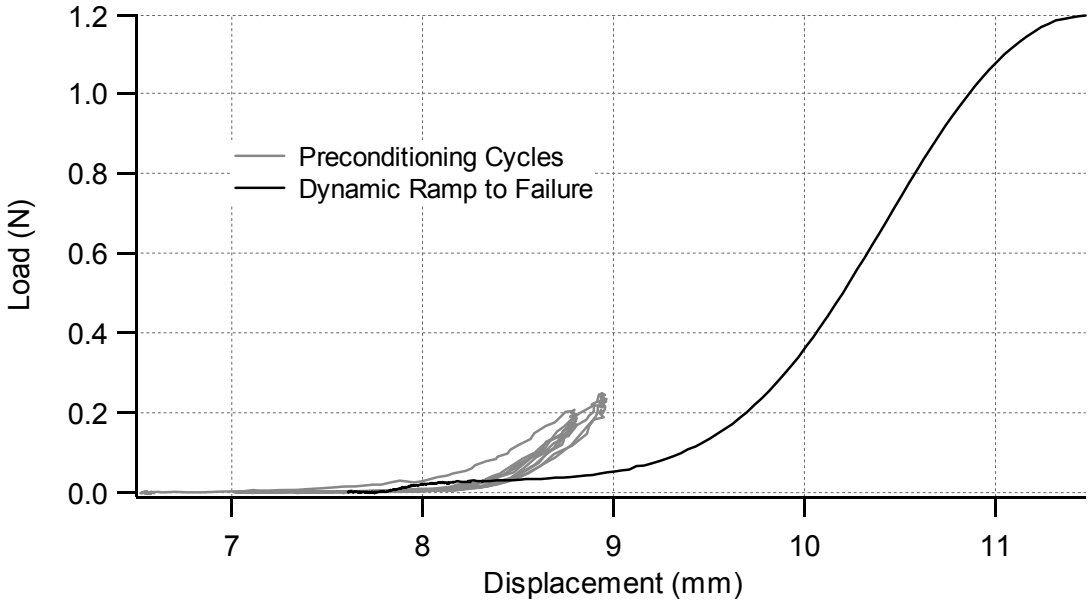

Figure 4.16 Load-displacement response of a selected artery during preconditioning and dynamic testing to failure

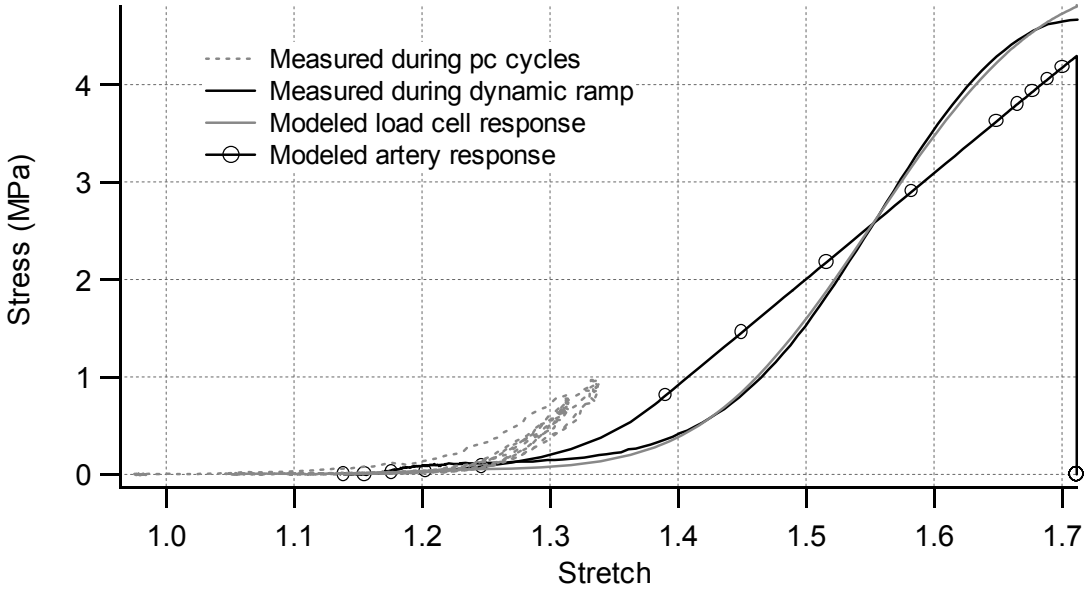

Figure 4.17 Comparison of the stress-stretch response of an artery during preconditioning and its measured and modeled behaviors for dynamic testing

Figure 4.17 shows the results of the load cell-grip-vessel model described in Chapter 3, for the artery from Fig. 4.16. The plot shows the stress calculated from the measured load during the test, along with the stresses calculated from the model-predicted loads in both the load cell and the vessel. While the model-produced load does not exactly match the measured load (likely due both to vibrations associated with impact wave propagation and an imperfect modeling process), there is remarkably good agreement between the two, confirming the suitability of the model. As Fig. 4.17 shows, the model predicts significantly different load-displacement behavior for the load cell and the vessel, with the vessel stress beginning to rise much closer to where the preconditioning trace began to increase, decreasing the length of the toe region. Additionally, the ultimate stress has been reduced so that the trace is more comparable to typical quasi-static behavior.

In the presented figure, the most poorly matched portions of the curve are at very small loads and in the ultimate region. Lack of matching at small loads is likely due to impact wave or testing machine vibrations. As overshoot of the model trace in the ultimate region suggests, the latter discrepancy is probably a result of neglecting the damping characteristics of the load cell in the model. Had the influence of damping been included, however, it appears that the reduction in ultimate stress would be even greater. During the curve-matching process, it was discovered that the quadratic portion of the curve was seldom useful in achieving an adequate fit, probably due to the neglect of damping. Since the yield values of the new curve were dependent upon its use, their identification was somewhat arbitrary. As a result, yield values were not reported for the modeled cases.

For other dynamic cases, some curves matched as well as the presented case while others did not. Many of the model results suggested significant changes in the stress-stretch behavior but others suggested no major changes. General trends for adjustment, however, were similar to those demonstrated by the example case. Plots showing model results for some of the other considered cases are included in Appendix B.3.

Adjusted curve parameters from each of the model-produced traces were substituted into the original data set, and the statistical model was run a second time to evaluate the effect of the changes. Results indicated a marked decrease in the general significance of the test rate variable, with no parameter predictably changing with test rate except for the length of the toe region. The magnitude of the expected change of this parameter was reduced by approximately half in comparison to the original model. Numerical results for the second statistical model run are outlined in Appendix E.5. This study of the dynamic

test results points toward a lack of rate dependence in the cerebral blood vessels, but it is important to note that further tests are expected to shed more and more light on the subject. It also suggests that data from previous studies in which rate dependence was reported may have been corrupted by load cell dynamics.

4.2.4.4 Donor Age

Table 4.2 shows donor age to be the least significant of the considered independent variables, although it was, interestingly, more significant in dynamic tests than in quasi-static ones. For dynamic tests, increases in age were found to shorten the toe region, increase the yield modulus, and decrease the yield and ultimate stretches. Interestingly, for quasi-static cases, the only significant effect was to increase the yield stress. Why age would be more influential in dynamic tests than quasi-static ones is unknown. More data is needed to confirm this finding, but if it stands, it is an important piece of information toward learning how vessel structure changes with age.

Without noting any differences between quasi-static and dynamic tests, multiple other investigators of cerebral arteries have similarly concluded that increases in donor age result in higher vessel stiffness (Busby and Burton, 1965; Nagasawa *et al*, 1979; Hayashi *et al*, 1980). Each of these studies were concerned with the circumferential direction, but Busby and Burton also considered axial stretch. The authors of these studies generally report and attribute the increased stiffness with an increase in vessel wall thickness with age. Like this study, however, where no significant dimensional differences were found with age, Busby and Burton found no significant change in vessel dimensions beyond the age of 30. No such studies have been published regarding the cerebral veins, but Mochizuki (1952) reported a 10-18% decrease in ultimate stress and stretch for veins

(popliteal, femoral, inferior vena cava) from 60-69 year-olds in comparison to those from the 20-29 year age group.

4.2.4.5 Confirmation of Lack of Interaction Between Main Independent Variables

Even though preliminary statistical tests checked for possible interactions between the independent variables, additional tests were performed to confirm this finding and validate the model. In general, confidence ellipses plotted for these results endorsed the approach of ignoring interactions between most of the variables. Figure 4.18, however, demonstrates two cases where, perhaps, some interaction should have been considered. Figure 4.18(a) plots the predicted change, and the variation of the change, in λ_Y and σ_Y for arteries and veins obtained through surgery, with vessels acquired from autopsy as the reference. The ellipse with the solid dot represents the anticipated changes for arteries

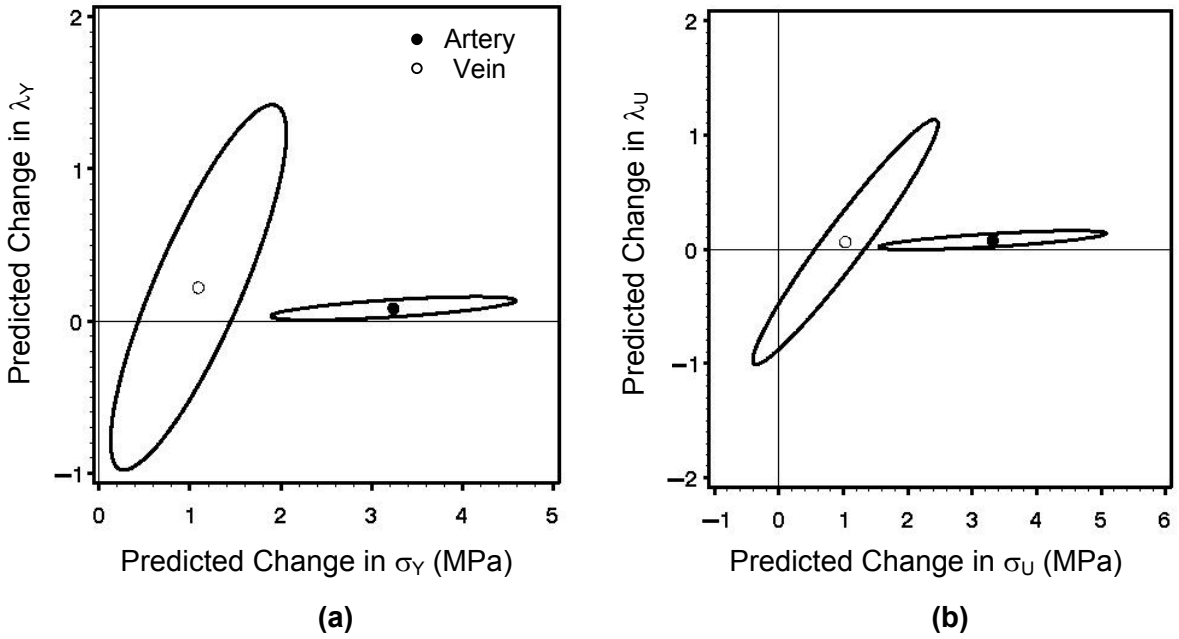

Figure 4.18 Confidence ellipses for predicted changes in (a) λ_Y and σ_Y and (b) λ_U and σ_U for vessels obtained from surgery compared to those acquired through autopsy. Predicted changes for arteries (filled dots) and veins (open dots) are given separately.

while the open dot represents those for veins. Figure 4.18(b) shows the variation in λ_U and σ_U for the same conditions. In each case, the non-overlapping confidence ellipses demonstrate that the stress measures for the arteries change by a significantly larger amount in surgical vessels compared to those from autopsy than for veins. This interaction was not accounted for in the current model but is left to be considered in future models with more extensive data.

4.2.4.6 Other Independent Variables

While a number of the independent variables were not considered beyond the exploratory tests, some of them might be expected to have a significant effect for wider variations. Larger changes in size, for example, implying the acquisition of a non-cortical vessel and a probable change in structure, would surely have an effect. Similarly, while time from resection to testing only ranged from 3-9 hours for surgical vessels and from 7.5-13 hours for autopsy specimens, longer delays would be expected to have an effect.

A lack of significance in the location of failure was also a result of the initial testing. Despite the presence of stress concentrations due to clamping, the fact that over one-third of the vessels still failed in midsection implies that the range of stress amplification due to clamping is within the variation of vessel strength due to inhomogeneity along the specimen length.

One other notable variable not included in the final model is the extent of preconditioning. While overall studies of its effect on the curve parameters don't reveal a level of significance, evidence uncovered during test analysis, as partially described below, prompted a more careful review of its influence. Based on the original data set, additional multivariate comparisons revealed a significance of the variable for arteries,

whether vessel source or test rate was considered, but not for veins. In these tests, significance was suggested for the curve parameters in all three curve regions. Test results are included in Appendix E.6.

4.2.4.6.1 Influence of Pre-stretch

One of the most difficult aspects of data analysis was the determination of the vessel reference length. As described in the procedure section, this reference was defined at the point where the load began to increase from zero following preconditioning. While the intention was to stretch the tissue to *in vivo* levels during the preconditioning process, a number of factors, including uncertainty in the *in vivo* measurement (or unavailability of a measurement) and human error or machine malfunction during testing, contributed to a more-than-desired level of pre-stretch variation. As a result, the question of how influential pre-stretch is on subsequent vessel behavior was brought to the forefront.

While it is generally agreed that preconditioning is necessary to achieve reliable measurements on soft tissue, details of the procedure, particularly to what extent the tissue should be stretched, vary significantly from investigator to investigator (Humphrey, 1995). To the author's knowledge, there has been no study published regarding the influence of variations in preconditioning procedures on subsequent vessel behavior. In perhaps the most closely related work, Schatzmann *et al* (1998) investigated tensile properties of tendon and ligament in the absence and presence of preconditioning. Mechanical, including failure, properties of tested ligaments in their study showed significant dependence upon preconditioning while the tendons did not. The tendons in this case consisted mostly of aligned collagen fibers, while the ligaments contained

mostly obliquely oriented fibers. The authors attributed the dependence of the ligaments on preconditioning to a gradual recruitment of the oblique fibers.

Figure 4.19 shows the ramp of the first cycle of a preconditioning process followed by an attempted ramp to failure (the vessel slipped from the grip before attaining a high stress level) conducted on an artery resected in surgery. The extent of pre-stretch for this case corresponds to a stretch ratio of 1.22, a value that is consistent with the range of measured *in vivo* stretch values. From the plot, it is clear that the process did slightly change the shape of the curve by shifting it to the right, or lengthening out the toe region. While it can't be seen at this scale, it is interesting to note that the reference length of the vessel remained unchanged, although the slope of the curve at the reference point is slightly lower in the ramp to failure than in the initial ramp. The plot demonstrates that the maximum slope of the curve remains unchanged.

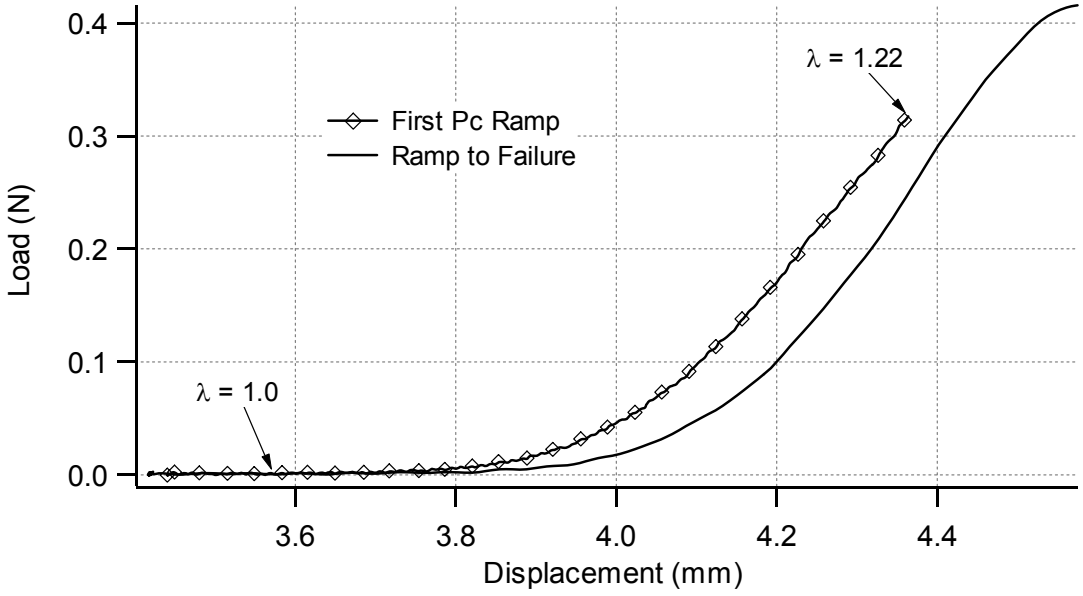

Figure 4.19 Load-displacement behavior of a selected artery during the first loading cycle of preconditioning and during the ramp to failure

To further explore the influence of pre-stretch shown in Fig. 4.19, an artery resected from surgery was subjected to a series of successively more extensive preconditioning cycles until failure. The first loading ramp of each set of ten cycles is shown in Fig. 4.20. As was seen in the previous case, each new set of data basically shifts to the right, maintaining the maximum slope until the ultimate failure point. In comparison to normal tests, the maximum overall load, occurring in Series 10 as shown, is significantly higher than that attained when yield behavior first begins to be visible. Yielding can be seen in the individual traces, or following Donovan *et al* (1990), if the maximum point of each curve was used as a point in a new curve (shown by the light, thick line), the yield point could also be identified by the distinct change in the created line's slope, as indicated in the figure. Donovan *et al* used this created line as the representation of the mechanical behavior of the vessel, suggesting that if any of the preconditioning curves was extended

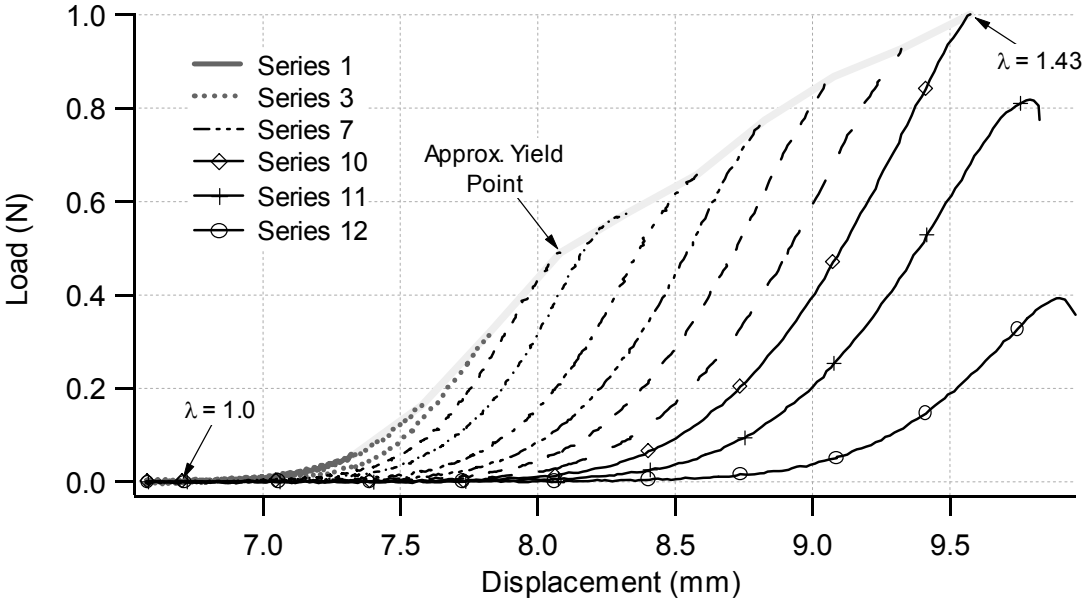

Figure 4.20 Load-displacement behavior of a selected artery subjected to successively increasing preconditioning cycles up to failure. The initial loading ramp of each set of cycles is shown

to failure, it would follow this line to the same failure point. Whether or not this is true is unknown, but the fact that the ultimate load for this case is so much higher than the yield level suggests that the extra preconditioning might have increased its ultimate properties, much like a metal being strain-hardened. Comparison of this vessel's ultimate stress and stretch, however, with results from tests where the extent of preconditioning was limited to the *in vivo* length, reveals no difference in magnitude.

The location of the reference length associated with *in vivo* preconditioning levels is indicated (as $\lambda = 1.0$) in the figure. To check for changes in the reference point with increasing stretches, the first 0.2 mm of each curve following the identified reference point was fit with a line. The resulting fits are presented in Fig. 4.21. While the slopes of the lines gradually decrease, they remain positive through Series 9. It is unknown what relationship, if any, the negative slope of Series 10 might have with the fact that this same

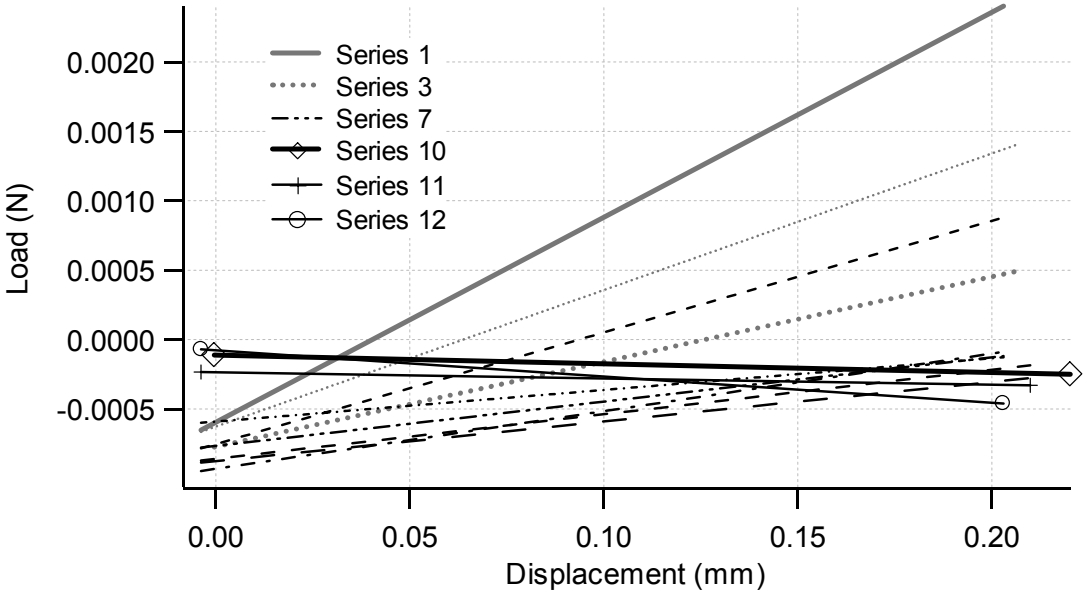

Figure 4.21 Linear fits for the first 0.2 mm following the reference of each curve presented in Fig. 4.19

curve contained the maximum load. To verify the results of the line fit, the process was repeated over the first 0.4 mm of each curve as well, giving the same transition point for positive to non-positive slope. As the vessel in this particular example has undergone extensive preconditioning, it is important to compare how its resulting behavior, taken as represented by the Series 10 trace, compares to arterial data from tests where preconditioning was not so severe. Figure 4.22 plots the stress-stretch data of Series 10 with the quasi-static arterial results previously presented and indicates that its behavior is comparable. It does, however, exhibit a slightly higher maximum modulus.

A final example of the influence of pre-stretch extent, this time on a vein resected from surgery, involves the re-testing to failure of a vessel previously subjected to a failure test. Figure 4.23 shows the stress-stretch behavior for a failure test and three subsequent tests to failure on the longest surviving segment of each test. The plot reveals

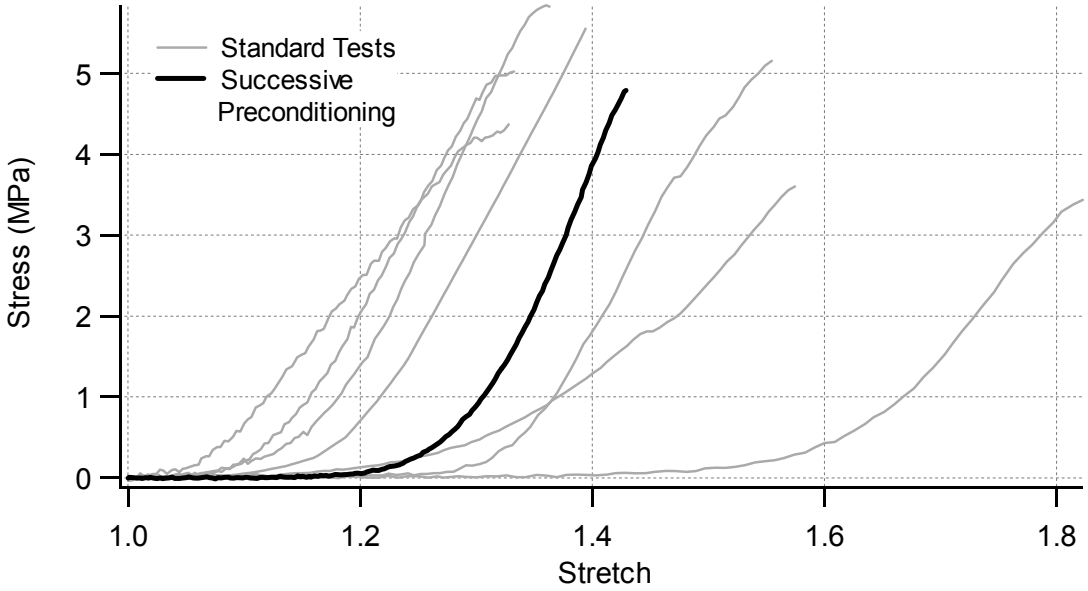

Figure 4.22 Comparison of Series 10 from Fig. 4.19 with quasi-static stress-stretch behavior of cortical arteries in standard tests

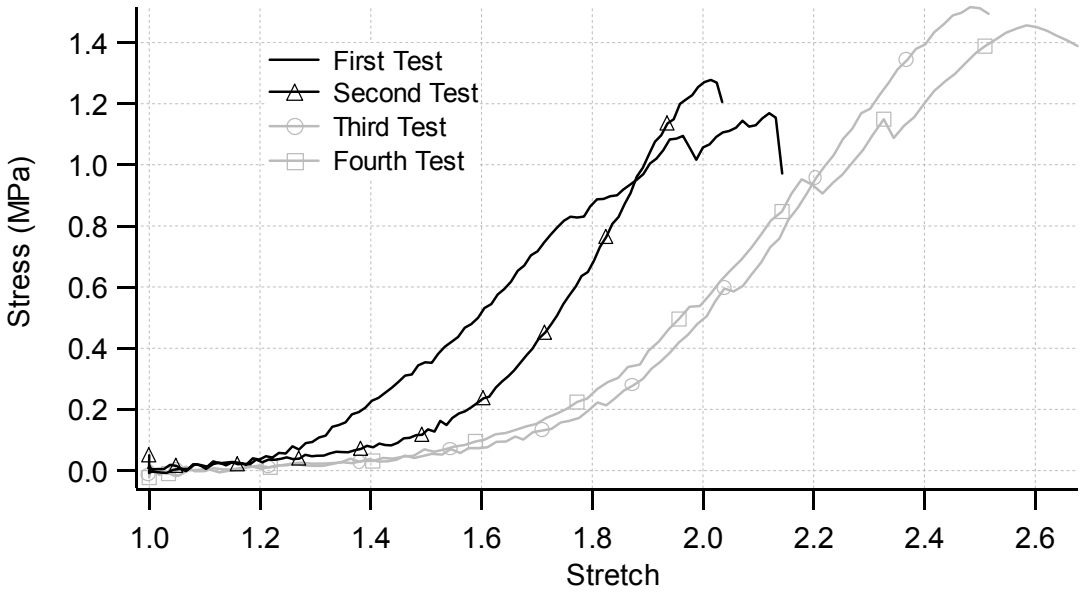

Figure 4.23 Stress-stretch results from repeated quasi-static tests to failure conducted on a cortical vein obtained through surgery

that the first two tests resulted in comparable ultimate values, as did the last two. It is expected that ultimate stresses would increase with subsequent tests, as seen, since the strongest sections of the vessel would be the last to fail. As was shown for the arteries, the toe regions of succeeding tests for this case also grow longer. It is not clear whether or not the reference length has changed with each repetition since each segment has a different length and was loaded into the test fixture separately. Focusing on the first two tests, it is clear that the initial one began to yield at a stress of about 0.8 MPa, following which the curve was non-uniform until ultimate failure. In comparison, the second test displays a great deal more smoothness over its whole range. The maximum slope of the second test is also higher than any of the other cases, suggesting that it possibly suffered no damage during the initial high level of pre-stretch.

With the preceding discussion focusing on the influence of extent of preconditioning, no mention has been made of the method. As indicated, the typical approach to the process is a series of cycles. The cycling is continued until a steady-state is obtained. In a couple of the present tests, stress-relaxation processes were combined with cycling as a means for preconditioning. Figure 4.24 shows one such case. The specimen was first cycled between its reference and *in vivo* length ten times, then ramped up to that length and held for five minutes. Following the stress-relaxation, the specimen was again cycled between the two lengths. While it was believed that steady-state had been reached following the first set of cycles, the tissue continued to soften during the stress-relaxation procedure, following which the repeated cycles were very consistent. Since it appears that the cycling is doing little besides relaxing the tissue, it seems quite possible that such a relaxation process may be used in place of cycling to achieve similar results. Further

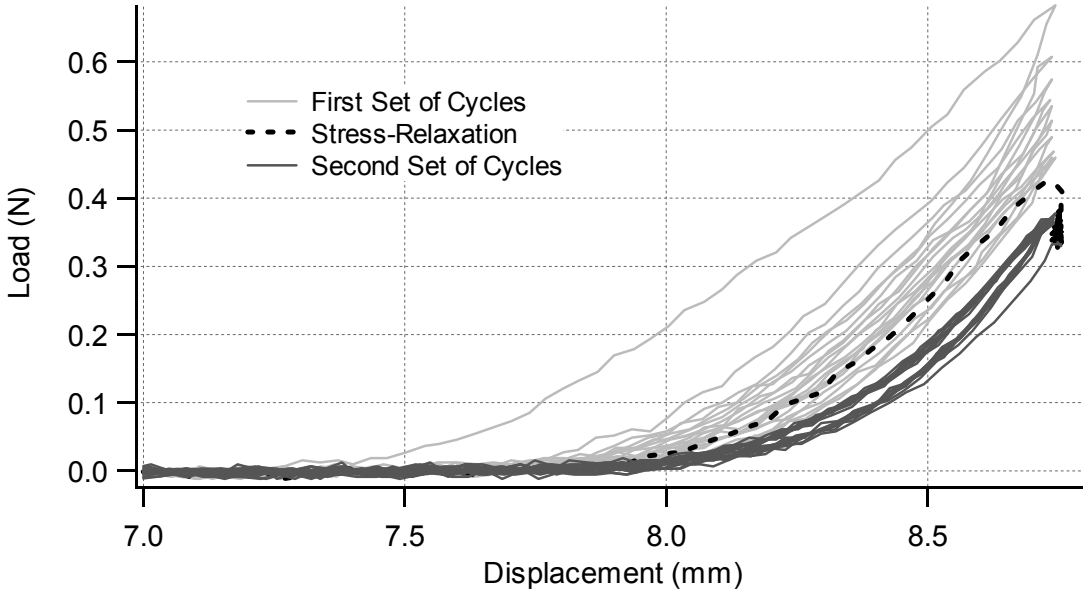

Figure 4.24 Load-displacement behavior of a selected artery during preconditioning. The process consisted of two sets of ten cycles, with a five-minute stress-relaxation period between them.

investigation of this question is reserved for later time.

Whether or not the observations of these examples would hold true for a collection of arteries and veins is left to be explored in a future study. Although additional tests must surely be conducted to explore the influence of pre-stretch on the mechanical properties of blood vessels, it is clear that the effect is significant, arguing for the standardization of preconditioning protocols (Humphrey, 1995). Based on the cited examples, it appears that the reference length of a specimen does not change for variations in extent of preconditioning, even when pre-stretch levels approach the ultimate failure point. The maximum slope of the individual stress-stretch curves is similarly unchanged (or increased), even though yield behavior is visible, until failure occurs. It is also clear, however, that the curve shape at low stresses is changed, with a lengthening out of the toe region over a larger range of stretch but, again, not changing the reference length. In light of these observations and based on what has been suggested by previous researchers (Roach and Burton, 1957) that the low-stress portion of the curve is determined by the elastin fibers in the vessel and the high-stress region by collagen, it could be concluded that the demonstrated yield behavior is associated with elastin and not collagen. It is also quite possible, however, that the behavior is not due to failure of elastin fibers but to a restructuring, wherein the interconnections between the elastin and other components of the vessel wall (e.g., collagen and smooth muscle) are either broken or moved. Consideration of the fact that cerebral veins contain very little elastic material compared to the arteries, along with the suggested influence of pre-stretch on elastin, seems to explain the predicted significance of pre-stretch on arteries but not on veins in the current tests. Further, the evidence of increasing moduli and smoother traces with high-stress pre-

stretches also suggests a more efficient recruitment of collagen, as was shown by Schatzmann *et al* (1998) with ligaments. While the preceding examples highlight changes in the vessel behavior at sub-failure loads, the question of whether or not preconditioning affects failure properties remains.

4.2.5 Data Analysis Considerations

4.2.5.1 Measurement of Cross-Sectional Area

One of the major factors influencing the results of this study was the accurate measurement of cross-sectional area. Video resolution of cross-section images varied slightly from case to case, but most images were captured with a resolution on the order of 5 μm/pixel, with the vessel outer diameter typically around 500 μm. While this was considered to be a sufficient level of accuracy for this measurement, the wall thickness of these vessels, based on this approach, were often near 50 μm, challenging the ability of the technique to produce accurate results. Further, as has been described and as was shown in Fig. 4.1, vein walls in particular tended to collapse, departing from the typical round shape and making it difficult to distinguish the profile of the vessel.

In addition to the difficulty associated with microscopic measurements, each vessel was expected to display some level of dimensional inhomogeneity along its length. While in most cases cross-sections were only available from the ends of specimens, one harvested segment that was too short to test was sectioned along its length to get a sense of what sort of variation might be expected in these vessels. In seven different sections, area measurements ranged from 0.164 to 0.233 mm^2. For a load of 1 N, this represents a variation in stress from 4.29-6.10 MPa. While it is difficult to know how typical this variation is without a comparison of more samples, it does provide an idea of what to

expect. Assuming that end sections used for measurements were taken sufficiently far away from cauterized tissue, it seems appropriate to suppose that relatively large and small sections were selected at random frequencies so that the biological scatter present in the final results is partially generated by any such dimensional inhomogeneities. Thus, studies for significance already incorporated this variation.

Since most of the tested vessels were of a similar size, the possibility of studying the load-stretch response instead of stress-stretch behavior, as a means for eliminating the discussed variation in measurement was considered. Load-stretch plots, however, were found to show a higher level of variation than did stress-stretch ones. As a result, despite the difficulties discussed, it was assumed that the area measurements had been conducted at an acceptable level of accuracy.

4.2.5.2 Stretch Homogeneity

Another important factor affecting the accuracy of the presented results is the measurement of stretch. As has been discussed, it was assumed that the stretch was uniform along the length of the specimen, so devices associated with the testing apparatus that measure grip displacement were used to calculate stretch. In each case, this uniformity was verified through the use of a video camera and stain markings applied to the vessels. Video images typically provided resolutions around 0.05 mm/pixel, which was considered to be sufficient for the tested segments, which typically had lengths greater than 5 mm. Stretch homogeneity, however, was found to be a valid assumption only up to the point of yield, after which further deformation was largely restricted to the region of ultimate failure. Despite the lack of uniformity between the yield and ultimate points, displacement data was still utilized to approximate this region. The resulting

stretch measurement in this section of the curve, then, tends to underestimate the actual stretch at the site of failure and overestimate it elsewhere in the vessel. While video could be used to more accurately quantify the stretch associated with various regions of the specimen, the exact portion of the vessel that is failing is difficult to identify, producing similar difficulties.

4.2.5.3 Identification of the Reference Length

The difficulty of proper determination of the reference length has been highlighted in the discussion of preconditioning. Neglecting, however, any load-induced material changes that may complicate the reference used throughout the testing of a specimen, there is little question that the current method of reference identification is likely to produce slightly different results depending upon the analyst. As a result, this must be considered when comparing the present data to that of any other investigator.

4.2.6 Summary

The previous sections report the measured mechanical and failure properties of cortical arteries and veins, obtained both through surgery and from autopsy, for a series of quasi-static and dynamic tests. In general, veins were found to fail at stress levels of about half those for arteries, but they were capable of withstanding approximately twice the amount of stretch. Statistical analyses showed that differences between arteries and veins were significant. The reported data suggested that the source of the vessels (whether from surgery or autopsy), the rate of testing, and the age of the donor were also influential factors in some measured property values. A proposed dynamic model of the load cell-grip-vessel system brought the importance of testing rate into question, suggesting that some of the measured differences between data from quasi-static and

dynamic tests may be artifactual. Although it was not included as an independent variable in the statistical model, the importance of the extent of preconditioning was considered. Evidence from case studies argues the importance of more research of this phenomenon. Changes of vessel behavior induced by pre-stretch appear to provide additional insight into the load-carrying contributions of various wall components. All of these results point toward ways to better link vessel wall structure with mechanical behavior and underscore the need to learn more about how structure changes for variations in the discussed independent variables.

4.3 MECHANICAL TESTING — INFLATION

4.3.1 General Observations

Figure 4.25 shows a series of images from a typical inflation test on an artery, with each frame separated by 10 sec, except for the last two which are separated by 4 sec. The ends of the specimen were secured to the needles using sutures, as the figure shows, and cyanoacrylate glue. Were the images presented in color, the vessel boundaries would be more visible, but the figure illustrates the transparent nature of these vessels and some of the difficulty associated with measuring their dimensions during testing. The ragged look of the boundaries in some areas is due to surrounding tissue which was not completely dissected away. As was true in this case, tests achieving failure via bursting generally ruptured in midsection – the final image shows dyed fluid escaping from the vessel. Figure 4.26 shows the pressure-circumferential stretch trace for the test shown in Fig. 4.25, along with its accompanying preconditioning behavior. As the data indicates, the diameter of the preconditioned vessel was significantly larger than before it was pressurized, something that was fairly common in the few tests conducted. The brief, sub-

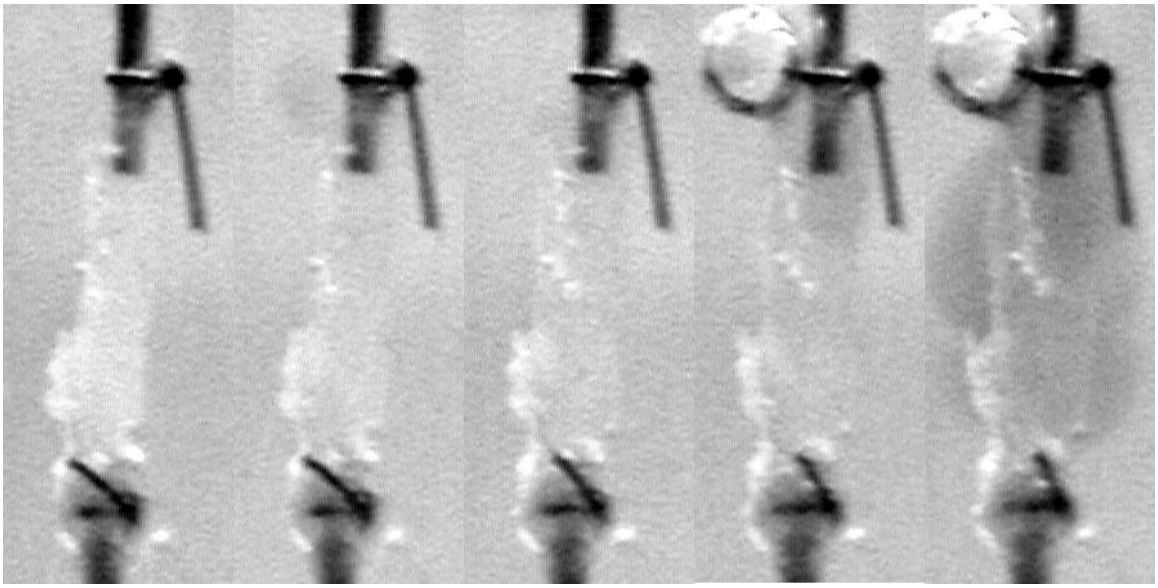

Figure 4.25 Inflation test image sequence for a selected artery. Frames are separated by 10 sec (except for last two-separated by 4 sec). The diameter of the cannulating needles is 0.41 mm.

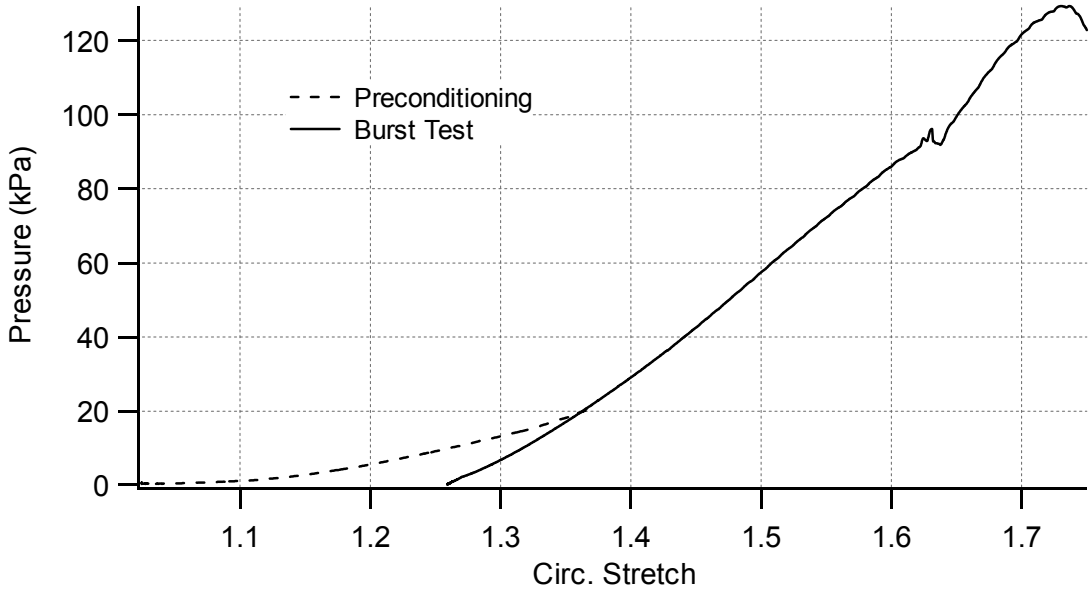

Figure 4.26 Pressure-circumferential stretch response of artery shown in Fig. 4.25. Both preconditioning and burst data are shown.

failure drop in the pressure trace for this test was associated with a momentary leak at the vessel end that inexplicably disappeared shortly after it became visible.

In general, for tests in which pressure was increased while maintaining the vessel at its reference length, sealing the vessel to the needle with only glue proved sufficient to prevent leakage, even at bursting levels. For cases where some tension was generated in the vessel prior to inflation, however, the glue-only bond was weak and would allow the specimen to slip at small loads. In these cases, successful bonds were developed by using needles with epoxy bulbs on the ends of them, tying the vessel ends off on the back side of the bulbs with suture or wire, and covering the ends with a layer of glue. Because of its ability to maintain a deformed shape, the wire proved to be simpler to work with than the suture to accomplish the tying process.

As was indicated in Section 4.1, veins more commonly had longer sections with no minor branches in comparison to arteries. Despite this fact, significantly fewer veins were tested successfully in inflation.

4.3.2 Measurements – Arteries

Figure 4.27 shows circumferential stress-stretch results for each of the four arterial inflation tests that was successfully carried out to failure. For each case, the length of the specimen was held constant at the axial stretch indicated by the number at the end of the applicable curve. As shown, axial stretch varied from 0.92-1.18 through the different tests and proved to have a significant influence on the resulting circumferential measurements. Since only a few tests are available for study, it is impossible to know how representative they are, but it is clear that higher levels of axial stretch resulted in higher circumferential stresses at smaller circumferential stretches, as would be expected, While this is generally

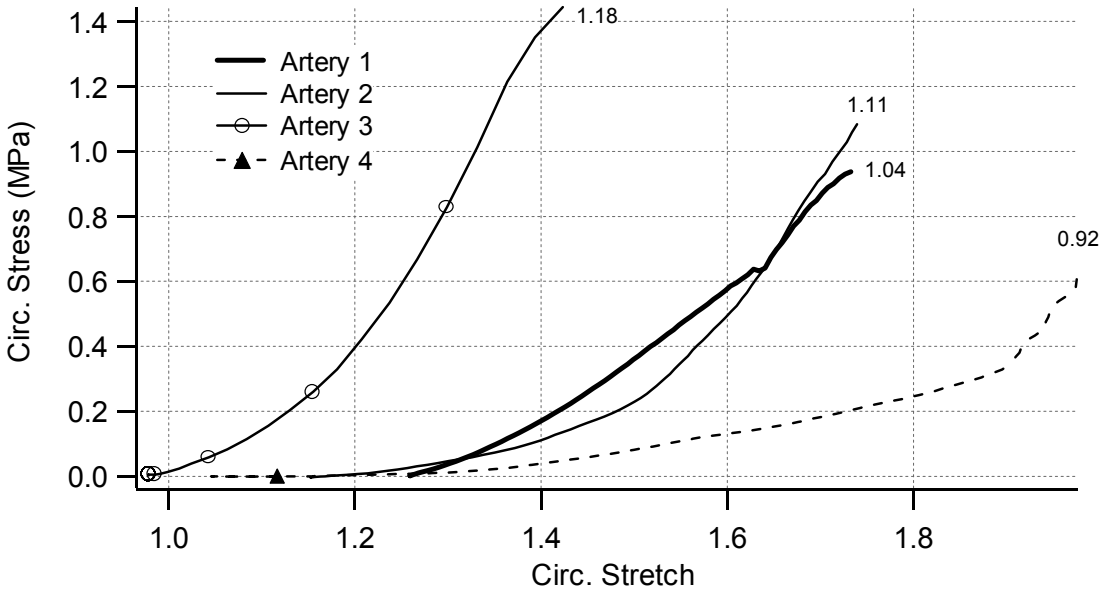

Figure 4.27 Circumferential stress-stretch behavior of cortical arteries at different values of axial stretch, indicated by the number at the end of each trace.

true, the large difference in axial stretch between Arteries 1 and 2 doesn't appear to have had much of an effect. The cases also suggest that higher axial stretches produce steeper circumferential stress-stretch curves, at least in the lower portion of the curve. It is unknown whether the distinct, two-phase behavior of Artery 4 is anomalous data or if it is result of structural differences associated with a sub-unit axial stretch. The maximum slope appears to be similar for the four tests. Further, the plot suggests that larger axial stretches result in higher ultimate stresses and lower ultimate stretches in the circumferential direction.

In the consideration of these results, however, it is important to note that the circumferential stress is calculated using the assumption of incompressibility, the measured axial stretch, and measurements of current radius and reference wall thickness, as indicated in Section 3.3.5.1. While incompressibility has been shown to be a reasonable assumption for blood vessels at physiological levels, how valid it is at these

extreme deformations is unknown. Further, with the present technique, the measurement of reference wall thickness is somewhat imprecise. Also, resolution of video images of inflation tests were typically around 0.015 mm/pix, but changes in diameter were commonly around just 0.2 to 0.4 mm. As a result, more data and advancements in measurement procedures, in addition to testing for incompressibility at high load levels, are needed to corroborate the presented circumferential stress-stretch results. Figure 4.28 presents the data in terms of pressure-diameter to eliminate some of these unknowns. While the plot says little about the value of the stress-stretch results, there is greater similarity between the four traces here than in the previous figure. The pressures achieved before failure were generally around ten times higher than typical physiological loads (1000 mmHg = 133.3 kPa).

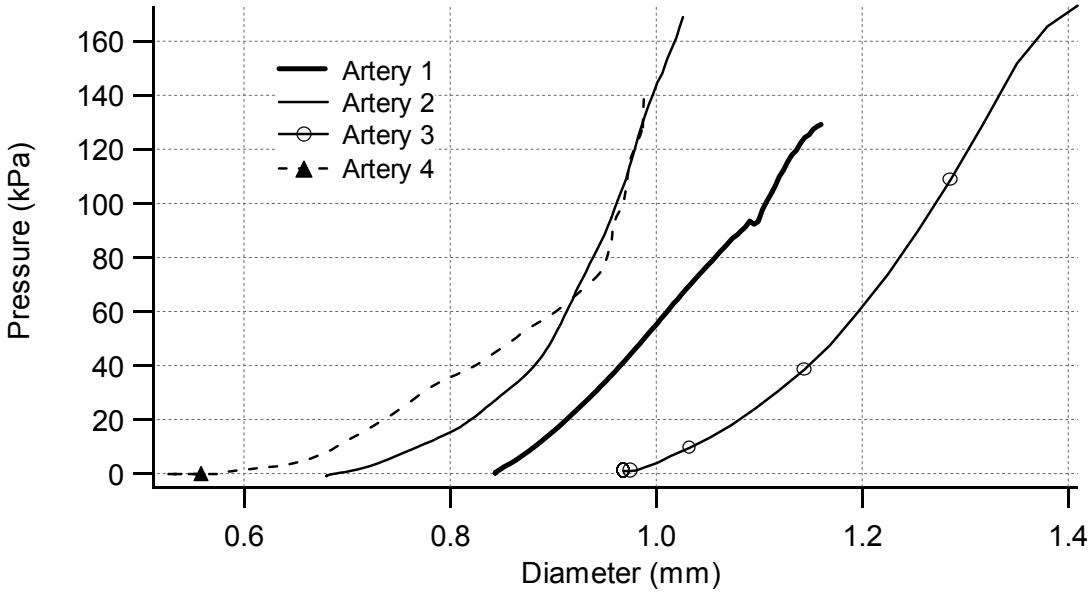

Figure 4.28 Pressure-diameter behavior of cortical arteries from surgery subjected to inflation and stretch. The inflations were conducted at various levels of axial stretch, as indicated in Fig. 4.27.

It has been reported (Brossolet and Vito, 1995; Humphrey, 1995) that when a passive blood vessel is stretched axially to its *in vivo* length and pressurized, the measured axial load remains constant for changes in pressure. This has been referred to as the "*in vivo* property" of the vessel. When, however, the vessel isn't stretched as far as the *in vivo* length and is pressurized, the measured axial load decreases with increases in internal pressure, and for stretches beyond the *in vivo* length, the load increases with internal pressure. No definite explanation for this phenomenon has been offered, but it is considered to be an important feature of combined inflation-stretch behavior of blood vessels. Figure 4.29 plots the measured axial load as a function of circumferential stretch for the four arterial inflation tests and demonstrates the presence of this phenomenon in the cerebral vessels. Axial stretch values are indicated at the end of each trace. Although Artery 3 was only stretched to 1.18 axially, it appears to have been beyond its *in vivo*

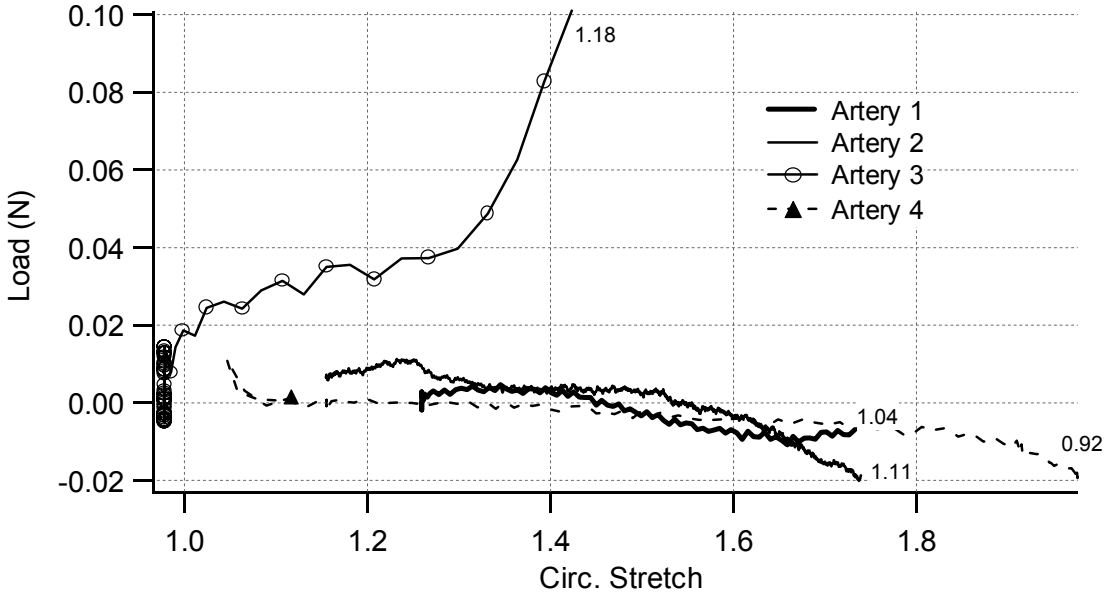

Figure 4.29 Axial load-circumferential stretch response of arteries inflated to bursting. Constant axial stretch value for each test is indicated at the end of each curve.

stretch level. The other vessels appear to have been stretched somewhere below their *in vivo* stretch level.

While no circumferential stress-stretch behavior of cerebral arteries and veins is available in the literature, bursting pressures from the current tests are on the same order as those reported by Groenink *et al* (1999) for thoracic aorta.

4.3.2.1 Influence of Preconditioning

Figure 4.30 repeats the results of Artery 1 previously given in Fig. 4.26 but shows the circumferential stress-stretch data instead of the pressure-stretch results. For this specimen's preconditioning, the axial stretch was held at a value of 1.04, as in the subsequent burst test, while the vessel was pressurized to 20 kPa (150 mmHg) and held for about a minute. This loading scenario was expected to be rather light since the axial stretch was not increased beyond the reference. Nevertheless, the difference between the

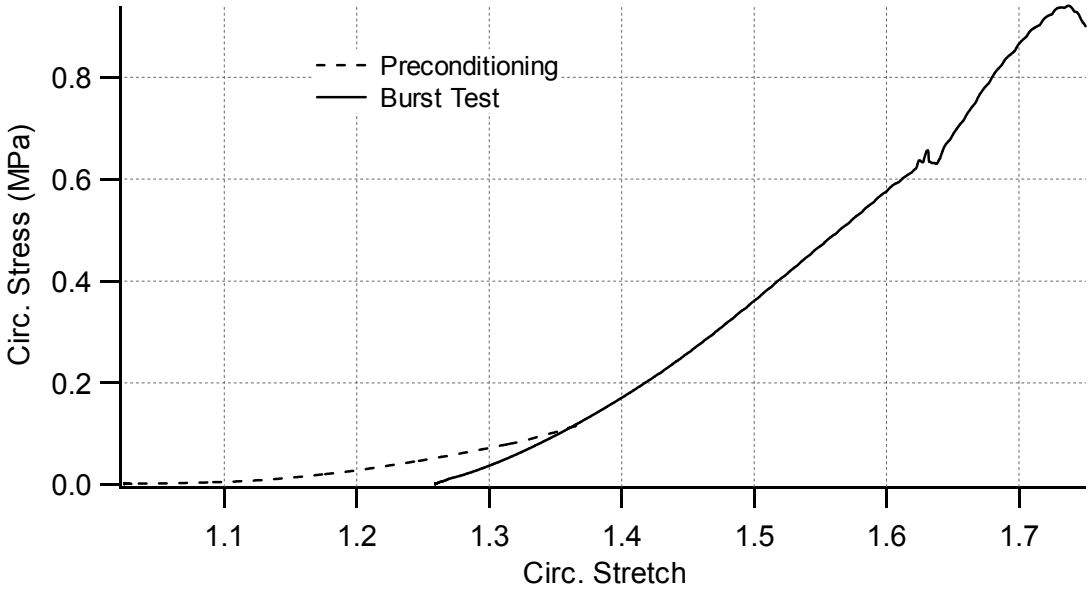

Figure 4.30 Circumferential stress-stretch response for Artery 1. Preconditioning and burst data are included.

starting points associated with the preconditioning and burst traces suggests a large change in the reference point. Additionally, the burst trace displays significantly less curvature in its lower section than does the preconditioning data. It is possible that upon resection, the portion of the structure of these vessels that determines their circumferential properties is dramatically altered due to the lack of load. Then, the changes seen here may only be a necessary restructuring, returning the vessel to its *in vivo* condition. Such a large change, however, is not expected.

Scott *et al* (1972) reported a somewhat similar finding in their study comparing cerebral arteries and aneurysms. They found that aneurysms were much less distensible than healthy arteries, particularly in the initial, elastin-dominated portion of the curve, much like the difference seen here between the preconditioning and burst traces. Further, these investigators found that after three repeated pressurizations of healthy arteries to 200 mmHg, they began to behave more like the aneurysms, with much less distension at low pressures. They attributed these differences to changes in, or damage to, the elastin structure of the vessels. While the vessel in the present case was not subjected to pressures quite as high as 200 mmHg, it was held at 150 mmHg for a significant length of time, possibly resulting in similar consequences for the elastin structure.

4.3.2.2 Comparison of Longitudinal and Circumferential Properties

Taking the circumferential stress-stretch data to be representative allows a comparison of the properties of cortical arteries in the longitudinal and circumferential directions. In the four inflation cases, the maximum modulus ranged from 3.4-5.4 MPa, about one-fourth the value of the average measure for longitudinal studies of cortical arteries from surgery. Ultimate stresses were also approximately four times higher in the

longitudinal direction than circumferential, at least for the cases near $\lambda_z = 1.0$. While both of these parameters are dependent upon an accurate calculation of stress and must thus be regarded as preliminary according to the above discussion, the measurement of stretch is not subject to these errors. Again considering the cases where axial stretch was near the reference, the figure indicates ultimate stretch around 1.7, compared to 1.4 for the longitudinal direction. These results, then, suggest that the cortical arteries stretch are less stiff in the circumferential direction but can withstand larger stretches than the longitudinal.

Combining what was reported earlier with regard to the effect of preconditioning in the longitudinal direction with the above discussion on preconditioning through pressurization, it appears that the contribution of elastin to distension behavior in the two directions is distinctly different. It is particularly interesting that the reference point for stress increases appears to be more subject to change in the circumferential direction than in the longitudinal one.

4.3.3 Measurements – Veins

Figure 4.31 presents the most successful inflation test on veins. The presented tests correspond to the same vein, with pressurization at the two different axial stretch values indicated in the figure. Even though there were large changes in the radius, the circumferential stresses clearly did not rise to significant levels. Measured maximum pressure values were 0.61 and 0.77 kPa for the two tests. Nevertheless, as was the case for arteries, the axial stretch plays a significant role in the circumferential stress-stretch behavior for veins. The large changes in circumferential stretch also suggest an expected

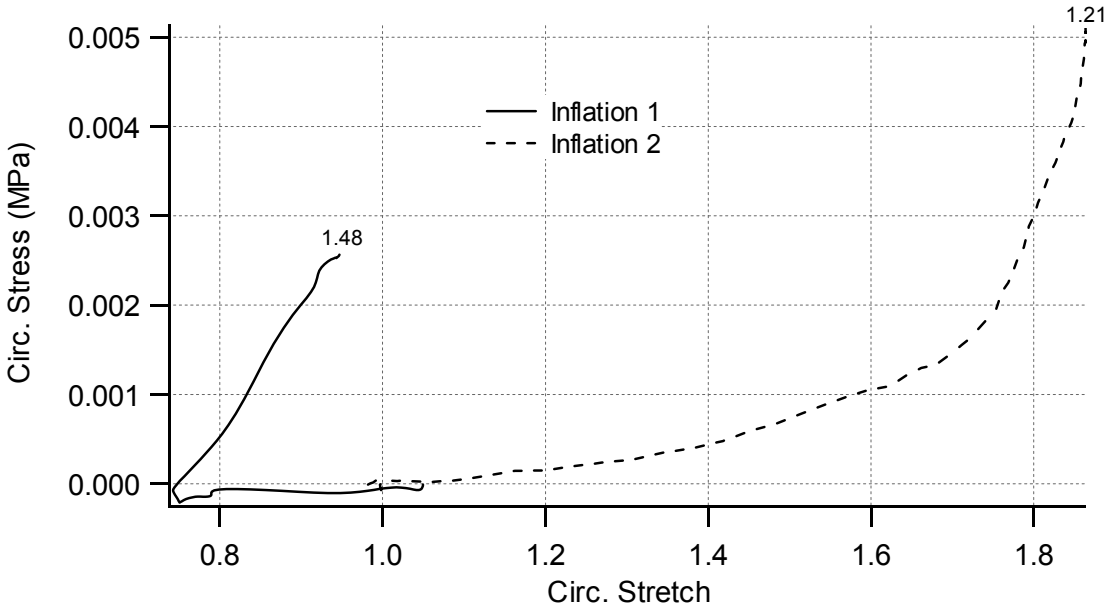

Figure 4.31 Circumferential stress-stretch results for two sub-failure inflation tests on a vein. Constant axial stretch values are given at the end of each curve.

high distensibility relative to the arteries, as with longitudinal tests, although the differences in scale really don't allow a reliable comparison.

4.3.4 Summary

Inflation tests on four arteries and one vein demonstrate an expected significant dependence of circumferential behavior upon axial loading conditions. A comparison of results from inflation and longitudinal stretch tests on arteries suggests that cortical arteries are stiffer and are able to withstand more stress in the axial direction and that they are able to attain greater stretches in the circumferential direction. Additionally, circumferential preconditioning data, like that seen in the longitudinal results, points toward elastin as the main load-carrying component of the vessel wall to be influenced by pre-stretch. While the reference length in longitudinal tests was unlikely to change as a

result of preconditioning, the reference diameter in inflation procedures is likely to shift, even at levels of loading associated with healthy physiology.

4.4 MATHEMATICAL REPRESENTATION

Since one of the main motivations, at least in the context of head injury, for the study of cerebral blood vessels is their implementation into computer models, it is necessary to represent their responses mathematically. The two following sections discuss simulation options for uniaxial and biaxial cases. Although current whole head models are constrained by memory restrictions to utilize a uniaxial representation, more refined models, intended to analyze the response of a small region of the brain, may incorporate the described two-dimensional behavior.

4.4.1 Uniaxial Description – Longitudinal Direction

As has been discussed, longitudinal stress-stretch curves in this study were characterized by breaking each curve up into three parts. The first, the toe region, was modeled as an exponential. The second, a section between the toe region and the yield point, was usually still slightly nonlinear but not enough so to allow representation by the toe region exponential. The final portion, between the yield and ultimate points, is probably best described as a concave-downward quadratic. Although some numerical models might allow a simulated vessel's response to be defined from a data file, it is usually preferred to represent a structure's behavior by a single function. For these vessels, a polynomial is likely the only form that could accommodate the three regions together, but the coefficients of polynomials (of at least third order) are difficult to relate to material properties and so are not preferred.

One option to a polynomial, besides accepting a less accurate vessel representation, is to restrict the range of stretch over which simulation is required. Most applications, including head injury modeling, probably don't need to define response through all three regions of the blood vessel stress-stretch curve. Figure 4.32 shows a selected arterial trace with exponential fits over three ranges. One fit spans the whole range of stretch, the second is limited to points below the yield point, and the third spans the region between the *in vivo* stretch and the yield point. As the figure shows, the weaknesses of the exponential fits are an overestimation of stress at low stretches and an underestimation at higher ones. The smallest span, however, provides a reasonable representation, at least for the range of stretch one might be interested in modeling for head injury scenarios. Thus, as others (Tanaka and Fung, 1974; Hayashi *et al*, 1981) have reported that exponential fits provide a good model for uniaxial blood vessel behavior over some

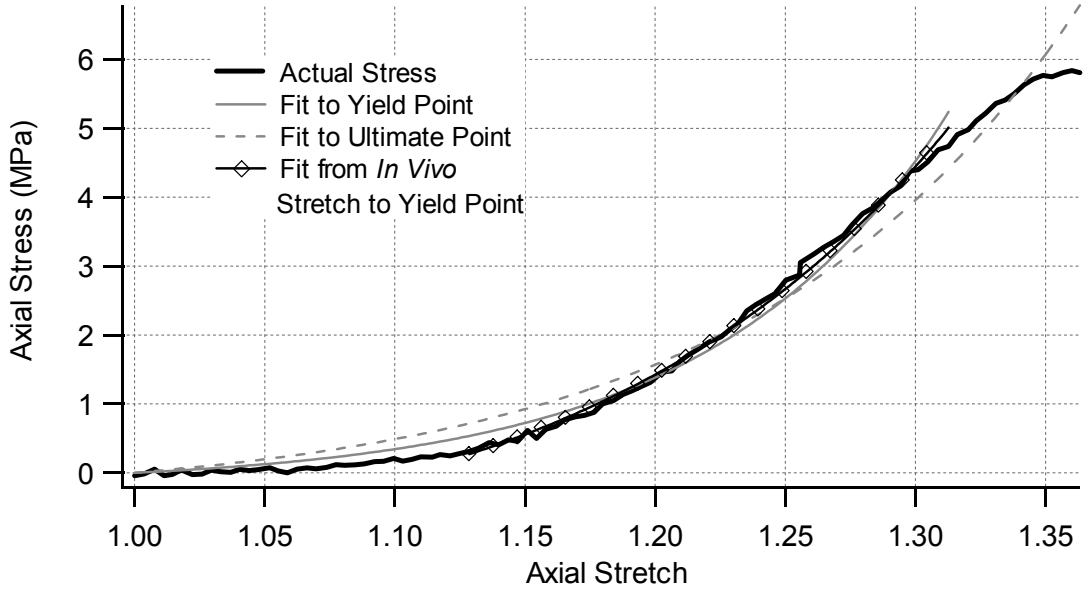

Figure 4.32 Uniaxial stress-stretch response for a selected artery, along with exponential curve fits over three different regions

portion of the stretch range, the same is noted here.

Because the arterial (and venous) data are spread widely across the stretch axis, an attempt at exponential curve fitting using all the data from one vessel type together results in a concave downward curve, as the fitting process attempts to accommodate the many points of high stress and moderate stretch and a few points at high stretch but not particularly high stress. Thus, instead of providing coefficients for a fit of the average data, Figs. 4.33(a) and (b) show two selected arterial and venous traces, respectively, that represent a good range of the data and their individual exponential fits over the full, or near full, range. The coefficients for the fits, A and B, are given in the context of Equation 3.2. Fit ranges for the veins were shortened because of their particularly lengthy yield regions.

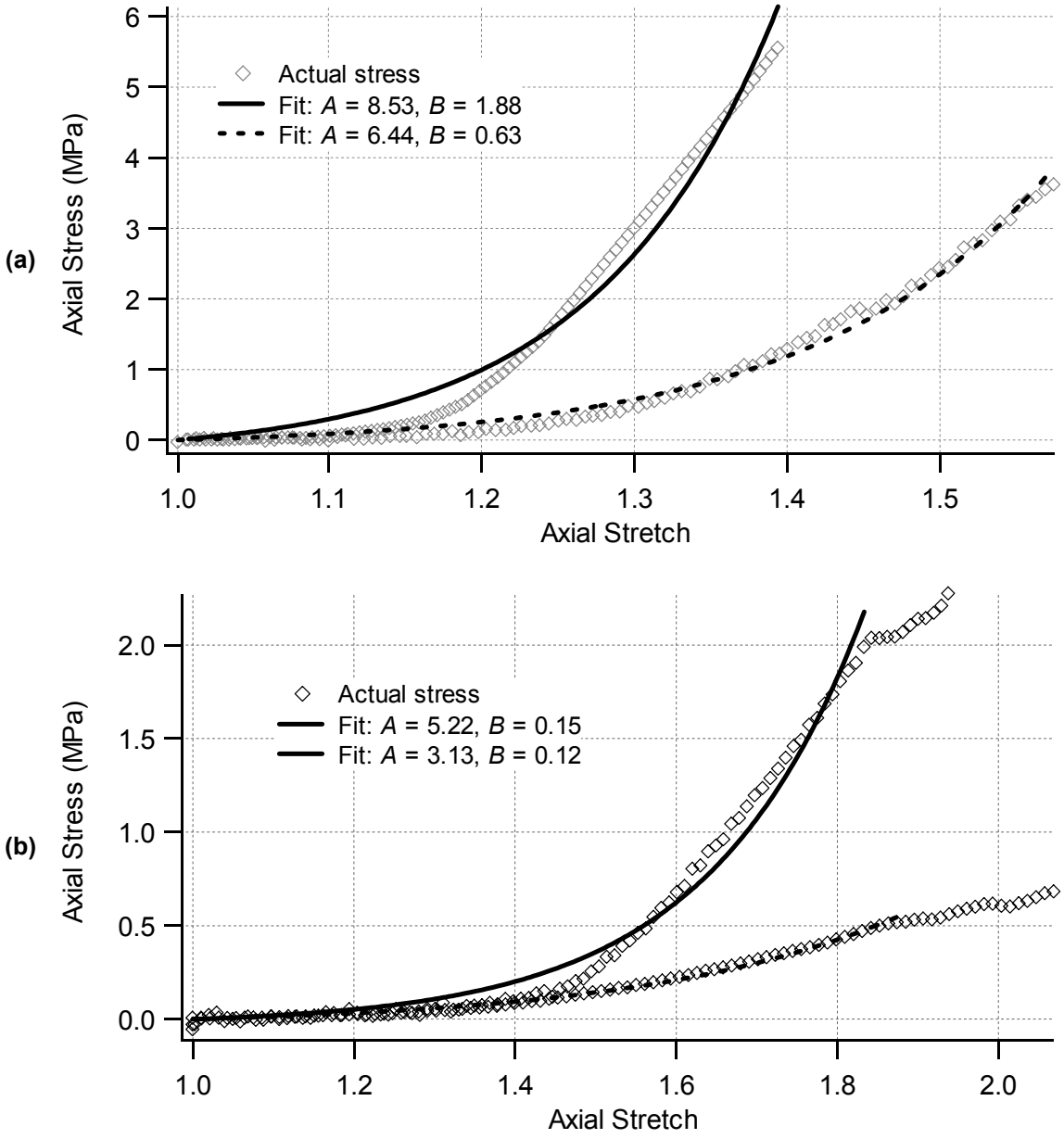

Figure 4.33 Axial stress-stretch behavior of two selected (a) arteries and (b) veins, along with exponential fits over their full, or near full, ranges. Coefficients for the fits, defined in the context of Equation 3.2, are given in the figures.

4.4.2 Biaxial Description

For the consideration of biaxial behavior, data was fit to the two-dimensional exponential model introduced by Fung *et al* (1979) and given by Equation 3.4. Figures 4.34(a) and (b) present longitudinal and circumferential data and resulting fits for

selected arterial stretch and inflation tests. To make the figure easier to interpret, data and fits were included for just three arterial stretch tests and for the four inflation tests that resulted in failure. The coefficients defining the fits, however, were determined using all acceptable data from quasi-static stretch and inflation experiments. The one very-large-stretch arterial stretch case was not considered since it was so different from the other cases and had a large impact on the resulting overall fit.

It was shown earlier that an exponential function has difficulty representing the longitudinal stretch behavior over a large stretch, but when multiple traces are considered, the fit is, of course, even less accurate, as Fig. 4.34(a) demonstrates. Additionally, the longitudinal stresses that developed during inflation tests (the data points that increase for a single value of axial stretch) are not captured at all by the model. In part (b) of the figure, the model does predict slightly higher circumferential stresses for tests with larger axial stretches, as expected, but it cannot perform to the extremes the data require.

Coefficient values for this combination fit, along with a measure for goodness of fit (χ^2), are given in Table 4.3. The coefficient for the longitudinal stretch, b_2, is an order of magnitude higher than the other "directional" coefficients (b_1 and b_4), indicating that

Table 4.3 Coefficients of Fung-type strain energy function for combination longitudinal stretch and inflation data, as well as for longitudinal and inflation data considered separately.

	c	b_1	b_2	b_3	*Goodness of Fit (χ^2)*
Combination of longitudinal stretch and inflation	650.6	9.8e-5	0.0016	1.9e-5	1185.08
Combined longitudinal stretch	483.4	-7.3e-4	0.0022	-3.9e-4	969.96
Combined inflation	0.19	0.15	0.78	0.31	25.17

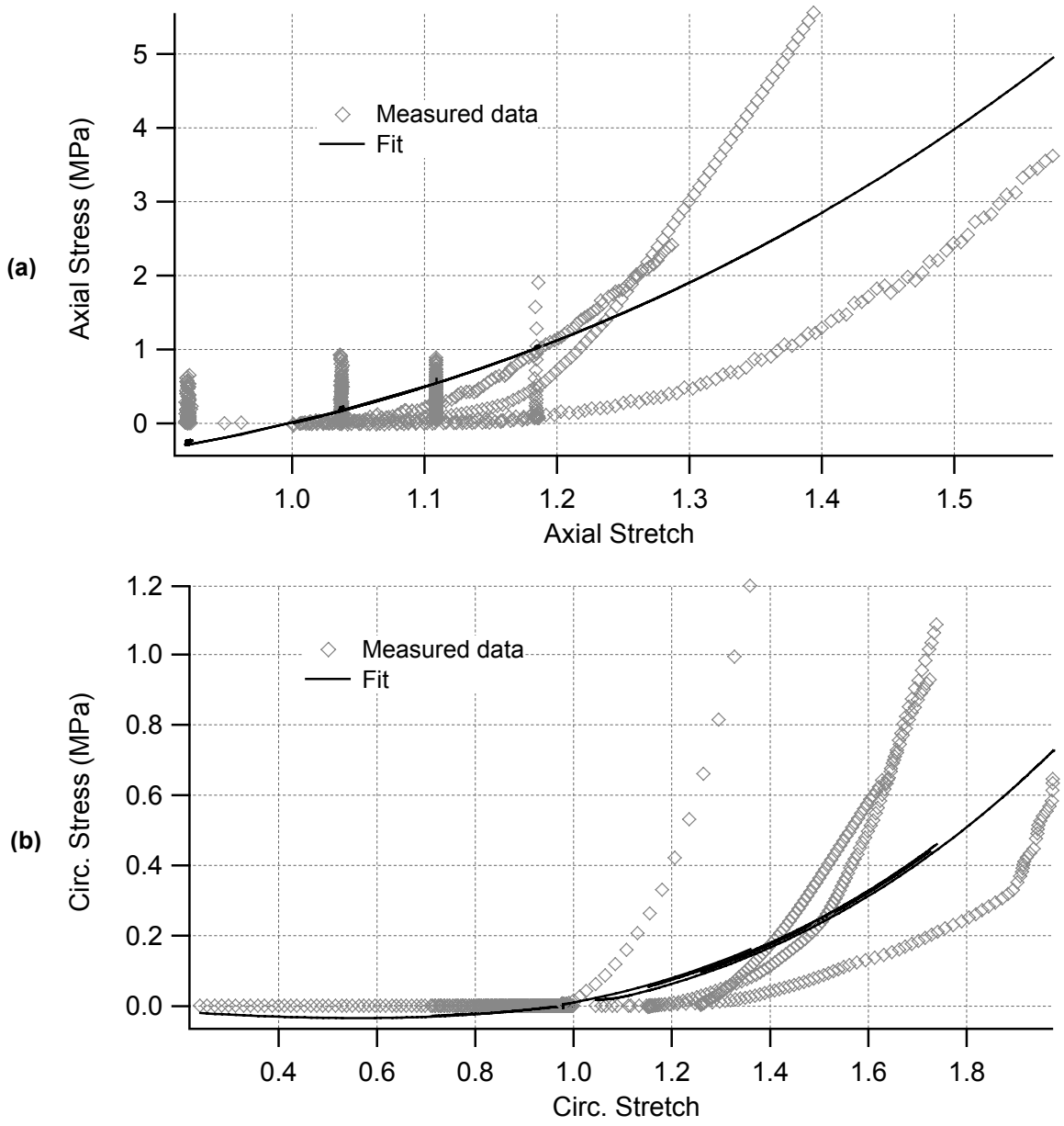

Figure 4.34 (a) Longitudinal and (b) circumferential data and fits for selected arterial cases, based on coefficients determined from all axial stretch and inflation tests.

larger changes occur in the model for longitudinal stretches than for circumferential ones. This fact is clear from Fig. 4.34 and is also in qualitative agreement with the conclusion reached previously in the discussion on inflation results that the longitudinal direction is

stiffer than the circumferential one. The χ^2 value is very large, as might be expected based upon the quality of fit demonstrated in the figures.

As Table 4.3 indicates, the model was also fit to longitudinal stretch and inflation data separately. The respective longitudinal and circumferential data and fits for these cases are presented in Figs. 4.35 and 4.36. As shown by the table and Fig. 4.35, the fit for the longitudinal data alone did not change much from the overall combined case, although b_1 were b_4 are negative. According to Holzapfel *et al* (2001), negative coefficients in this model violate convexity / stability requirements, and they result in a model that may give physically unreasonable predictions (Humphrey, 1995). These problems may be a result of poor circumferential stretch approximations for longitudinal tests, since camera field of view had to be larger during axial stretch experiments than for inflation tests.

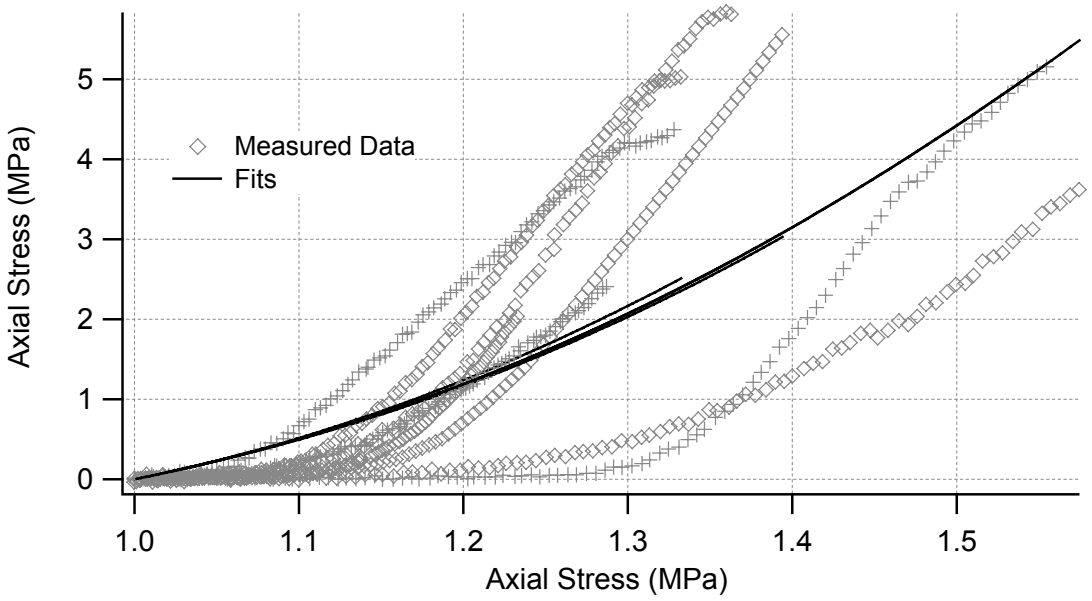

Figure 4.35 Axial data and fits based on coefficients determined using longitudinal stretch tests only.

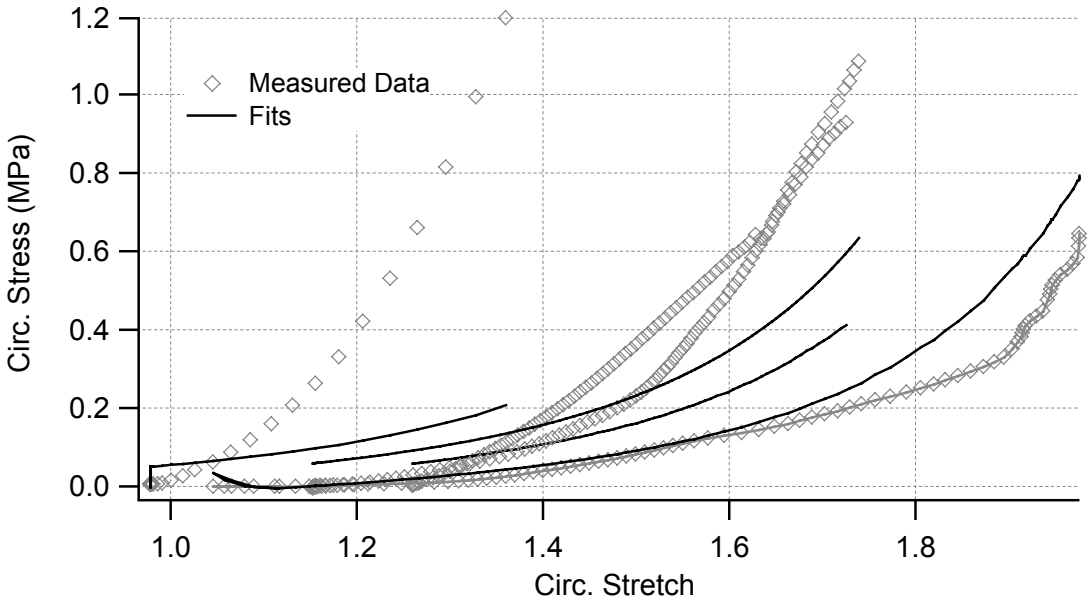

Figure 4.36 Circumferential data and fits based on coefficients determined using inflation data only.

In contrast to the lack of change between the fits associated with the first two data collections, the circumferential fit from the inflation data shown in Fig. 4.36 demonstrates much better predictions, although they are still quite poor. Coefficients for the combined inflation fit are dramatically different than for the other collections of data, with substantially higher values for the directional coefficients and a much lower number for *c*. Despite the large changes, the greater stiffness of the longitudinal direction as compared to the circumferential is preserved. The smaller relative value of *c* also gives the directional coefficients more influence and allows for more anisotropy in the model. Figure 4.37 shows the predictions of this particular fit for a selected longitudinal trace, demonstrating, like in the circumferential direction, that this fit also underestimates stresses in the axial direction.

While some of the mechanical behavior of the tested cerebral blood vessels can be qualitatively reproduced by the considered model, it lacks the ability to accommodate the

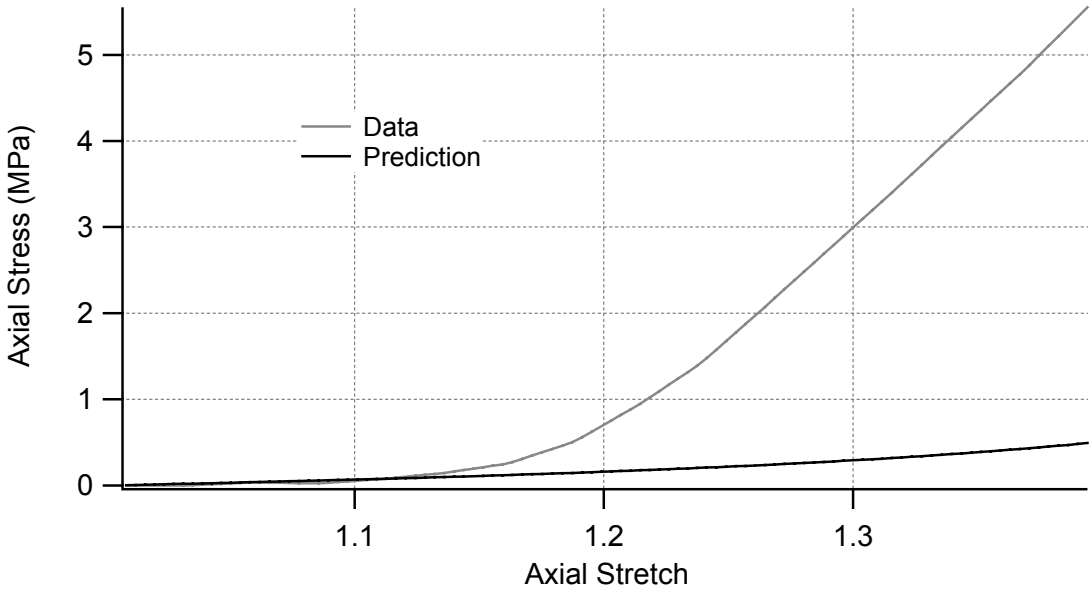

Figure 4.37 Model prediction of selected longitudinal stretch test based on coefficients determined using inflation data only

measured dramatic changes over the stretch ranges considered. Fits of individual sets of data, as shown in the discussion on uniaxial behavior, can adequately describe vessel behavior over small stretch ranges, but a single model is needed that can simulate these changes for a specimen population. More experimentation is needed to verify the behavior of these vessels in inflation, including the veins, and a suitable mathematical representation for their response needs to be defined. While it is unknown how large its effect might be, it is important to recall that the assumption of incompressibility was applied and may not be representative of this tissue at very large deformations.

5 Conclusions and Recommendations

5.1 CONCLUSIONS

1) Longitudinal stress-stretch behavior of human cerebral blood vessels generally consists of an exponentially-shaped toe region at low stresses, followed by a slightly nonlinear increase in stress until yield, where the slope of the curve begins to decrease until the ultimate point.
2) Human cortical arteries display significantly different mechanical behavior than cortical veins. Arteries are stiffer than veins and carry approximately twice as much stress at half the amount of stretch at failure.
3) Blood vessels resected during surgery and tested within a few hours display different mechanical properties than those obtained through autopsy, at least for autopsies conducted more than a day after death. Fresh vessels display higher maximum slopes and yield and ultimate stresses than those from autopsy.
4) The influence of strain rate over a range of more than three orders of magnitude has little significance on the mechanical, including failure, properties of human cerebral arteries and veins. Dynamic test results may be altered by load cell excitation, leading to erroneous conclusions regarding rate dependence.
5) Cortical arteries fail in inflation at approximately ten times healthy physiological pressure levels.
6) Human cortical arteries appear to be stiffer in the longitudinal direction than they are circumferentially. They withstand significantly greater stretch in the circumferential direction than they do longitudinally.

7) The extent of pre-stretch on the longitudinal and circumferential mechanical properties of human cerebral blood vessels is significant and seems to affect a vessel differently for different directions of loading. At low stress levels, the phenomenon appears to change a vessel's elastin structure, resulting in longer toe regions, if the elastin is not damaged, or a change in reference length if it is. Larger extents of preconditioning appear to recruit collagen fibers and reorganize them to more effectively withstand larger loads.
8) The uniaxial stress-stretch response of human cerebral blood vessels can be reasonably modeled on an individual test basis using an exponential form, so long as it is not necessary to fit the full range of stretch, from the reference to failure. The widely used biaxial form of the Fung-type strain energy relation appears to be inadequate for the modeling of combined inflation and axial stretch in cortical arteries, at least over the large range between the reference and the burst point.

5.2 RECOMMENDATIONS

1) In order to further clarify differences in the mechanical properties of human cerebral vessels, more quasi-static and dynamic axial stretch tests should be conducted on vessels obtained through autopsy. Larger vessels available through this source should also be investigated to help determine the effect of size. Tests on vessels from autopsy should be designed to study the effect of time after death. More inflation tests on both arteries and veins from surgery and autopsy are necessary to confidently define the behavior of these vessels under multi-axial loading conditions.
2) Among the many variables of interest, the extent and method of preconditioning should be further investigated in order to quantify its effect on both sub-failure and

failure properties of blood vessels. Recommendations should be made for standardization.

3) More advanced methods for the measurement of vessel dimensions during additional inflation tests should be a priority. The validity of the assumption of incompressibility in blood vessels at large deformations should also be investigated.
4) As the differences manifested between vessels are likely a result of structural differences, vessel microstructure needs to be further defined and correlated with the collected data. Studies of microstructure should also include more accurate methods for measuring the reference dimensions of blood vessels, such as histology techniques that preserve tissue morphology (Hart *et al*, 1983).
5) More advanced mathematical models that are capable of describing large deformations under multi-axial loading conditions are needed. Efforts should continue to attempt to incorporate tissue microstructure.

References

Abe, H., Hayashi, K., Sato, M. (Eds.), 1996. *Data Book of Mechanical Properties of Living Cells, Tissues and Organs*. Tokyo, New York, Springer.

Adams, J. Hume, 1990. Brain damage in fatal non-missile head injury in man. In: Braakman, R. (Ed.), *Handbook of Clinical Neurology, Vol. 13 (57): Head Injury*. Elsevier Science Publishers B.V., pp. 43-63.

Bandak, F. A., Eppinger, R. H., 1994. A three-dimensional finite element analysis of the human brain under combined rotational and translational accelerations. In *Proceedings 38th STAPP Car Crash Conference*, Society of Automotive Engineers. SAE 942215.

Boock, R. J. (1991), *Vascular Response to Mechanical Deformations.* PhD Dissertation, Department of Bioengineering, University of Pennsylvania.

Brossollet, L. J., Vito, R. P., 1995. An alternate formulation of blood vessel mechanics and the meaning of the *in vivo* property. *Journal of Biomechanics* 28(6): 679-687.

Brossollet, L. J., Vito, R. P., 1997. The effects of cryopreservation on the biaxial mechanical properties of canine saphenous veins. *Journal of Biomechanical Engineering* 119: 1-5.

Brunette, H. (1988), *Propellant-driven Projectile Embedment in Rock*. M.S. Thesis, Department of Mechanical Engineering, University of California, Berkeley.

Busby, D. E., Burton, A. C., 1965. The effect of age on the elasticity of the major brain arteries. *Canadian Journal of Physiology and Pharmacology* 43: 185-202.

Carew, T. E., Vaishnav, R. N., Patel, D. J., 1968. Compressibility of the arterial wall. *Circulation Research* 23(1): 61-68.

CDC, Analysis by the CDC National Center for Injury Prevention and Control, using data obtained from state health departments in Alaska, Arizona, California (reporting Sacramento County only), Colorado, Louisiana, Maryland, Missouri, New York, Oklahoma, Rhode Island, South Carolina, and Utah. Methods are described in:

- Centers for Disease Control and Prevention, 1997. Traumatic Brain Injury -- Colorado, Missouri, Oklahoma, and Utah, 1990-1993. *Morbidity and Mortality Weekly Report* 46(1):8-11.
- Thurman, D. J., Sniezek, J. E., Johnson, D., Greenspan, A., Smith, S. M., 1995. Guidelines for Surveillance of Central Nervous System Injury. Atlanta: Centers for Disease Control and Prevention.

Chalupnik, J. D., Daly, C. H., Merchant, H. C., 1971. *Material Properties of Cerebral Blood Vessels*. Final Report on Contract No. NIH-69-2232, Report No. ME 71-11, University of Washington, Seattle.

Chuong, C. J., Fung, Y. C., 1986. On residual stresses in arteries. *Journal of Biomechanical Engineering* 108(2):189-192.

Collins, R., Hu, W. C. L., 1972. Dynamic deformation experiments on aortic tissue. *Journal of Biomechanics* 5: 333-337.

Diamond, M. C., Scheibel, A. B., Elson, L. M., 1985. *The Human Brain Coloring Book*. New York, Barnes & Noble.

Diamond, M. C., 2001. From class notes: Integrative Biology 245 – Functional Neuroanatomy. Spring 2001, University of California, Berkeley.

Deaver, J. B., 1900-1904. *Surgical Anatomy : A Treatise on Human Anatomy in its Application to the Practice of Medicine and Surgery*. Philadelphia: Blakiston's, Vol. I.

Dobrin, P. B., 1978. Mechanical properties of arteries. *Physiological Reviews* 58(2): 397-460.

Donovan, D. L., Schmidt, S. P., Townshend, S. P., Njus, G. O., Sharp, W. V., 1990. Material and structural characterization of human saphenous vein. *Journal of Vascular Surgery* 12(5): 531-537.

Finlay, H. M., McCullough, L.; Canham, P. B., 1995. Three-dimensional collagen organization of human brain arteries at different transmural pressures. *Journal of Vascular Research* 32(5): 301-312.

Fung, Y. C., Fronek, K., Patitucci, P., 1979. Pseudoelasticity of arteries and the choice of its mathematical expression. *American Journal of Physiology* 237(5): H620-H631.

Gadd, C. W., 1966. Use of weighted-impulse criterion for estimating injury hazard. Society of Automotive Engineers 660793.

Gean, A. D., 1994. *Imaging of Head Trauma*. New York, Raven Press.

Gennarelli, T. A., Ommaya, A. K., Thibault, L. E., 1971. Comparison of translational and rotational head motions in experimental cerebral concussion. In *Proceedings 15th Stapp Car Crash Conference*. New York, Society of Automotive Engineers, pp. 797-803.

Gennarelli, T. A., Thibault, L. E., 1982. Biomechanics of acute subdural hematoma. *Journal of Trauma* 22(8): 680-686.

Goldsmith, W., 1966. The Physical Processes Producing Head Injuries. In Caveness, W. F., Walker, A. E. (Eds.), *Head Injury: Conference Proceedings*. J. B. Lippincott, pp. 350-382.

Goldsmith, W., 2002. On the state of head injury biomechanics: past, present, and future; part 1. For publication in Critical Reviews of Bioengineering, 2002.

Groenink, M., Langerak, S. E., Vanbavel, E., van der Wall, E. E., Mulder, B. J., van der Wal, A. C., Spaan, J. A., 1999. The influence of aging and aortic stiffness on permanent dilation and breaking stress of the thoracic descending aorta. *Cardiovascular Research* 43(2): 471-480.

Gurdjian, E. S., Lissner, H. R., Patrick, L. M., 1962. Protection of the head and neck in sports. *Journal of the American Medical Association* 182: 509-512.

Gurdjian, E. S., 1975. *Impact Head Injury*. Springfield, IL, C. C. Thomas.

Hart, M. N., Hansen, K. E., Sadoshima, S., Heistad, D. D., 1983. Freeze substitution as a means of preserving meningeal vessel morphology. *Brain Research* 260(1): 178-80.

Hayashi, K., Nagasawa, S., Naruo, Y., Okumura, A., Moritake, K., Handa, H., 1980. Mechanical properties of human cerebral arteries. *Biorheology* 17(3): 211-218.

Hayashi, K., Washizu, T., Tsushima, N., Kiraly, R. J., Nose, Y, 1981. Mechanical properties of aortas and pulmonary arteries of calves implanted with cardiac prostheses. *Journal of Biomechanics* 14(3):173-182.

Hayashi, K., 1993. Experimental approaches on measuring the mechanical properties and constitutive laws of arterial walls. *Journal of Biomechanical Engineering* 115(4B): 481-488.

Holbourn, A. H. S., 1943. Mechanics of head injuries. *The Lancet* 2: 438-441.

Holbourn, A. H. S., 1945. The mechanics of brain injuries. *British Medical Bulletin* 3: 147-149.

Holzapfel, G. A., Gasser, T. C., Ogden, R. W., 2000. A new constitutive framework for arterial wall mechanics and a comparative study of material models. *Journal of Elasticity* 61(1/3): 1-48.

Huang, H. M., Lee, M. C., Chiu, W. T., Chen, C. T., Lee, S. Y., 1999. Three-dimensional finite element analysis of subdural hematoma. *Journal of Trauma* 47(3): 538-544.

Hudetz, A. G., Márk, G., Kovách, A. G., Kerényi, T., Fody, L., Monos, E., 1981. Biomechanical properties of normal and fibrosclerotic human cerebral arteries. *Atherosclerosis* 39(3):353-365.

Humphrey, J. D., 1995. Mechanics of the arterial wall: review and directions. *Critical Reviews in Biomedical Engineering* 23(1-2): 1-162.

Humphrey, J. D., 1999. An evaluation of pseudoelastic descriptors used in arterial mechanics. *Journal of Biomechanical Engineering* 121(2): 259-262.

Ivarsson, J., Viano D. C., Lövsund, P., Aldman, B., 2000. Strain relief from the cerebral ventricles during head impact: experimental studies on natural protection of the brain. *Journal of Biomechanics* 33: 181-189.

Klisch, S. M., Lotz, J. C., 1999. Application of a fiber-reinforced continuum theory to multiple deformations of the annulus fibrosus. *Journal of Biomechanics* 32: 1027-1036.

Lee, M. C., Haut, R. C., 1985. Strain rate effects on tensile failure properties of the human parasagittal bridging vein and the common carotid artery and jugular veins of ferrets. In Langrana, N. A. (Ed.), *Advances in Bioengineering*. New York, American Society of Mechanical Engineers, pp. 111-112.

Lee, M. C., Haut, R. C., 1989. Insensitivity of tensile failure properties of human bridging veins to strain rate: implications in biomechanics of subdural hematoma. *Journal of Biomechanics* 22: 537-542.

Lissner, H. R., Lebow, M., Evans, F. G., 1960. Experimental studies of the relation between acceleration and intracranial pressure changes in man. *Surgery, Gynecology and Obstetrics* 111: 329-338.

Löwenhielm, P., 1974. Dynamic properties of the parasagittal bridging veins. *Z. Rechtsmedizin* 74: 55-62.

Löwenhielm, P., 1978. Dynamic strain tolerance of blood vessels at different post-mortem conditions. *Journal of Bioengineering* 2: 509-515.

Marina, A. A. (1989), *On the Dynamic Loading of Cerebral Blood Vessels*. M.S. Project Report, Department of Mechanical Engineering, University of California, Berkeley.

McMinn, R. M. H., 1977. *Color Atlas of Human Anatomy*. Ed. by R. M. H. McMinn, R. T. Hutchings. Chicago, Year Book Medical Publishers.

Melvin, J. W., Lighthall, J. W., Ueno, K., 1993. Brain injury biomechanics, In: Nahum, A. M., Melvin, J. W. (eds.), *Accidental Injury*. New York, Springer-Verlag, pp. 268-291.

Mohan, D., Melvin, J. W., 1982. Failure properties of passive human aortic tissue, I-uniaxial tension tests. *Journal of Biomechanics* 15: 887-902.

Mohan, D., Melvin, J. W., 1983. Failure properties of passive human aortic tissue, II-biaxial tension tests. *Journal of Biomechanics* 16: 31-44.

Nagasawa, S., Handa, H., Okumura, A., Naruo, Y., Moritake, K., Hayashi, K., 1979. Mechanical properties of human cerebral arteries. Part 1: Effects of age and vascular smooth muscle activation. *Surgical Neurology* 12(4):297-304.

Netter, F. H., 1997. *Atlas of Human Anatomy*. East Hanover, New Jersey, Novartis.

Ommaya, A. K., Yarnell, P., Hirsch, A. E., Harris, E. H., 1967. Scaling of experimental data on cerebral concussion in sub-human primates to concussion threshold for man. In *Proceedings 11th Stapp Car Crash Conference*, Society of Automotive Engineers, pp. 47-52. SAE 670906.

Ommaya, A. K., 1968. Mechanical properties of the tissues of the nervous system. *Journal of Biomechanics* 1: 127-138.

Ommaya, A. K., Fass, F., Yarnell P., 1968. Whiplash injury and brain damage: an experimental study. *Journal of the American Medical Association* 204: 285-289.

Ommaya, A. K., Corrao, P., 1969. Pathologic biomechanics of the central nervous system injury in head impact and whiplash trauma. In: Brinhous, K. (Ed.), *Proceedings of the International Conference of Accident Pathology*, Washington, D. C., Government Printing Press.

Ommaya, A. K., Hirsch, A. E., 1971. Tolerances for cerebral concussion from head impact and whiplash in primates. *Journal of Biomechanics* 4(1):13-21.

Omori, K., Zhang, L., Yang, K. H., King, A. I., 2000. Effect of cerebral vasculatures on the mechanical response of brain tissue: a preliminary study. In: Mahmood, H. F., Barbat, S. D., Baccouche, M. R. (Eds.), *Crashworthiness, Occupant Protection, and Biomechanics in Transportation Systems ASME 2000*, American Society of Mechanical Engineers, AMD v. 246 / BED v. 49: 167-174.

Ono, K., Kikuchi, A., Nakamura, M., Kobayashi, H., Nakamura, H., 1980. Human head tolerance to sagittal impact reliable estimation deduced from experimental head injury using sub-human primates and human cadaver skulls. In: *Proceedings 24th Stapp Car Crash Conference*, Society of Automotive Engineers. SAE 801303.

Patel, D. J., Fry, D. L., 1969. The elastic symmetry of arterial segments in dogs. *Circulation Research* 24(1): 1-8.

Roach, M. R., Burton, A. C., 1957. The reason for the shape of the distensibility curve of arteries. *Canadian Journal of Biochemistry and Physiology* 35: 681-690.

Roy, C. S., 1880. The elastic properties of the arterial wall. *Journal of Physiology (London)* 3: 123-159.

Sato, M., Niimi, H., Okumura, A., Handa, H., Hayashi, K., Moritake, K., 1979. Axial mechanical properties of arterial walls and their anisotropy. *Medical & Biological Engineering & Computing* 17: 170-176.

Schatzmann, L., Brunner, P., Staubli, H. U., 1998. Effect of cyclic preconditioning on the tensile properties of human quadriceps tendons and patellar ligaments. *Knee Surgery, Sports Traumatology, Arthroscopy* 6 [Suppl 1]: S56-61.

Scott, S., Ferguson, G. G., Roach, M. R., 1972. Comparison of the elastic properties of human intracranial arteries and aneurysms. *Canadian Journal of Physiology and Pharmacology* 50(4):328-332.

Shreiber, D. I., Bain, A. C., Meaney, D. F., 1997. In vivo thresholds for mechanical injury to the blood-brain barrier. In *Proceedings 41st Car Crash Conference*, Society of Automotive Engineers. SAE 973335.

Shreiber, D. I., Bain, A. C., Ross, D. T., Smith, D. H., Gennarelli, T. A., McIntosh, T. K, Meaney, D. F., 1999. Experimental investigation of cerebral contusion: histopathological and immunohistochemical evaluation of dynamic cortical deformation. *Journal of Neuropathology and Experimental Neurology* 58(2): 153-164.

Smith, R. W., 1979. The Response of Unembalmed Cadaveric and Living Cerebral Vessels to Graded Injury – A Pilot Study. In *Proceedings of the 23rd Stapp Car Crash Conference*, Society of Automotive Engineers, pp. 545-560. SAE 791021.

Sobotta, J., 1927-1928. *Atlas of Human Anatomy*. Ed. from the 6th German edition by J. Playfair McMurrich. New York, G. E. Stechert & Co., Vol. III.

Stalnaker, R. L., Melvin, J. W., Nusholtz, G. S., Alem, N. M., Benson, J., 1977. Head impact response. *Proceedings 21st STAPP Car Crash Conference*, SAE 770921.

Stehbens, W. E., 1972. *Pathology of the Cerebral Blood Vessels*. Saint Louis, C. V. Mosby.

Steiger, H. J., Aaslid, R., Keller, S., Reulen, H. J., 1989. Strength, elasticity and viscoelastic properties of cerebral aneurysms. *Heart and Vessels* 5(1):41-46.

Tanaka, T. T., Fung, Y. C. 1974. Elastic and inelastic properties of the canine aorta and their variation along the aortic tree. *Journal of Biomechanics* 7(4):357-370.

Thurman, D. J., Alverson, C., Dunn, K. A., Guerrero, J., Sniezek, J. E., 1999. Traumatic brain injury in the United States: A public health perspective. *Journal of Head Trauma Rehabilitation* 14(6): 602-15.

Vaishnav, R. N., Vossoughi, J., 1987. Residual stress and strain in aortic segments. *Journal of Biomechanics* 20(3):235-239.

Versace, J., 1971. A review of the severity index. Society of Automotive Engineers 710881.

Vossoughi, J., Bandak, F. A., 1996. Mechanical characteristics of vascular tissue and their role in brain injury modeling: a review. In: Bandak, F. A., Eppinger, R, H., Ommaya, A. K. (Eds.), *Traumatic Brain Injury: Bioscience and Mechanics*. Mary Ann Liebert, Inc, pp. 207-215.

Ward, C., Nahum, A. M., Smith, R., 1977. Intracranial pressure dynamics during head impact. *Proceedings 21st STAPP Car Crash Conference*, pp. 339-366, SAE 770922.

Woerdeman, M. W., 1950. *Atlas of Human Anatomy, Descriptive and Regional*. Baltimore, Williams and Wilkins Co., Vol. II.

Yamada, H., 1970. *Strength of Biological Materials*. Evans, F. G. (Ed.), Baltimore, Williams and Wilkins.

Zhou, J., Fung, Y. C., 1997. The degree of nonlinearity and anisotropy of blood vessel elasticity. *Proceedings of the National Academy of Sciences of the United States of America* 94: 14255-142.

A Histology

A.1 TISSUE PROCESSOR PROCEDURE

Table A.1 BTRC (Brain Tissue Research Center) Tissue Processor Procedure

Step	Solution	Time (minutes)	Temp (deg C)
1	70% Ethyl Alcohol	600	OFF
2	70% Ethyl Alcohol	45	OFF
3	95% Ethyl Alcohol	45	OFF
4	95% Ethyl Alcohol	45	OFF
5	100% Ethyl Alcohol	30	OFF
6	100% Ethyl Alcohol	45	OFF
7	100% Ethyl Alcohol	45	OFF
8	Xylene	60	OFF
9	Xylene	60	OFF
10	Xylene	30	OFF
11	Paraffin	60	56
12	Paraffin	60	56

A.2 SELECTED HISTOLOGICAL IMAGES

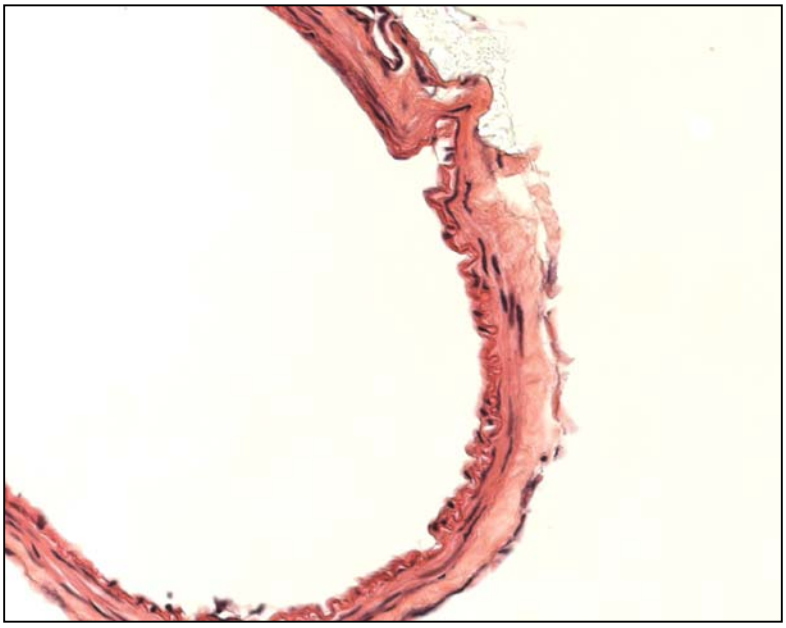

Figure A.1 Cortical artery section with H&E stain

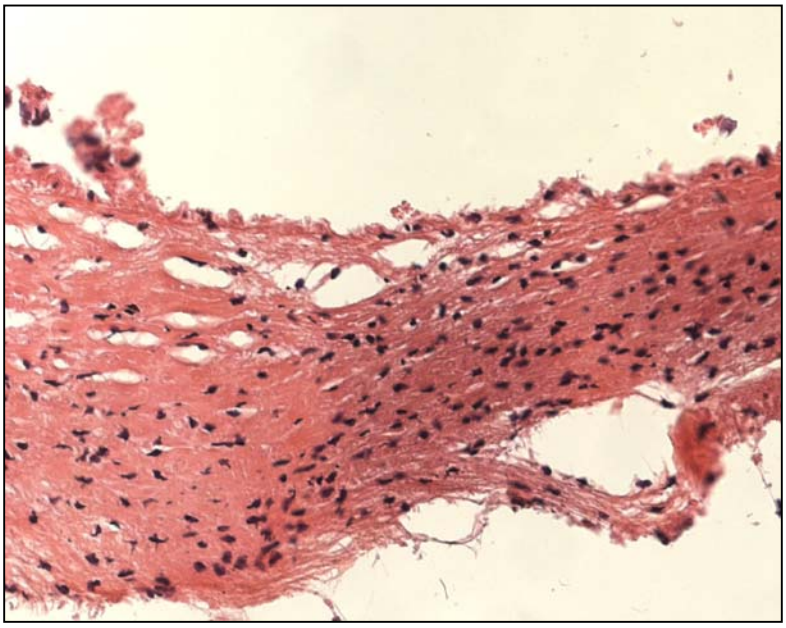

Figure A.2 Cortical vein section with H&E stain

B Dynamic Modeling

B.1 EQUATIONS

B.1.1 Blood Vessel Spring Load Response Equations

B.1.1.1 Region 1: Exponential

$$F_1 = \frac{B}{A}(e^{A(x_2 - x_1)} - 1) \tag{B.1}$$

where F_1 is the load, A and B are constants, and x_1 and x_2 are as defined in Equation 3.3.

B.1.1.2 Region2: Linear

$$F_2 = k_2(x_2 - x_1) + \overline{F} \tag{B.2}$$

where k_2 is linear stiffness and $\overline{F}$ is the required offset load

B.1.1.3 Region3: Quadratic

$$F_3 = P(x_2 - x_1)^2 + Q(x_2 - x_1) + R \tag{B.3}$$

where P, Q, and R are constants

B.1.2 Transition Constraints

B.1.1.4 Transition 1: Exponential to Linear

- Point Continuity: Require $F_1(y) = F_2(y)$ for some chosen $y \in \{x_2 - x_1\}$.

  This requirement gives $\frac{B}{A}(e^{Ay} - 1) = k_2 y + \overline{F}$ (B.4)

- Slope Continuity: Require $\frac{dF_1}{d(x_2 - x_1)}(y) = \frac{dF_2}{d(x_2 - x_1)}(y)$

  so that $k_2 = Be^{Ay}$ (B.5)

  Combining Equations B.4 and B.5 then gives

$$\overline{F} = \frac{B}{A}(e^{Ay} - 1) - k_2 y \tag{B.6}$$

Transition 2: Linear to Quadratic

- Point Continuity: Require $F_2(y') = F_3(y')$ for some chosen $y' \in \{x_2 - x_1\}$.

  This requirement gives $k_2 y' + \overline{F} = Py'^2 + Qy' + R$ (B.7)

- Slope Continuity: Require $\frac{dF_2}{d(x_2 - x_1)}(y') = \frac{dF_3}{d(x_2 - x_1)}(y')$

  so that $Q = k_2 - 2Py'$ (B.8)

  Then from Equations B.7 and B.8

  $$R = k_2 y' + \overline{F} - Py'^2 - Qy' \quad \text{(B.9)}$$

Thus, all constants are defined when A, B, and P are chosen, along with the times associated with y and y'.

B.2 PROGRAM M-FILES FOR USE IN MATLAB

B.2.1 Main m-file

```
% simDyn.m by Ken Monson      10/01
%
% Clear out workspace.
clear

% Constants.
global k1;
global k2;
global F;
global P;
global Q;
global R;
global m;
global A;
global B;
global tdl;
global gripXSt;

% Parameters.
      % Blood Vessel
A = 4500;                % vessel load-disp behavior: B/A*(exp(A*(xGrip-
xLc))-1)
B = 26;
P = -17          *1000; % Quadratic portion squared term coeff. Px^2 +
Qx + R
CsA = 0.558;                          % (mm^2) vessel cross-sectional area
xRef = 5.58       /1000;      % (mm) reference length of vessel
      % Load Cell
```

```
k1 = 109948.82;      % N/m (2.5 cell: 109948.82; 10 cell: 437795.28)
m = 0.0174;          % kg -- with grip (2.5: 0.0174; 10: 0.0278 [upside
down])
      % Simulation
tTrans = .0065;      % time for transition from exp to linear spring for
vessel
tYield = .0085;         % time for yield
tFail = .0087;

% Load appropriate time(s)-disp(m)-load(N) file
load tdl.txt;
gripXSt = tdl(1, 2);

% Find out size of t.
nrows = size(tdl,1);
tStart = tdl(1,1);
tEnd = tdl(nrows,1);           % end time
tSpan = [tStart tEnd];

% Initial conditions.
y0 = [0 0];

% Integrate from tStart to tTrans (exponential portion).
options = odeset('refine',5);
[t,y] = ode45('dynODEExp', tSpan, y0, options);
%[t,y] = ode45('dynODEExp', tSpan, y0);

% Get pre-transition values.
nrows = size(y, 1);
timeFlg = 0;   % time transition flag
i = 1;
while timeFlg == 0
   if t(i) > tTrans
         timeFlg = 1;
         transIndex = i-1;          %save transition index
   else
      xGrip = linterp(tdl(:, 1), tdl(:, 2), t(i));
      xVessel(i) = xGrip-gripXSt-y(i,1);
      fVessel(i) = B/A*(exp(A*xVessel(i))-1);
      fCellAct(i) = linterp(tdl(:, 1), tdl(:, 3), t(i));
   end

   i = i + 1;
end
endVals = y(1:transIndex,:);
time = t(1:transIndex,:);

gripX = linterp(tdl(:, 1), tdl(:, 2), time(transIndex));
vessX = gripX - gripXSt - endVals(transIndex,1);
k2 = B*exp(A*vessX);
F = B/A*(exp(A*vessX)-1)-k2*vessX;

% Integrate from tTrans to tYield (linear portion).
y0 = [endVals(transIndex, 1) endVals(transIndex, 2)];
tSpan = [time(transIndex) tEnd];
[t1,y1] = ode45('dynODELin', tSpan, y0, options);
```

```
% Get linear portion values.
nrows = size(y1, 1);
timeFlg = 0;   % time transition flag
i = 1;
while timeFlg == 0
   if t1(i) > tYield
         timeFlg = 1;
         yieldIndex = i-1;          %save yield index
   else
      xGrip = linterp(tdl(:, 1), tdl(:, 2), t1(i));
      xVessel(transIndex+i) = xGrip-gripXSt-y1(i,1);
      fVessel(transIndex+i) = k2*xVessel(transIndex+i) + F;
      fCellAct(transIndex+i) = linterp(tdl(:, 1), tdl(:, 3), t1(i));
   end
   i = i + 1;
end
endVals = [endVals; y1(1:yieldIndex,:)];
time = [time; t1(1:yieldIndex,:)];

newIndex = transIndex + yieldIndex;

gripX = linterp(tdl(:, 1), tdl(:, 2), time(newIndex));
vessX = gripX - gripXSt - endVals(newIndex,1);
Q = k2 - 2*P*vessX;
R = k2*vessX + F - P*vessX^2 - Q*vessX;

% Integrate from tYield to tFail (quadratic portion).
y0 = [endVals(newIndex, 1) endVals(newIndex, 2)];
tSpan = [time(newIndex) tEnd];
[t2,y2] = ode45('dynODEQuad', tSpan, y0, options);

% Get quadratic portion values.
nrows = size(y2, 1);
timeFlg = 0;   % time transition flag
i = 1;
while timeFlg == 0
   if t2(i) > tFail
         timeFlg = 1;
         failIndex = i-1;           %save transition index
   else
      xGrip = linterp(tdl(:, 1), tdl(:, 2), t2(i));
      xVessel(newIndex+i) = xGrip-gripXSt-y2(i,1);
      fVessel(newIndex+i) = P*(xVessel(newIndex+i))^2 +
Q*xVessel(newIndex+i)+R;
      fCellAct(newIndex+i) = linterp(tdl(:, 1), tdl(:, 3), t2(i));
   end
   i = i + 1;
end
endVals = [endVals; y2(1:failIndex,:)];
time = [time; t2(1:failIndex,:)];

newIndex = newIndex + failIndex;

% Integrate from tFail to tEnd (failed portion).
y0 = [endVals(newIndex, 1) endVals(newIndex, 2)];
tSpan = [time(newIndex) tEnd];
[t3,y3] = ode45('dynODEFree', tSpan, y0, options);
```

```
endVals = [endVals; y3];
time = [time; t3];

% Get failed portion values.
nrows = size(y3, 1);
timeFlg = 0;   % time transition flag
i = 1;
for i=1:nrows,
   xVessel(newIndex+i) = xGrip-gripXSt-y3(i,1);
   fVessel(newIndex+i) = 0;
   fCellAct(newIndex+i) = linterp(tdl(:, 1), tdl(:, 3), t3(i));
end

% Calculate load cell values
fCell = k1*endVals(:,1);

mrows = size(endVals, 1);
for i=1:mrows,
   sigV(i) = fVessel(i) / CsA;
   lamV(i) = (xVessel(i) + xRef) / xRef;
end

% Plot
figure(1);
subplot(1,2,1);
plot(time, fCell, 'r', time, fCellAct, 'b', time, fVessel, ':');
grid;
xlabel('Time (sec)');
ylabel('Load (N)');
legend('Calculated Load','Measured Load', 'Calc. Vessel', 2);

subplot(1,2,2);
plot(xVessel*1000, fCell,'r',xVessel*1000,
fCellAct,'b',xVessel*1000,fVessel,':');
grid;
xlabel('Disp (mm)');
ylabel('Load (N)');
legend('Calculated Load','Measured Load', 'Calc. Vessel', 2);

figure(2);
plot(lamV, sigV);
grid;
xlabel('Stretch');
ylabel('Stress (MPa)');

% Print output information.

fPtr = fopen('out.dat', 'w');
nrows = size(fVessel, 2);
i = 1;
fprintf(fPtr, '   Time (s)   Stretch   Stress (MPa)  LC Stress
(MPa)\n');
for i=1:nrows,
   cellStress = fCell(i) / CsA;
   fprintf(fPtr, '%10.6f %10.4f  %10.4f  %10.4f\n', time(i), lamV(i),
sigV(i), cellStress);
```

```
end
fclose(fPtr);
```

B.2.2 Auxiliary m-files

```
% dynODE.m by Ken Monson      10/01
%
% This function computes the derivatives of the
% load cell dynamic data ODE for exponential portion.
%
% function definition:
%
% function [derivs] = dynODEExp(t, states)
%    where t is time vector, states
%    is given state vector, derivs
%    is derivative of state vector

function [derivs] = dynODEExp(t, states)

global k1;
global k2;
global F;
global P;
global Q;
global R;
global m;
global A;
global B;
global tdl;
global gripXSt;

% Constants.

% Parameters.

% Convert input vector quantities to state variables
% (for readability - not necessary).
x1 = states(1);
x2 = states(2);

% Compute actuator position for present time.
gripX = linterp(tdl(:, 1), tdl(:, 2), t);

% Compute output derivatives.
x1Dot = x2;
x2Dot = -k1/m*x1 + B/A/m*(exp(A*(gripX-gripXSt-x1))-1);

% Convert derivative values to output vector quantities.
derivs = [x1Dot; x2Dot];
```

```
% dynODE.m by Ken Monson      10/01
%
% This function computes the derivatives of the
% load cell dynamic data ODE for linear portion.
```

```
%
% function definition:
%
% function [derivs] = dynODELin(t, states)
%    where t is time vector, states
%    is given state vector, derivs
%    is derivative of state vector

function [derivs] = dynODELin(t, states)

global k1;
global k2;
global F;
global P;
global Q;
global R;
global m;
global A;
global B;
global tdl;
global gripXSt;

% Constants.

% Parameters.

% Convert input vector quantities to state variables
% (for readability - not necessary).
x1 = states(1);
x2 = states(2);

% Compute actuator position for present time.
gripX = linterp(tdl(:, 1), tdl(:, 2), t);

% Compute output derivatives.
x1Dot = x2;
x2Dot = 1/m*(k2*(gripX-gripXSt-x1) + F - k1*x1);

% Convert derivative values to output vector quantities.
derivs = [x1Dot; x2Dot];
```

```
% dynODEQuad.m by Ken Monson  10/01
%
% This function computes the derivatives of the
% load cell dynamic data ODE for quadratic portion.
%
% function definition:
%
% function [derivs] = dynODEQuad(t, states)
%    where t is time vector, states
%    is given state vector, derivs
%    is derivative of state vector

function [derivs] = dynODEQuad(t, states)

global k1;
global k2;
```

```
global F;
global P;
global Q;
global R;
global m;
global A;
global B;
global tdl;
global gripXSt;

% Constants.

% Parameters.

% Convert input vector quantities to state variables
% (for readability - not necessary).
x1 = states(1);
x2 = states(2);

% Compute actuator position for present time.
gripX = linterp(tdl(:, 1), tdl(:, 2), t);

% Compute output derivatives.
x1Dot = x2;
xVess = gripX-gripXSt-x1;
x2Dot = 1/m*(P*xVess^2 + Q*xVess + R - k1*x1);

% Convert derivative values to output vector quantities.
derivs = [x1Dot; x2Dot];
```

```
% dynODEFree.m by Ken Monson  10/01
%
% This function computes the derivatives of the
% load cell dynamic data ODE for failed portion.
%
% function definition:
%
% function [derivs] = dynODEFree(t, states)
%    where t is time vector, states
%    is given state vector, derivs
%    is derivative of state vector

function [derivs] = dynODEFree(t, states)

global k1;
global k2;
global F;
global P;
global Q;
global R;
global m;
global A;
global B;
global tdl;
global gripXSt;

% Constants.
```

```
% Parameters.

% Convert input vector quantities to state variables
% (for readability - not necessary).
x1 = states(1);
x2 = states(2);

% Compute output derivatives.
x1Dot = x2;
x2Dot = -k1/m*x1;

% Convert derivative values to output vector quantities.
derivs = [x1Dot; x2Dot];
```

B.3 PLOTS OF SELECTED DYNAMIC MODELING CASES

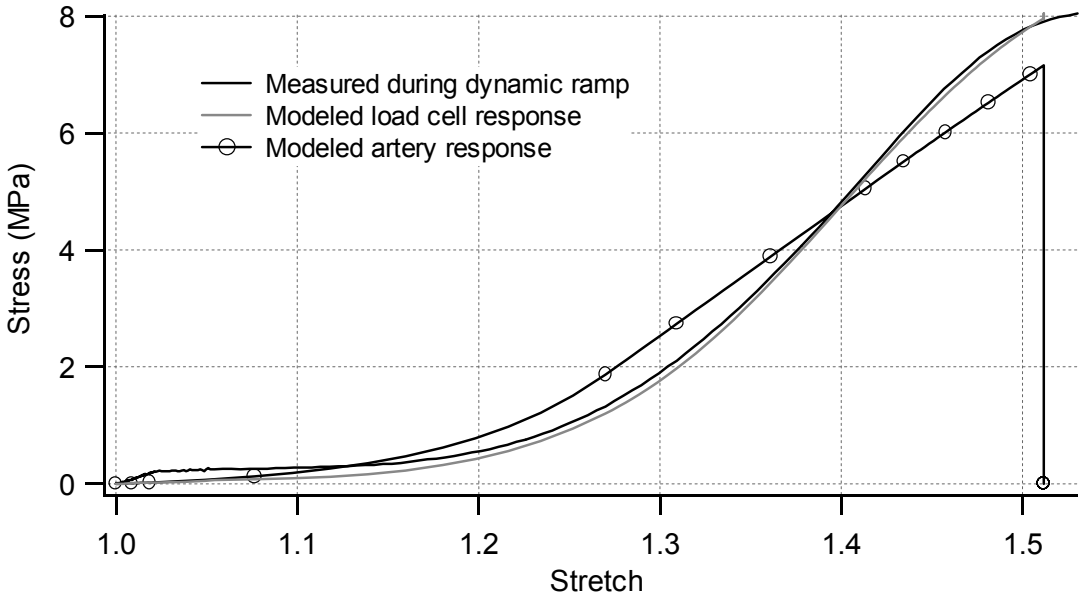

Figure B.1 Dynamic Modeling Results – Selected Case One: Artery resected from surgery

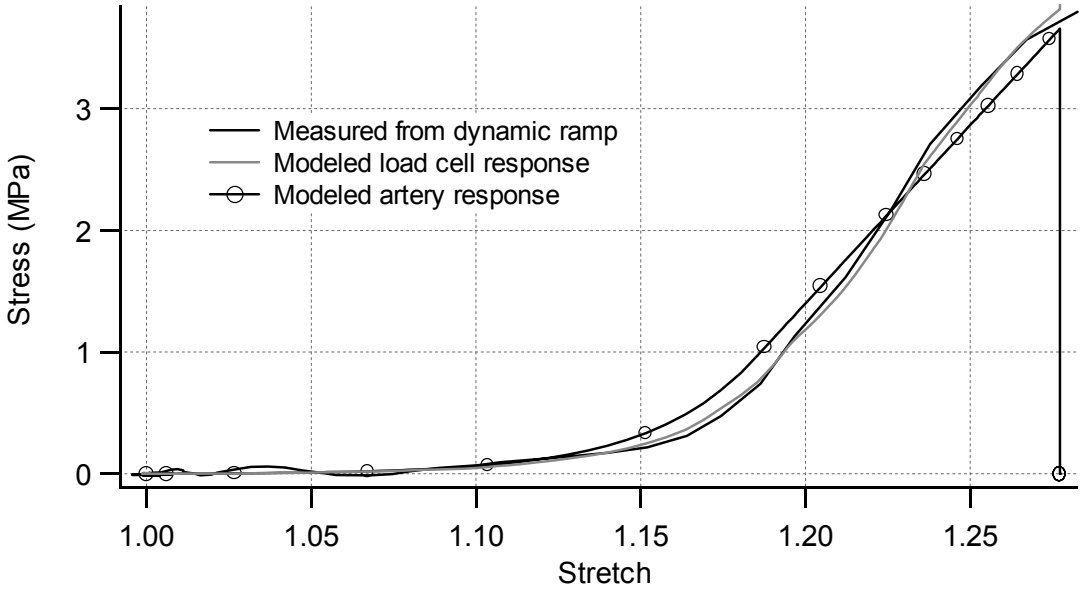

Figure B.2 Dynamic Modeling Results – Selected Case Two: Artery resected in autopsy

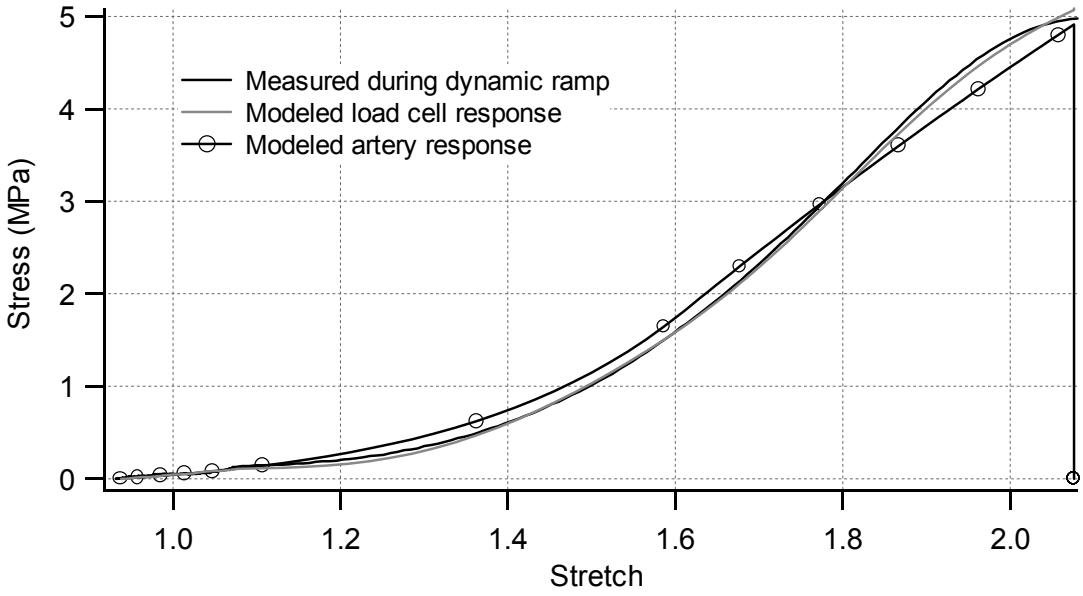

Figure B.3 Dynamic Modeling Results – Selected Case Three: Vein resected in surgery

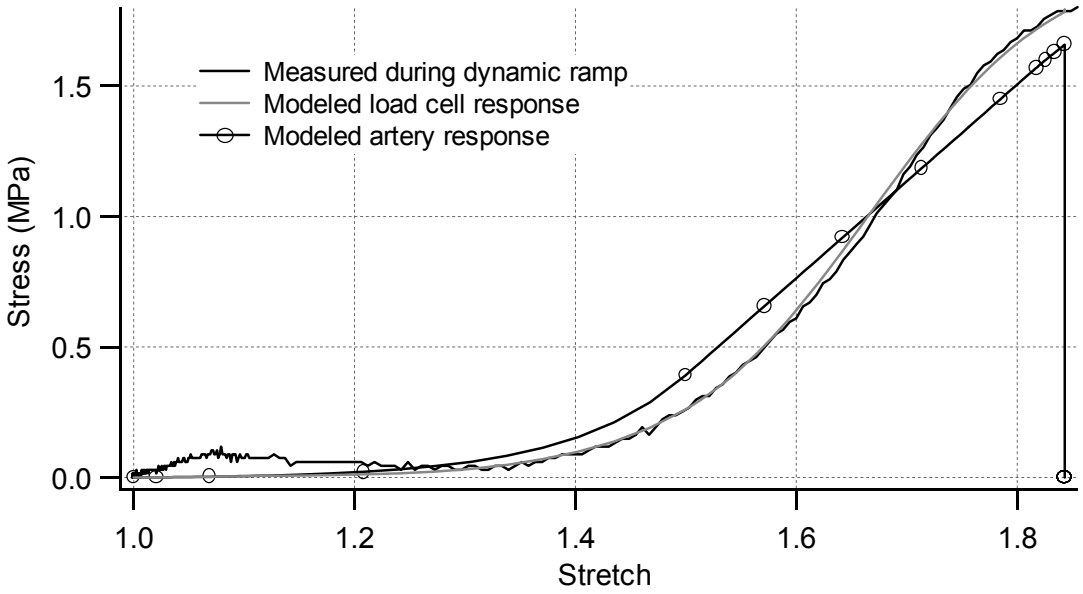

Figure B.4 Dynamic Modeling Results – Selected Case Four: Vein resected in surgery

C Vessel Data

Vessel data from axial stretch tests are organized in landscape format on the following pages by vessel type (artery or vein), vessel source (surgery or autopsy), and test type (quasi-static or dynamic). Dynamic data are followed by results from dynamic modeling. The data are separated into blocks based on the above descriptors, and each block is summarized below by number of specimens, mean, standard deviation, maximum value, and minimum value.

Various described parameters are defined as follows:

Test	Name for specimen and test
Date	Date of test
Vessel	Type of vessel
Age	Donor age
Sex	Donor sex
Cs Area	Cross-sectional area (in mm^2)
~ OD	Approximate outer diameter (in mm)
Wall	Wall thickness (in mm)
Inv/Ex Ratio	Ratio of *in vivo* and excised lengths
Tm: d-t	Time between death and testing, autopsy cases only (in hours)
Tm: r-t	Time between resection and testing (in hours)
GageL	Reference length of specimen during test (in mm)
Pc Lam	Maximum extent of stretch during preconditioning
Toe Lam	Length of toe region
A	Constant A defined in Equation 2.1
B	Constant B defined in Equation 2.1
Max Mod	Maximum slope of stress-stretch curve, Mod_Y (in MPa)
lamY	Stretch at yield point, λ_Y
sigY	Stress at yield point, σ_Y (in MPa)
lamU	Stretch at ultimate point, λ_U
sigU	Stress at ultimate point, σ_U (in MPa)
Max Load	Maximum load obtained during test (in N)
Rate	Strain rate of test (in s^{-1})
Fail Loc	Location of failure within specimen, either at the end or in midsection. Blank cells indicate a sub-failure test.
Grips Type	Type of grips used in test, either flat clamps or needles

Table C.1 Individual Test Data for Quasi-Static Tests on Cortical Arteries, both from Surgery and Autopsy

Test	Date	Vessel	Age	Sex	Cs Area (mm^2)	~ OD (mm)	Wall (mm)	InV/Ex Ratio	Tm:d-t (hr)	Tm:r-t (hr)	GageL (mm)	Pc Lam	Toe Lam	A	B	Max Mod	lamY	sigY (MPa)	lamU	sigU (MPa)	Max Load (N)	Rate (s-1)	Fail Loc	Grips Type
Arteries-Quasi-static																								
Surgery Vessels																								
7-2-99a1-2	7/2/99	temp cort	54	M	0.249	0.58	0.12	1.40	N/A	4.25	7.80	1.26	1.24	20.41	0.230	27.68	1.39	5.55	1.39	5.55	1.38	0.26	mid	flat
10-8-99a	10/8/99	temp cort	28	M	0.158	0.49	0.11	N/A	N/A	4	4.96	1.17	1.37	11.27	0.181	17.73	1.56	3.50	1.57	3.61	0.57	0.20	mid	flat
10-15-99a	10/15/99	temp cort	25	M	0.108	0.44	0.08	2.00	N/A	4.5	3.95	1.76	1.51	9.97	0.045	11.20	1.76	3.08	1.82	3.47	0.37	0.13	end	flat
10-22-99a	10/22/99	temp cort	27	F	0.218	0.63	0.09	N/A	N/A	4	6.25	1.40	1.38	24.50	0.003	27.77	1.47	3.66	1.55	5.15	1.12	0.16	mid	flat
8-4-00a	8/4/00	temp cort	35	M	0.189	0.56	0.10	1.13	N/A	4.5	8.50	1.12	1.20	19.14	0.612	32.23	1.31	4.75	1.36	5.89	1.11	0.06	end	flat
9-8-00a1	9/8/00	temp cort	30	M	0.125	0.45	0.09	N/A	N/A	4	8.30	1.11	1.12	37.91	0.177	27.00	1.26	3.62	1.33	5.02	0.64	0.10	end	flat
9-8-00a2	9/8/00	temp cort	30	M	0.096	0.37	0.07	1.06	N/A	4.75	5.70	1.12	1.10	26.37	1.373	18.49	1.28	4.03	1.33	4.37	0.43	0.11	end	flat
5-4-01a	5/4/01	temp cort	36	M	0.340	0.85	0.14	1.29	N/A	4	1.30	1.42	1.08	55.54	0.386	-	-	-	-	-	-	0.01	-	needle
6-1-01a1	6/1/01	temp cort	30	M	0.144	0.48	0.10	1.73*	N/A	7.5	2.70	1.00	1.16	17.46	0.756	-	-	-	-	-	-	0.19	-	needle
6-1-01a2	6/1/01	temp cort	30	M	same	same	same	same	N/A	9	3.57	1.22	1.17	30.85	0.100	-	-	-	-	-	-	0.14	-	needle
		number	9		9	9	9	5	0	10	10	10	10	10	10	7	7	7	7	7	7	10		
		avg	32.8		0.181	0.54	0.10	1.38		5.05	5.30	1.26	1.23	25.34	0.39	23.16	1.43	4.03	1.48	4.72	0.80	0.14		
		stdev	8.70		0.078	0.14	0.02	0.37		1.74	2.46	0.22	0.14	13.59	0.42	7.45	0.18	0.85	0.18	0.94	0.39	0.07		
		min	25		0.096	0.37	0.07	1.06	0.00	4.00	1.30	1.00	1.08	9.97	0.00	11.20	1.26	3.08	1.33	3.47	0.37	0.01		
		max	54		0.340	0.85	0.14	2.00	0.00	9	8.50	1.76	1.51	55.54	1.37	32.23	1.76	5.55	1.82	5.89	1.38	0.26		
Autopsy Vessels																								
8-14-01-1a1	8/14/01	temp cort	59	M	0.277	0.83	0.13	N/A	40	12.75	8.74	1.11	1.11	64.68	0.011	18.57	1.27	2.82	1.29	3.10	0.86	0.05	mid	flat
8-14-01-1a21	8/14/01	temp cort	59	M	0.558	1.29	0.14	N/A	34.75	7.5	8.20	1.13	1.11	44.78	0.051	10.11	1.29	1.90	1.29	1.90	1.06	0.03	end	flat
8-14-01-1a23	8/14/01	temp cort	59	M	0.558	1.29	0.14	N/A	35.25	8	8.60	1.15	1.11	52.11	0.044	25.47	1.28	3.99	1.31	4.55	2.54	0.03	end	flat
8-14-01-1a32	8/14/01	temp cort	59	M	2.357	2.56	0.34	N/A	39.25	12	16.03	1.19	1.11	45.67	0.030	-	-	-	-	-	-	0.03	-	flat
8-14-01-1a42	8/14/01	temp cort	59	M	0.474	1.21	0.13	N/A	40.25	13	18.50	1.11	1.09	51.51	0.165	22.85	1.21	2.74	1.23	3.07	1.45	0.03	end	flat
8-14-01-2a12	8/14/01	temp cort	57	M	0.375	0.96	0.14	N/A	40	11.75	9.42	1.17	1.13	45.37	0.024	10.77	1.25	1.43	1.27	1.59	0.60	0.05	end	flat
8-23-01a2	8/23/01	temp cort	38	M	0.092	0.5	0.06	1.17	41.75	11.75	5.15	1.19	1.19	31.12	0.020	9.11	1.25	0.76	1.33	1.30	0.12	0.10	mid	flat
8-23-01a3	8/23/01	temp cort	38	M	7.250	3.74	0.59	N/A	42	12	5.88	1.23	1.16	19.87	0.078	2.00	1.39	0.51	1.42	0.54	3.92	0.08	end	flat
		number	8		8	8	8	1	8	8	8	8	8	8	8	7	7	7	7	7	7	8		
		avg	53.5		1.493	1.55	0.21	1.17	39.16	11.09	10.07	1.16	1.13	44.39	0.05	14.13	1.28	2.02	1.31	2.29	1.51	0.05		
		stdev	9.59		2.431	1.07	0.17		2.73	2.12	4.72	0.04	0.03	13.64	0.05	8.41	0.06	1.24	0.06	1.36	1.31	0.03		
		min	38		0.092	0.50	0.06	1.17	34.75	7.50	5.15	1.11	1.09	19.87	0.01	2.00	1.21	0.51	1.23	0.54	0.12	0.03		
		max	59		7.250	3.74	0.59	1.17	42.00	13.00	18.50	1.23	1.19	64.68	0.17	25.47	1.39	3.99	1.42	4.55	3.92	0.10		

Table C.2 Individual Test Data for Dynamic Tests on Cortical Arteries from Surgery, along with Dynamic Model Adjustments

Test	Date	Vessel	Age	Sex	Cs Area (mm^2)	~OD (mm)	Wall (mm)	InV/Ex Ratio	Tm:d-t (hr)	Tm:r-t (hr)	GageL (mm)	Pc Lam	Toe Lam	A	B	Max Mod	lamY	sigY (Mpa)	Max Lam	Su (Mpa)	Max Load (N)	Rate (s-1)	Fail Loc	Grips Type
Arteries-Dynamic																								
Surgery Vessels																								
2-18-00a2	2/18/00	temp cort	27	M	0.361	0.83	0.14	1.20	N/A	4	11.30	-	-	-	-	-	-	-	1.38-1.62	4.94	1.78	476	end	flat
3-24-00a	3/24/00	temp cort	21	M	0.142	0.47	0.09	1.60	N/A	3.75	7.40	~1.3	1.51	6.72	0.480	16.30	1.64	4.30	1.71	4.94	0.70	270	end	flat
5-12-00a	5/12/00	temp cort	39	F	0.104	0.41	0.07	1.32	N/A	3.25	10.00	1.30	-	-	-	20.75	1.44	3.89	1.52	4.80	0.51	259	end	flat
5-17-00a1	5/17/00	temp cort	50	F	0.158	0.56	0.08	1.35	N/A	3.5	8.70	~1.35	1.33	9.69	1.050	34.98	1.44	6.11	1.53	8.05	1.27	246	mid	flat
5-17-00a2	5/17/00	temp cort	50	F	same	same	same	same	N/A	4	9.80	~1.35	-	-	-	-	-	-	1.39	3.63	0.57	216	mid	flat
5-26-00a	5/26/00	temp cort	34	F	0.254	0.72	0.12	1.09	N/A	3.75	6.70	1.34	-	-	-	20.68	1.60	3.48	1.71	4.67	1.20	288	end	flat
6-9-00a	6/9/00	temp cort	30	F	0.145	0.52	0.11	1.06	N/A	3.75	8.00	1.40	-	-	-	-	-	-	1.60	5.06	0.74	211	end	flat
7-28-00a1	7/28/00	temp cort	36	M	0.179	0.36	0.08	1.19	N/A	4	7.80	1.18	-	-	-	14.93	1.71	4.09	1.83	4.96	0.89	294	mid	flat
7-28-00a2	7/28/00	temp cort	36	M	0.128	0.48	0.09	1.23	N/A	4.5	7.00	1.30	-	-	-	19.05	1.59	5.11	1.78	7.11	0.91	435	end	flat
		number	8		8	8	8	8		9	9	5	2	2	2	6	6	6	8	9	9	9		
		avg	34.1		0.184	0.54	0.10	1.26		3.83	8.52	1.30	1.42	8.21	0.77	21.12	1.57	4.50	1.63	5.35	0.95	299		
		stdev	8.64		0.084	0.16	0.02	0.17		0.35	1.55	0.08	0.13	2.10	0.40	7.19	0.11	0.96	0.15	1.35	0.40	93		
		min	21		0.104	0.36	0.07	1.06		3.25	6.70	1.18	1.33	6.72	0.48	14.93	1.44	3.48	1.39	3.63	0.51	211		
		max	50		0.361	0.83	0.14	1.60		4.50	11.30	1.40	1.51	9.69	1.05	34.98	1.71	6.11	1.83	8.05	1.78	476		
Dynamic Modeling																								
3-24-00a													1.39	7.40	0.573	10.42			1.69	4.42		366		
5-12-00a													-	-	-	11.60			1.49	3.95		259		
5-17-00a1													1.27	11.31	1.046	22.04			1.51	7.16		246		
5-17-00a2													1.16	10.79	2.046	11.62			1.38	3.25		215		
5-26-00a													1.36	17.29	0.018	10.86			1.71	4.28		287		
6-9-00a													not good enough data for modeling											
7-28-00a1													1.37	8.58	0.371	8.75			1.82	4.79		362		
7-28-00a2													not good enough data for modeling											
		number											5	5	5	6			6	6		6		
		avg											1.31	11.07	0.81	12.55			1.60	4.64		289		
		stdev											0.10	3.82	0.78	4.77			0.17	1.34		62		

Table C.3 Individual Test Data for Dynamic Tests on Cortical Arteries from Autopsy, along with Dynamic Model Adjustments

Test	Date	Vessel	Age	Sex	Cs Area (mm^2)	~OD (mm)	Wall (mm)	InV/Ex Ratio	Tm:d-t (hr)	Tm:r-t (hr)	GageL (mm)	Pc Lam	Toe Lam	A	B	Max Mod	lamY	sigY (MPa)	Max Lam	Su (MPa)	Max Load (N)	Rate (s-1)	Fail Loc	Grips Type
Arteries-Dynamic (cont'd.)																								
Autopsy Vessels																								
8-14-01-1a22	8/14/01	temp cort	59	M	0.558	1.29	0.14	N/A	35	7.75	5.58	1.15	1.19	40.2	0.019	51.4	1.3	6.41	1.37	8.19	4.57	74	end	flat
8-14-01-1a31	8/14/01	temp cort	59	M	2.357	2.56	0.34	N/A	39.25	12	8.92	1.12	1.18	34.1	0.063	19.9	1.3	3.17	1.38	4.40	10.37	60	end	flat
8-14-01-1a41	8/14/01	temp cort	59	M	0.474	1.21	0.13	N/A	40	12.75	20.61	1.13	1.14	34.5	0.379	42.3	1.18	2.84	1.20	3.45	1.63	28	end	flat
8-14-01-2a11	8/14/01	temp cort	57	M	0.375	0.96	0.14	N/A	30.75	11.5	9.23	1.15	1.2	34.8	0.041	38.3	1.24	2.71	1.28	3.80	1.42	54	mid	flat
8-14-01-2a2	8/14/01	temp cort	57	M	0.137	0.59	0.07	N/A	27.75	8.5	11.15	1.16	-	-	-	40.2	1.29	6.08	1.33	8.06	1.10	51	mid	flat
8-23-01a1	8/23/01	temp cort	38	M	0.210	0.76	0.1	1.21	41	11	5.40	1.23	1.32	19.61	0.061	30.61	1.38	3.52	1.46	6.03	1.27	91	end	flat
		number	6		6	6	6	1	6	6	6	6	5	5	5	6	6	6	6	6	6	6		
		avg	54.8		0.685	1.23	0.15	1.21	35.63	10.58	10.15	1.16	1.21	32.64	0.11	37.13	1.28	4.12	1.34	5.66	3.39	59		
		stdev	8.30		0.834	0.70	0.10		5.43	2.00	5.59	0.04	0.07	7.70	0.15	10.77	0.07	1.67	0.09	2.11	3.66	21		
		min	38		0.137	0.59	0.07	1.21	27.75	7.75	5.40	1.12	1.14	19.61	0.02	19.94	1.18	2.71	1.20	3.45	1.10	28		
		max	59		2.357	2.56	0.34	1.21	41.00	12.75	20.61	1.23	1.32	40.18	0.38	51.41	1.38	6.41	1.46	8.19	10.37	91		
Dynamic Modeling																								
8-14-01-1a22													1.19	34.8	0.058	43.6			1.36	8.81		69		
8-14-01-1a31													1.17	30.3	0.099	19.7			1.36	4.33		57		
8-14-01-1a41													1.12	41.2	0.261	31.3			1.20	3.40		28		
8-14-01-2a11													1.18	31.4	0.091	29.3			1.28	3.66		52		
8-14-01-2a2													1.17	32.90	0.162	43.2			1.33	8.06		51		
8-23-01a1													1.31	21.60	0.039	30.00			1.45	5.68		84		
		number											6	6	6	6			6	6		6		
		avg											1.19	32.03	0.12	32.86			1.33	5.66		57		
		stdev											0.06	6.40	0.08	9.16			0.08	2.30		19		

Table C.4 Individual Test Data for Quasi-Static Tests on Cortical Veins, both from Surgery and Autopsy

Test	Date	Vessel	Age	Sex	Cs Area (mm^2)	~OD (mm)	Wall (mm)	InV/Ex Ratio	Tm:d-t (hr)	Tm:r-t (hr)	GageL (mm)	Pc Lam	Toe Lam	A	B	Max Mod	lamY	sigY (Mpa)	Max Lam	Su (Mpa)	Max Load (N)	Rate (s-1)	Fail Loc	Grips Type
Veins-Quasi-static																								
Surgery Vessels																								
7-2-99v1-1	7/2/99	temp cort	54	M	0.160	0.46	0.10	N/A	N/A	4.75	3.85	1.50	1.58	9.17	0.022	3.31	1.69	0.84	2.13	1.16	0.19	0.13	end	flat
9-3-99v1-1	9/3/99	temp cort	27	F	0.321	0.93	0.14	1.50	N/A	4.5	13.60	1.29	1.40	7.72	0.085	2.15	1.76	0.81	2.12	1.18	0.37	0.04	mid	flat
10-1-99v	10/1/99	temp cort	23	F	0.105	0.32	0.07	1.31	N/A	N/A	4.12	1.80	1.17	12.57	0.420	4.33	1.25	0.60	2.00	1.93	0.20	0.12	mid	flat
11-5-99v	11/5/99	temp cort	19	M	0.267	0.58	0.14	1.54	N/A	4.5	5.37	1.55	1.55	9.67	0.021	6.08	1.84	2.06	1.94	2.30	0.61	0.09	mid	flat
8-4-00v1	8/4/00	temp cort	35	M	0.651	1.20	0.13	N/A	N/A	4	7.90	1.19	1.31	9.49	0.166	-	-	-	-	-	-	0.06		flat
8-25-00v1-1	8/25/00	temp cort	39	M	0.171	0.47	0.10	1.47	N/A	3.25	3.00	1.30	1.46	5.22	0.060	1.80	2.05	0.66	2.07	0.68	0.12	0.14	end	flat
8-25-00v1-2	8/25/00	temp cort	39	M	0.288	0.64	0.12	1.47	N/A	3.5	5.20	1.30	1.42	10.18	0.042	3.89	1.74	1.19	1.83	1.35	0.39	0.10	end	flat
4-6-01v	4/6/01	temp cort	14	M	0.716	1.28	0.13	1.12*	N/A	6.75	4.12	1.00	-	-	-	1.75	1.54	0.50	1.88	0.71	0.51	0.20	end	needle
4-13-01v	4/13/01	temp cort	22	M	0.819	0.93	0.22	1.8*	N/A	7.25	4.00	1.00	1.28	17.46	0.019	1.60	1.33	0.18	-	-	-			needle
		number	9		9	9	9	5		8	9	9	8	8	8	8	8	8	7	7	7	8		
		avg	30.2		0.389	0.76	0.13	1.46		4.81	5.68	1.33	1.40	10.19	0.10	3.11	1.65	0.86	2.00	1.33	0.34	0.11		
		stdev	##		0.267	0.34	0.04	0.09		1.45	3.28	0.26	0.14	3.61	0.14	1.59	0.27	0.57	0.12	0.60	0.18	0.05		
		min	14		0.105	0.32	0.07	1.31		3.25	3.00	1.00	1.17	5.22	0.02	1.60	1.25	0.18	1.83	0.68	0.12	0.04		
		max	54		0.819	1.28	0.22	1.54		7	13.60	1.80	1.58	17.46	0.42	6.08	2.05	2.06	2.13	2.30	0.61	0.20		
Autopsy Vessels																								
8-14-01-1v11	8/14/01	temp cort	59	M	0.646	1.5	0.14	N/A	35.75	8.5	10.90	1.19	1.50	8.74	0.011	0.74	1.60	0.17	2.03	0.34	0.22	0.04	end	flat
8-14-01-1v13	8/14/01	temp cort	59	M	0.646	1.5	0.14	N/A	35.75	8.5	9.67	1.38	1.31	16.80	0.009	2.20	1.50	0.30	1.86	0.57	0.37	0.05	end	flat
8-23-01v1	8/23/01	temp cort	38	M	0.519	1.28	0.14	1.45	29.33	11.33	6.80	1.23	1.17	34.55	0.002	1.74	1.55	0.52	1.70	0.73	0.38	0.07	end	flat
		number	3		3	3	3	1	3	3	3	3	3	3	3	3	3	3	3	3	3	3		
		avg	52.0		0.604	1.43	0.14	1.45	33.61	9.44	9.12	1.27	1.33	20.03	0.01	1.56	1.55	0.33	1.86	0.55	0.32	0.05		
		stdev	##		0.073	0.13	0.00		3.71	1.63	2.10	0.10	0.17	13.20	0.00	0.75	0.05	0.18	0.17	0.20	0.09	0.01		
		min	38		0.519	1.28	0.14	1.45	29.33	8.50	6.80	1.19	1.17	8.74	0.00	0.74	1.50	0.17	1.70	0.34	0.22	0.04		
		max	59		0.646	1.50	0.14	1.45	35.75	11.33	10.90	1.38	1.50	34.55	0.01	2.20	1.60	0.52	2.03	0.73	0.38	0.07		

Table C.5 Individual Test Data for Dynamic Tests on Cortical Veins, both from Surgery and Autopsy, along with Dynamic Model Adjustments

Test	Date	Vessel	Age	Sex	Cs Area (mm^2)	~OD (mm)	Wall (mm)	InV/Ex Ratio	Tm:d-t (hr)	Tm:r-t (hr)	GageL (mm)	Pc Lam	Toe Lam	A	B	Max Mod	lamY	sigY (MPa)	Max Lam	Su (MPa)	Max Load (N)	Rate (s-1)	Fail Loc	Grips Type
Veins-Dynamic																								
Surgery Vessels																								
2-18-00v	2/18/00	temp cort	27	M	0.422	1.06	0.12	1.37	N/A	4	8.20	N/A	-	-	-	-	-	-	N/A	7.37	3.11	524	end	flat
3-31-00v2	3/31/00	temp cort	37	F	0.121	0.42	0.06	1.03	N/A	6.5	6.80	N/A	-	-	-	13.95	1.48	2.29	1.54	2.72	0.33	313	mid	flat
4-28-00v1	4/28/00	temp cort	25	F	0.269	0.71	0.12	1.10	N/A	3.75	4.90	N/A	1.68	3.82	0.415	8.38	2.03	3.98	2.23	4.98	1.34	432	mid	flat
4-28-00v2	4/28/00	temp cort	25	F	0.269	0.71	0.12	1.10	N/A	4	6.70	N/A	1.68	8.88	0.022	10.40	1.86	2.72	2.04	3.83	1.03	306	mid	flat
5-12-00v	5/12/00	temp cort	39	F	0.114	0.54	0.07	1.13	N/A	4	7.50	N/A	-	-	-	6.08	1.76	1.50	1.85	1.80	0.21	303	end	flat
5-19-00v1	5/19/00	temp cort	36	F	0.11*	0.35*		1.47	N/A	3.5	8.00	N/A	-	-	-	-	-	-	2.00	4.35*	0.48	215	mid	flat
5-26-00v	5/26/00	temp cort	34	F	N/A	0.61		1.14	N/A	4.5	9.00	1.23	-	-	-	-	-	-	1.59	-	0.25	196	mid	flat
		number	7		5	6	5	7	0	7	7	1	2	2	2	4	4	4	6	5	7	7		
		avg	31.9		0.239	0.68	0.10	1.19		4.32	7.30	1.23	1.68	6.35	0.22	9.70	1.78	2.62	1.88	4.14	0.96	327		
		stdev	6.01		0.127	0.22	0.03	0.16		1.01	1.33		0.00	3.58	0.28	3.34	0.23	1.04	0.27	2.16	1.04	116		
		min	25		0.114	0.42	0.06	1.03		3.50	4.90	1.23	1.68	3.82	0.02	6.08	1.48	1.50	1.54	1.80	0.21	196		
		max	39		0.422	1.06	0.12	1.47		6.50	9.00	1.23	1.68	8.88	0.42	13.95	2.03	3.98	2.23	7.37	3.11	524		
Dynamic Modeling																								
3-31-00v2													1.26	10.20	0.472	6.44			1.54	2.38		312		
4-28-00v1													1.61	3.27	0.917	6.64			2.08	4.91		402		
4-28-00v2													1.63	8.38	0.037	7.51			2.02	3.79		306		
5-12-00v													1.51	9.33	0.035	3.70			1.84	1.66		303		
		number											4	4	4	4			4	4		4		
		avg											1.50	7.80	0.37	6.07			1.87	3.19		331		
		stdev											0.17	3.11	0.42	1.65			0.24	1.45		48		
Autopsy Vessels																								
8-14-01-1v12	8/14/01	temp cort	59	M	0.646	1.5	0.14	N/A	35.75	8.5	11.10	1.19	1.25	12.36	0.089	2.22	1.35	0.36	1.39	0.45	0.29	57	mid	flat
8-23-01v2	8/23/01	temp cort	38	M	0.519	1.28	0.14	1.45	29.5	11.5	5.48	1.41	1.51	9.71	0.031	3.08	1.67	0.93	2.20	1.83	0.95	138	mid	flat
		number	2		2	2	2	1	2	2	2	2	2	2	2	2	2	2	2	2	2	2		
		avg	48.5		0.583	1.39	0.14	1.45	32.63	10.00	8.29	1.30	1.38	11.04	0.06	2.65	1.51	0.65	1.80	1.14	0.62	98		
		stdev	15		0.090	0.16	0.00		4.42	2.12	3.97	0.16	0.18	1.87	0.04	0.61	0.23	0.40	0.57	0.98	0.47	57		
		min	38		0.519	1.28	0.14	1.45	29.50	8.50	5.48	1.19	1.25	9.71	0.03	2.22	1.35	0.36	1.39	0.45	0.29	57		
		max	59		0.646	1.50	0.14	1.45	35.75	11.50	11.10	1.41	1.51	12.36	0.09	3.08	1.67	0.93	2.20	1.83	0.95	138		
Dynamic Modeling																								
8-14-01-1v12													nothing significant											
8-23-01v2													nothing significant											

D Residual Stresses

It has been noted that the thin wall assumption was applied to the vessels of this study. As the consideration of residual stresses in the vessel wall is inconsistent with this assumption, these stresses are not included in calculations of stress and stretch in this work. Nevertheless, as a matter of general interest, opening angles associated with cut sections from various arteries and veins, both from surgery and autopsy, are reported in Table D.1. Specimens from autopsy are identified with Aut in their name. As the table shows, some of the measurements included multiple sections from different points along the vessel length.

Table D.1 Number of Sections, Opening Angle (or Average Opening Angle), and Range of Measured Angles (for Multiple Sections) for Selected Arteries and Veins

	Number of Sections	Angle (or Avg.) (deg)	Angle Variation (deg)
Art 1	2	34	23, 46
Art 2	6	30	0-60
Art 3	1	139	
ArtAut1	1	46	
ArtAut2	1	38	
Vein1	2	67	64, 71
VeinAut1	1	114	

E Statistical Data

E.1 PRELIMINARY MANOVA TESTS – PREDICT ALL EIGHT DEPENDENT VARIABLES

Table E.1 Preliminary MANOVA Testing. Predictors: Three Main Independents and One Covariate

Predictor	PValue	Predictor	PValue
QS_Dynamic	<.0001	QS_Dynamic	0.0001
Art_Vein	<.0001	Art_Vein	<.0001
Surg_Aut	<.0001	Surg_Aut	<.0001
No covariate		Mfail	0.9575
QS_Dynamic	0.0001	QS_Dynamic	<.0001
Art_Vein	<.0001	Art_Vein	<.0001
Surg_Aut	0.0005	Surg_Aut	0.0003
Age	0.1143	LogArea	0.5269
QS_Dynamic	0.0002	QS_Dynamic	<.0001
Art_Vein	<.0001	Art_Vein	<.0001
Surg_Aut	<.0001	Surg_Aut	0.0012
Male	0.6807	LogOD	0.5755
QS_Dynamic	<.0001	QS_Dynamic	<.0001
Art_Vein	<.0001	Art_Vein	<.0001
Surg_Aut	0.2996	Surg_Aut	<.0001
Tm2	0.41	Wall	0.38
QS_Dynamic	<.0001	QS_Dynamic	0.0101
Art_Vein	<.0001	Art_Vein	0.0284
Surg_Aut	<.0001	Surg_Aut	0.01
GageL	0.1335	InV_Ex	0.4278

Table E.2 Preliminary MANOVA Testing. Predictors: Main Independents, Interactions Between Main Independents and One Covariate, and the Covariate

Predictor	PValue
QS_Dynamic	0.0185
Art_Vein	0.045
Surg_Aut	0.5171
QS_Dynamic_Age	0.0375
Art_Vein_Age	0.1299
Surg_Aut_Age	0.6865
Age	0.3619

Predictor	PValue
QS_Dynamic	0.0973
Art_Vein	0.0225
Surg_Aut	0.0218
QS_Dynamic_LogArea	0.7623
Art_Vein_LogArea	0.2637
Surg_Aut_LogArea	0.0903
LogArea	0.1803

QS_Dynamic	0.0009
Art_Vein	0.0143
QS_Dynamic_Male	0.0812
Art_Vein_Male	0.7353

QS_Dynamic	0.0003
Art_Vein	<.0001
Surg_Aut	0.0135
QS_Dynamic_LogOD	0.6779
Art_Vein_LogOD	0.4629
Surg_Aut_LogOD	0.2118
LogOD	0.2

*** not all terms estimable**

QS_Dynamic	0.0071
Art_Vein	0.031
Surg_Aut	0.3787
QS_Dynamic_Tm2	0.0675
Art_Vein_Tm2	0.3661
Surg_Aut_Tm2	0.3041
Tm2	0.7655

QS_Dynamic	0.0213
Art_Vein	0.1261
Surg_Aut	0.0239
QS_Dynamic_Wall	0.9192
Art_Vein_Wall	0.4188
Surg_Aut_Wall	0.087
Wall	0.3634

QS_Dynamic	0.0027
Art_Vein	0.0721
Surg_Aut	0.0971
QS_Dynamic_GageL	0.0583
Art_Vein_GageL	0.3527
Surg_Aut_GageL	0.6969
GageL	0.6247

QS_Dynamic	0.217
Art_Vein	0.0849
Surg_Aut	0.064
QS_Dynamic_InV_Ex	0.2777
Art_Vein_InV_Ex	0.1549
Surg_Aut_InV_Ex	0.0794
InV_Ex	0.0872

QS_Dynamic	0.011
Art_Vein	0.0022
Surg_Aut	0.0029
QS_Dynamic_Mfail	0.8398
Art_Vein_Mfail	0.7524
Surg_Aut_Mfail	0.754
Mfail	0.6065

Table E.3 Preliminary MANOVA Testing. Predictors: Main Independents and their Two-Way Interactions and One Covariate

Predictor	P-value	Predictor	P-value
QS_Dynamic	0.3552	QS_Dynamic	0.4587
Art_Vein	0.007	Art_Vein	0.0097
Surg_Aut	0.2174	Surg_Aut	0.218
QS_Dynamic x Art_Vein	0.4736	QS_Dynamic x Art_Vein	0.4711
QS_Dynamic x Surg_Aut	0.0957	QS_Dynamic x Surg_Aut	0.1061
Art_Vein x Surg_Aut	0.3541	Art_Vein x Surg_Aut	0.3885
		Mfail	0.9518
QS_Dynamic	0.3405	QS_Dynamic	0.3799
Art_Vein	0.0026	Art_Vein	0.0095
Surg_Aut	0.2563	Surg_Aut	0.2261
QS_Dynamic x Art_Vein	0.4336	QS_Dynamic x Art_Vein	0.5073
QS_Dynamic x Surg_Aut	0.116	QS_Dynamic x Surg_Aut	0.1092
Art_Vein x Surg_Aut	0.37	Art_Vein x Surg_Aut	0.3212
Age	0.1327	LogArea	0.5076
QS_Dynamic	0.394	QS_Dynamic	0.3819
Art_Vein	0.0097	Art_Vein	0.0108
Surg_Aut	0.2203	Surg_Aut	0.2182
QS_Dynamic x Art_Vein	0.3761	QS_Dynamic x Art_Vein	0.5038
QS_Dynamic x Surg_Aut	0.0347	QS_Dynamic x Surg_Aut	0.1044
Art_Vein x Surg_Aut	0.3715	Art_Vein x Surg_Aut	0.3721
Male	0.3485	LogOD	0.6128
QS_Dynamic	0.2857	QS_Dynamic	0.3683
Art_Vein	0.0055	Art_Vein	0.0026
Surg_Aut	0.4328	Surg_Aut	0.2431
QS_Dynamic x Art_Vein	0.5707	QS_Dynamic x Art_Vein	0.5043
QS_Dynamic x Surg_Aut	0.1024	QS_Dynamic x Surg_Aut	0.1111
Art_Vein x Surg_Aut	0.2511	Art_Vein x Surg_Aut	0.2582
Tm2	0.5621	Wall	0.3163
QS_Dynamic	0.3996	QS_Dynamic	0.1245
Art_Vein	0.0053	Art_Vein	0.5727
Surg_Aut	0.3015	Surg_Aut	0.1225
QS_Dynamic x Art_Vein	0.5393	QS_Dynamic x Art_Vein	0.2963
QS_Dynamic x Surg_Aut	0.0664	QS_Dynamic x Surg_Aut	0.8273
Art_Vein x Surg_Aut	0.3831	Art_Vein x Surg_Aut	0.1527
GageL	0.1323	InV_Ex	0.0776

E.2 FINAL STATISTICAL MODEL – PREDICTIONS

Table E.4 Predict Changes in all Eight Dependent Variables based on changes in Artery_Vein, Surg_Aut, Qs_Dynamic, Age_Dyn, Age_Qs

Change in Predictor	Dependent	Est. Change in Parameter	Standard Error	Lower 95% CI	Upper 95% CI	P-value
Artery instead of Vein	Toe_lam	-0.16083	0.03793	-0.2352	-0.0865	0.00021
	A	15.36024	3.49417	8.5117	22.2088	0.00014
	B	0.20438	0.09711	0.014	0.3947	0.04411
	ModY	18.65111	2.69625	13.3665	23.9358	0
	lamY	-0.26179	0.05252	-0.3647	-0.1589	0.00003
	sigY	2.49082	0.34196	1.8206	3.1611	0
	lamU	-0.47664	0.05628	-0.5869	-0.3663	0
	sigU	2.84873	0.4399	1.9865	3.7109	0
	Multivariate (combined effect of predictor on all eight parameters)					0
Surgery instead of Autopsy	Toe_lam	0.12251	0.05045	0.0236	0.2214	0.0216
	A	-13.3933	4.64797	-22.5033	-4.2832	0.00737
	B	0.33112	0.12918	0.0779	0.5843	0.01582
	ModY	9.03096	3.58657	2.0013	16.0606	0.01758
	lamY	0.14251	0.06986	0.0056	0.2794	0.05057
	sigY	2.27229	0.45487	1.3807	3.1638	0.00003
	lamU	0.07981	0.07486	-0.0669	0.2265	0.29517
	sigU	2.33121	0.58515	1.1843	3.4781	0.00042
	Multivariate (combined effect of predictor on all eight parameters)					0.00064
Dynamic instead of Quasi-static	Toe_lam	0.43607	0.12417	0.1927	0.6794	0.00148
	A	-5.81243	11.43936	-28.2336	16.6087	0.61522
	B	0.08279	0.31793	-0.5404	0.7059	0.79641
	ModY	-4.68015	8.8271	-21.9813	12.621	0.60001
	lamY	0.39847	0.17194	0.0615	0.7355	0.02774
	sigY	2.37107	1.11951	0.1768	4.5653	0.04287
	lamU	0.40048	0.18425	0.0393	0.7616	0.03805
	sigU	2.71081	1.44015	-0.1119	5.5335	0.06986
	Multivariate (combined effect of predictor on all eight parameters)					0.01238
Age Effect for Dynamic Tests (change is per year increase in age)	Toe_lam	-0.0069	0.00248	-0.0118	-0.002	0.00954
	A	0.16266	0.22893	-0.286	0.6114	0.48305
	B	0.0026	0.00636	-0.0099	0.0151	0.68584
	ModY	0.53887	0.17665	0.1926	0.8851	0.00485
	lamY	-0.0086	0.00344	-0.0153	-0.0019	0.01838
	sigY	0.01763	0.0224	-0.0263	0.0615	0.43774
	lamU	-0.01104	0.00369	-0.0183	-0.0038	0.00557
	sigU	0.01407	0.02882	-0.0424	0.0706	0.62916
	Multivariate (combined effect of predictor on all eight parameters)					0.0228
Age Effect for Quasi-static Tests (change is per year increase in age)	Toe_lam	0.000254	0.00198	-0.0036	0.0041	0.8987
	A	0.24298	0.18237	-0.1145	0.6004	0.19311
	B	0.00123	0.00507	-0.0087	0.0112	0.81013
	ModY	0.16954	0.14072	-0.1063	0.4454	0.23803
	lamY	-0.00092	0.00274	-0.0063	0.0045	0.73939
	sigY	0.0371	0.01785	0.0021	0.0721	0.04657
	lamU	-0.00326	0.00294	-0.009	0.0025	0.2766
	sigU	0.02335	0.02296	-0.0216	0.0684	0.31754
	Multivariate (combined effect of predictor on all eight parameters)					0.21468
Overall Age	Multivariate (combined effect of predictor on all eight parameters)					0.02942

E.3 PREDICTED CURVE PARAMETER VALUES

Table E.5 Predicted Curve Parameter Values for Specific Variations and Combinations of the Independent Variables

Art / Vein	Surg / Aut	QS / Dyn	Age	Param	Pred
Artery	**Surgery**	**QS**	**30**	A	22.41
				B	0.36
				ModY	21.74
				Toe_lam	1.26
				lamU	1.49
				lamY	1.44
				sigU	4.42
				sigY	3.68
Artery	**Surgery**	**QS**	**40**	A	24.84
				B	0.38
				ModY	23.44
				Toe_lam	1.26
				lamU	1.46
				lamY	1.43
				sigU	4.66
				sigY	4.05
Artery	**Surgery**	**QS**	**50**	A	27.27
				B	0.39
				ModY	25.13
				Toe_lam	1.27
				lamU	1.42
				lamY	1.42
				sigU	4.89
				sigY	4.42
Artery	**Surgery**	**QS**	**60**	A	29.70
				B	0.40
				ModY	26.83
				Toe_lam	1.27
				lamU	1.39
				lamY	1.41
				sigU	5.12
				sigY	4.79
Artery	**Surgery**	**Dyn**	**30**	A	14.19
				B	0.49
				ModY	28.14
				Toe_lam	1.48
				lamU	1.66
				lamY	1.61
				sigU	6.86
				sigY	5.46
Artery	**Surgery**	**Dyn**	**40**	A	15.81
				B	0.51
				ModY	33.53
				Toe_lam	1.41
				lamU	1.54
				lamY	1.52
				sigU	7.00
				sigY	5.64
Artery	**Surgery**	**Dyn**	**50**	A	17.44
				B	0.54
				ModY	38.92
				Toe_lam	1.34
				lamU	1.43
				lamY	1.44
				sigU	7.14
				sigY	5.82
Artery	**Surgery**	**Dyn**	**60**	A	19.07
				B	0.57
				ModY	44.31
				Toe_lam	1.28
				lamU	1.32
				lamY	1.35
				sigU	7.28
				sigY	5.99
Artery	**Autops**	**QS**	**30**	A	35.80
				B	0.03
				ModY	12.71
				Toe_lam	1.14
				lamU	1.41
				lamY	1.30
				sigU	2.09
				sigY	1.40
Artery	**Autops**	**QS**	**40**	A	38.23
				B	0.05
				ModY	14.41
				Toe_lam	1.14
				lamU	1.38
				lamY	1.29
				sigU	2.33
				sigY	1.78

Art / Vein	Surg / Aut	QS / Dyn	Age	Param	Pred
Artery	**Autops**	**QS**	**50**	A	40.66
				B	0.06
				ModY	16.10
				Toe_lam	1.14
				lamU	1.34
				lamY	1.28
				sigU	2.56
				sigY	2.15
Artery	**Autops**	**QS**	**60**	A	43.09
				B	0.07
				ModY	17.80
				Toe_lam	1.15
				lamU	1.31
				lamY	1.27
				sigU	2.79
				sigY	2.52
Artery	**Autops**	**Dyn**	**30**	A	27.58
				B	0.16
				ModY	19.11
				Toe_lam	1.36
				lamU	1.58
				lamY	1.47
				sigU	4.52
				sigY	3.19
Artery	**Autops**	**Dyn**	**40**	A	29.21
				B	0.18
				ModY	24.50
				Toe_lam	1.29
				lamU	1.47
				lamY	1.38
				sigU	4.67
				sigY	3.37
Artery	**Autops**	**Dyn**	**50**	A	30.83
				B	0.21
				ModY	29.89
				Toe_lam	1.22
				lamU	1.35
				lamY	1.30
				sigU	4.81
				sigY	3.54
Artery	**Autops**	**Dyn**	**60**	A	32.46
				B	0.24
				ModY	35.28
				Toe_lam	1.15
				lamU	1.24
				lamY	1.21
				sigU	4.95
				sigY	3.72
Vein	**Surgery**	**QS**	**30**	A	7.05
				B	0.16
				ModY	3.09
				Toe_lam	1.42
				lamU	1.97
				lamY	1.70
				sigU	1.57
				sigY	1.19
Vein	**Surgery**	**QS**	**40**	A	9.48
				B	0.17
				ModY	4.79
				Toe_lam	1.42
				lamU	1.93
				lamY	1.70
				sigU	1.81
				sigY	1.56
Vein	**Surgery**	**QS**	**50**	A	11.91
				B	0.18
				ModY	6.48
				Toe_lam	1.43
				lamU	1.90
				lamY	1.69
				sigU	2.04
				sigY	1.93
Vein	**Surgery**	**QS**	**60**	A	14.34
				B	0.20
				ModY	8.18
				Toe_lam	1.43
				lamU	1.87
				lamY	1.68
				sigU	2.28
				sigY	2.30

Art / Vein	Surg / Aut	QS / Dyn	Age	Param	Pred
Vein	**Surgery**	**Dyn**	**30**	A	-1.17
				B	0.28
				ModY	9.49
				Toe_lam	1.64
				lamU	2.13
				lamY	1.87
				sigU	4.01
				sigY	2.97
Vein	**Surgery**	**Dyn**	**40**	A	0.45
				B	0.31
				ModY	14.88
				Toe_lam	1.57
				lamU	2.02
				lamY	1.79
				sigU	4.15
				sigY	3.15
Vein	**Surgery**	**Dyn**	**50**	A	2.08
				B	0.34
				ModY	20.27
				Toe_lam	1.51
				lamU	1.91
				lamY	1.70
				sigU	4.29
				sigY	3.33
Vein	**Surgery**	**Dyn**	**60**	A	3.71
				B	0.36
				ModY	25.66
				Toe_lam	1.44
				lamU	1.80
				lamY	1.61
				sigU	4.43
				sigY	3.50
Vein	**Autops**	**QS**	**30**	A	20.44
				B	-0.17
				ModY	-5.94
				Toe_lam	1.30
				lamU	1.89
				lamY	1.56
				sigU	-0.76
				sigY	-1.09
Vein	**Autops**	**QS**	**40**	A	22.87
				B	-0.16
				ModY	-4.24
				Toe_lam	1.30
				lamU	1.85
				lamY	1.55
				sigU	-0.52
				sigY	-0.72
Vein	**Autops**	**QS**	**50**	A	25.30
				B	-0.15
				ModY	-2.55
				Toe_lam	1.30
				lamU	1.82
				lamY	1.54
				sigU	-0.29
				sigY	-0.34
Vein	**Autops**	**QS**	**60**	A	27.73
				B	-0.13
				ModY	-0.85
				Toe_lam	1.31
				lamU	1.79
				lamY	1.53
				sigU	-0.06
				sigY	0.03
Vein	**Autops**	**Dyn**	**30**	A	12.22
				B	-0.05
				ModY	0.46
				Toe_lam	1.52
				lamU	2.05
				lamY	1.73
				sigU	1.68
				sigY	0.70
Vein	**Autops**	**Dyn**	**40**	A	13.85
				B	-0.02
				ModY	5.85
				Toe_lam	1.45
				lamU	1.94
				lamY	1.64
				sigU	1.82
				sigY	0.88

Art / Vein	Surg / Aut	QS / Dyn	Age	Param	Pred
Vein	**Autops**	**Dyn**	**50**	A	15.47
				B	0.00
				ModY	11.24
				Toe_lam	1.38
				lamU	1.83
				lamY	1.56
				sigU	1.96
				sigY	1.05

Art / Vein	Surg / Aut	QS / Dyn	Age	Param	Pred
Vein	**Autops**	**Dyn**	**60**	A	17.10
				B	0.03
				ModY	16.63
				Toe_lam	1.31
				lamU	1.72
				lamY	1.47
				sigU	2.10
				sigY	1.23

E.4 INTERACTIONS BETWEEN SURGERY-AUTOPSY AND QUASI-STATIC (QS)-DYNAMIC

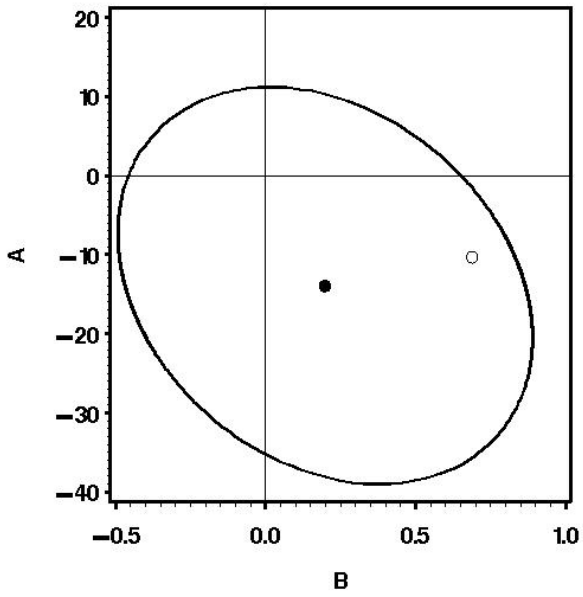

Figure E.1 Joint confidence interval of changes in *A* and *B* for surgery specimens compared to those from autopsy. Quasi-static and dynamic tests are represented by the solid and open dots, respectively. An ellipse could not be generated for the dynamic case due to a lack of data.

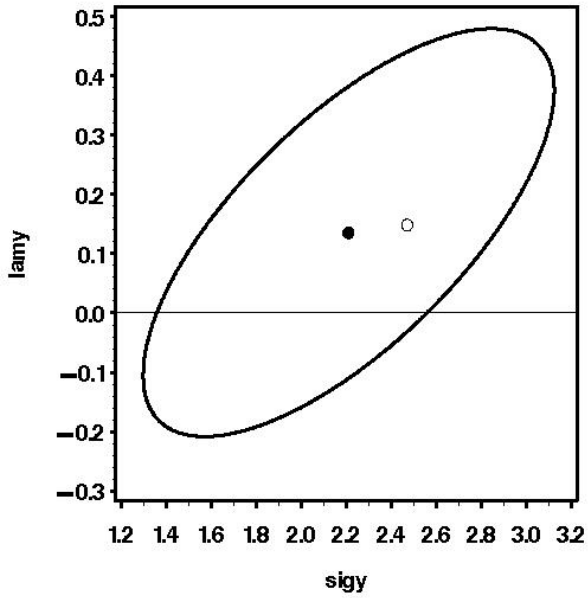

Figure E.2 Joint confidence interval of changes in λ_Y (lamy) and σ_Y (sigy) for surgery specimens compared to those from autopsy. Quasi-static and dynamic tests are represented by the solid and open dots, respectively. An ellipse could not be generated for the dynamic case due to a lack of data.

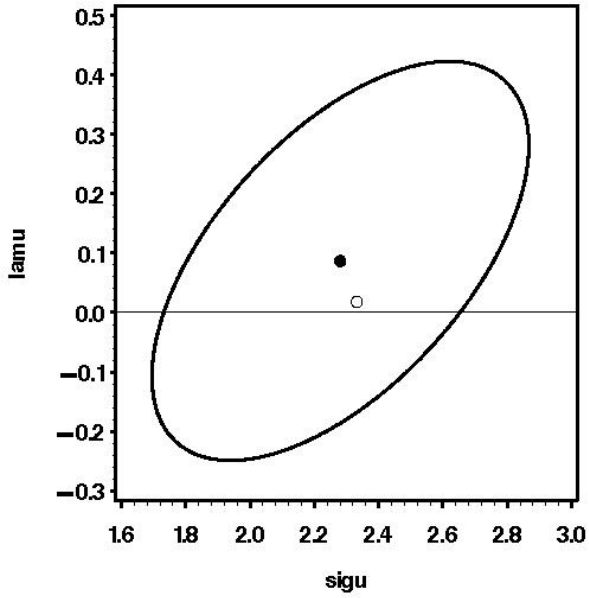

Figure E.3 Joint confidence interval of changes in λ_U (lamu) and σ_U (sigu) for surgery specimens compared to those from autopsy. Quasi-static and dynamic tests are represented by the solid and open dots, respectively. An ellipse could not be generated for the dynamic case due to a lack of data.

E.5 ADJUSTED STATISTICAL MODEL (BASED ON DYNAMIC MODELING RESULTS)

Table E.6 Predict Six Dependent Variables from Artery_Vein, Surg_Aut, Qs_Dynamic, Age_Dyn, Age_Qs, based on Data Adjusted from Dynamic Modeling

Change in Predictor	Dependent	Est. Change in Parameter	Standard Error	Lower 95% CI	Upper 95% CI	P-value
Artery instead of Vein	Toe_lam	-0.16024	0.03651	-0.2318	-0.0887	0.0001
	A	13.91925	3.0508	7.9397	19.8988	0.00006
	B	0.21562	0.12417	-0.0278	0.459	0.09127
	ModY	15.34581	2.69696	10.0598	20.6319	0
	lamU	-0.41428	0.05687	-0.5258	-0.3028	0
	sigU	2.6634	0.49489	1.6934	3.6334	0.00001
	Multivariate (combined effect of predictor on all eight parameters)					0
Surgery instead of Autopsy	Toe_lam	0.07095	0.0471	-0.0214	0.1633	0.14093
	A	-13.3793	3.93529	-21.0925	-5.6661	0.0017
	B	0.47315	0.16017	0.1592	0.7871	0.00557
	ModY	1.74618	3.47887	-5.0724	8.5648	0.61885
	lamU	0.05547	0.07336	-0.0883	0.1993	0.45462
	sigU	1.25104	0.63836	-0.0002	2.5022	0.05802
	Multivariate (combined effect of predictor on all eight parameters)					0.00205
Dynamic instead of Quasi-static	Toe_lam	0.27337	0.11911	0.0399	0.5068	0.02784
	A	-3.05573	9.95238	-22.5624	16.4509	0.76064
	B	0.10621	0.40506	-0.6877	0.9001	0.79471
	ModY	-15.0198	8.79809	-32.2641	2.2245	0.09665
	lamU	0.3147	0.18554	-0.0489	0.6784	0.09873
	sigU	0.59429	1.61443	-2.57	3.7586	0.71501
	Multivariate (combined effect of predictor on all eight parameters)					0.0054
Age Effect for Dynamic Tests (change is per year increase in age)	Toe_lam	-0.00592	0.00243	-0.0107	-0.0012	0.0202
	A	0.11507	0.20329	-0.2834	0.5135	0.57498
	B	0.00719	0.00827	-0.009	0.0234	0.3909
	ModY	0.44078	0.17971	0.0885	0.793	0.01931
	lamU	-0.01077	0.00379	-0.0182	-0.0033	0.00742
	sigU	0.02231	0.03298	-0.0423	0.0869	0.50314
	Multivariate (combined effect of predictor on all eight parameters)					0.01035
Age Effect for Quasi-static Tests (change is per year increase in age)	Toe_lam	-0.00097	0.00198	-0.0049	0.0029	0.62667
	A	0.24744	0.16545	-0.0768	0.5717	0.14373
	B	0.00457	0.00673	-0.0086	0.0178	0.50191
	ModY	0.00604	0.14626	-0.2806	0.2927	0.96731
	lamU	-0.00401	0.00308	-0.0101	0.002	0.20166
	sigU	-0.00177	0.02684	-0.0544	0.0508	0.94791
	Multivariate (combined effect of predictor on all eight parameters)					0.60739
Overall Age	Multivariate (combined effect of predictor on all eight parameters)					0.0227

E.6 MANOVA TESTING FOR SIGNIFICANCE OF EXTENT OF PRECONDITIONING (PCLAM)

Table E.7 MANOVA Testing. Predictors: Three Main Independents and PcLam

Predictor	P-value
QS_Dynamic	0.0001
Art_Vein	<.0001
Surg_Aut	<.0001
pclam	0.2201

Table E.8 MANOVA Testing. Predictors: Main Independents, Interactions Between Main Independents and PcLam, and PcLam

Predictor	P-value
QS_Dynamic	0.4099
Art_Vein	0.0281
Surg_Aut	0.1915
QS_Dynamic x Art_Vein	0.4208
QS_Dynamic x Surg_Vein	0.1007
Art_Vein x Surg_Vein	0.4136
Pclam	0.2871

Table E.9 MANOVA Testing. Predictors: Main Independents and their Two-Way Interactions and PcLam

Predictor	P-value
QS_Dynamic	0.9081
Art_Vein	0.038
Surg_Aut	0.4586
QS_Dynamic_pclam	0.9324
Art_Vein_pclam	0.0679
Surg_Aut_pclam	0.6402
pclam	0.3732

Table E.10 Multivariate Comparisons of PcLam for Quasi-static and Dynamic Tests

Artery or vein	Dependent	Predicted Value for Dyn	Predicted Value for QS	Dyn - QS	Lower 95% CL for difference	Upper 95% CL for difference	Multivariate test	P-Value for MANOVA
Vein	A	8.7433	12.2531	-3.50971	-12.4945	5.475095	Method	0.3322
	B	0.1431	0.0742	0.068878	-0.10163	0.239381	pclam	0.8259
	Toe_lam	1.5288	1.3829	0.145918	-0.04835	0.340188		
	ModY	7.3075	2.9096	4.397949	1.3073	7.488598	Method	0.0807
	lamY	1.6905	1.6306	0.059893	-0.18175	0.301538	pclam	0.777
	sigY	1.9543	0.7887	1.165615	0.213991	2.11724		
	lamU	1.69	1.6482	0.041806	-0.20826	0.291868	Method	0.0473
	sigU	2.6199	1.1328	1.487094	0.304308	2.66988	pclam	0.717
Artery	A	25.7192	33.7842	-8.06506	-22.9274	6.797249	Method	0.5595
	B	0.31	0.2338	0.076112	-0.2528	0.405024	pclam	0.0452
	Toe_lam	1.2616	1.1877	0.073956	-0.03157	0.179484		
	ModY	29.2203	18.559	10.66134	2.213257	19.10943	Method	0.0063
	lamY	1.4216	1.3586	0.062961	-0.02862	0.154541	pclam	0.0002
	sigY	4.3054	3.0275	1.277828	0.121559	2.434097		
	lamU	1.4216	1.3586	0.062961	-0.02862	0.154541	Method	0.0096
	sigU	5.6997	3.5124	2.187384	0.774957	3.599811	pclam	0.0002

Table E.11 Multivariate Comparisons of PcLam for Surgery and Autopsy

Artery or vein	Dependent	Autopsy	Surgery	Aut - Surg	Lower 95% CL for difference	Upper 95% CL for difference	Multivariate test	P-Value for MANOVA
Vein	A	16.4046	9.0897	7.314862	-0.09948	14.7292	Surg_Aut	0.241
	B	0.0256	0.1213	-0.09571	-0.24908	0.057659	pclam	0.8417
	Toe_lam	1.349	1.4514	-0.10237	-0.29152	0.086785		
	ModY	1.7592	5.3818	-3.62258	-7.28491	0.039743	Surg_Aut	0.1725
	lamY	1.5269	1.6981	-0.17128	-0.41258	0.070013	pclam	0.5669
	sigY	0.4015	1.4756	-1.07414	-2.14026	-0.00802		
	lamU	1.8342	1.9366	-0.1024	-0.38656	0.181755	Surg_Aut	0.1889
	sigU	0.7717	2.0268	-1.25503	-2.60113	0.091067	pclam	0.8893
Artery	A	39.8546	22.5033	17.35132	5.982033	28.7206	Surg_Aut	0.0037
	B	0.0711	0.4545	-0.38343	-0.62693	-0.13994	pclam	0.0443
	Toe_lam	1.1591	1.2618	-0.10265	-0.19079	-0.01451		
	ModY	23.6398	23.3194	0.320372	-10.5591	11.19982	Surg_Aut	0.005
	lamY	1.3183	1.4571	-0.13883	-0.22877	-0.04889	pclam	0.0081
	sigY	2.8857	4.3489	-1.46324	-2.76749	-0.15899		
	lamU	1.3659	1.5215	-0.1556	-0.2649	-0.04631	Surg_Aut	0.0162
	sigU	3.7288	5.1857	-1.45691	-3.18387	0.270054	pclam	0.0126